ABSTRACT

Title of Document: LIMITS OF THIN FILM COOLING IN MICROGAP CHANNELS

Emil Rahim, Doctor of Philosophy, 2011.

Directed by: Professor Avram Bar-Cohen
Department of Mechanical Engineering

The forced flow of dielectric liquids, undergoing phase change while flowing in a narrow channel, is a promising candidate for the thermal management of advanced semiconductor devices. Such channels may be created by the spacing between silicon ribs in a microchannel cooler, between stacked silicon chips in a three-dimensional logic, RF, or heterogeneous microsystem, narrowly-spaced organic or ceramic substrates, or between a chip and a non-silicon polymer cover in a microgap cooler.

These microgap configurations provide direct contact – and hence cooling – between a chemically-inert, dielectric liquid and the back surface of an active electronic component, thus eliminating the significant thermal resistance associated with a Thermal Interface Material (TIM) or the solid-solid contact resulting from the attachment of a microchannel cold plate to the chip.

This dissertation explores the physics underpinning two-phase flow in miniature channels, through an extensive literature survey, and employs analytical, numerical, and experimental techniques to determine the thermal transport phenomena in microgap channels, with emphasis on the thermal limits of thin film heat transfer in annular flow.

The applicability of several flow regime mapping methodologies has been examined. The predictions of these mapping methodologies have been compared to the visual observations of two-phase flow in microtubes and microchannels. The axial variation of two-phase heat transfer coefficients with local vapor qualities is reported, and the association of this variation with the dominant flow regime is discussed. The measured two-phase flow heat transfer coefficients are then sorted according to the dominant flow regime, and compared to the predictions of classical heat transfer correlations.

Two-phase flow experiments were performed in a microgap cooler with the flow of HFE7100 and FC-87. The microgap cooler is 125 mm long, 14 mm wide, and was operated with three distinct gap sizes: 100, 200, and 500 micron. An instrumented Intel thermal test vehicle (TTV) flip-chip mounted via a BGA on an organic substrate, and equipped with 9 pre-calibrated temperature sensors, was used as the heated section of the microgap channel. Pressure drop across the channel, fluid inlet and exit temperature, and wall temperature were measured.

Using commercial software, an “inverse” numerical technique was developed to identify the local heat flux and heat transfer coefficient. Local Annular heat transfer coefficients, for FC-87

flowing in the 100 micron channel, were found to display elements of the M-shaped variation with flow quality and reached a maximum value of 15 kW/m^2K.

LIMITS OF THIN FILM COOLING IN MICROGAP CHANNELS

By

Emil Rahim

Dissertation Submitted to the Faculty of the Graduate School of the
University of Maryland, College Park, in partial fulfillment
of the requirements for the degree
of Doctor of Philosophy
2011

Advisory Committee:
Professor Avram Bar-Cohen, Chair
Professor Marino di Marzo
Associate Professor Patrick McCluskey
Associate Professor Bao Yang
Professor Gary Pertmer

Dedication

To my parents, Amal and Nabil, and my sister Carine

Thank you for your love and support

Acknowledgements

I am most grateful to my advisor, Professor Avram Bar-Cohen for his ongoing support and encouragement. I am very thankful to have had the greatest opportunity to do my PhD under his direction. Thank you, ABC, for the most helpful advice, and for being there with your unlimited knowledge, encouragement, and positive energy to help at all times.

I would like to thank my dissertation defense committee members; Professor Marino di Marzo, Professor Patrick McCluskey, Professor Gary Pertmer, and Professor Bao Yang for their helpful advices and their encouragement throughout the final stages of this work.

Many thanks to my friends and colleagues who helped me throughout my graduate school career; Dr. Andre Ali, Dr. Ilai Sher, Mr. Jan Muehlbauer, and last but not least my former and current labmates: Dr. Dae-Whan Kim, Dr. Peng Wang, Juan Cevallos, Mike Manno, Horacio Nochetto (special thanks for the help with the numerical modeling), Frank Robinson, Darin Sharar, and Jessica Sheehan.

I am very grateful for my family this side of the Atlantic, who helped make Maryland a welcoming home for me over the last few years; Thank you Sarkis, Jack, Joseph, Linda, Hala, Leila, Paul, and Nadia. I am very fortunate to have you in my life.

Special thanks to the Office of Naval Research for supporting this work. I would also like to thank Intel for providing the Thermal Test Vehicle, and Mr. Phil Tuma and 3M for providing the HFE-7100 and FC-87 coolants.

Table of Contents

List of Tables

List of Figures

Chapter 1

Introduction

The trend in electronics compactness, functionality, and feature count – and thus power dissipation is going in an upward direction. The International Electronics Manufacturing Initiative (iNEMI) projects the chip power and chip heat flux trends for various form factors such as servers and notebook platforms. Figure 1.1 shows the iNEMI's view of chip power chip flux trends for server platforms iNEMI (2005).

As can be seen in Figure 1.1, the chip power and heat flux could reach 350 W and 200 W/cm^2 in heat dissipation and heat flux, respectively, by 2018.

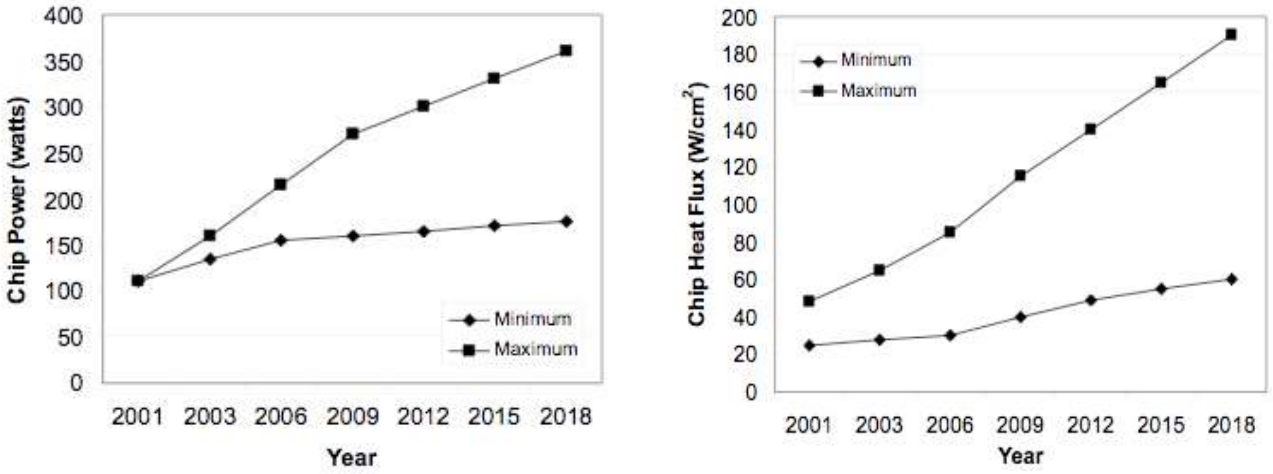

Figure 1.1 iNEMI's server chip power and chip heat flux trend

The objective of cooling flip chip dies with higher power dissipation, but continuously improving heat sinks, had shifted into the need for significantly lowering the maximum chip-to-

heat sink thermal resistance as this resistance became dominant and most critical resistance of the overall total system thermal resistance, Patel (2005).

The high chip-to-heat sink, and therefore junction-to-ambient, thermal resistance resulting from an air-cooled heat sink provides inadequate heat removal capability at the necessary junction temperatures for ITRS projections.

Attaching a massive heat sink to an electronic chip through multiple thermal interface materials (TIM) not only results in a large thermal resistance between the chip and the ambient, but also limits the packing density on the substrate, and increases chip-to-chip wiring length. The ITRS projected power density and junction-to-ambient thermal resistance for high performance chips at the 14 nm generation are over 100 W/cm^2, and less than 0.2 $^oC/W$, respectively. (ITRS 2009 SiP)

In order to keep the junction temperature constant as power dissipation increases, the size of the heat sink will be increasing significantly. This prevents the reduction of the system size, as well as the close placement of high performance chips in the lateral and vertical axes (3D packaging).

It would be good to flip the resistance chain, so that Tchip is on top next to the chip-to-sink resistance line. As a consequence, the thermal packaging community started searching for and investigating new cooling technologies for high heat flux chips. This is clearly shown in Figure 1.2, as beyond the year 2012, new cooling technologies ought to be implemented to achieve a lower

overall chip thermal resistance and in turn lower silicon junction temperature specification, Tosaya (2006).

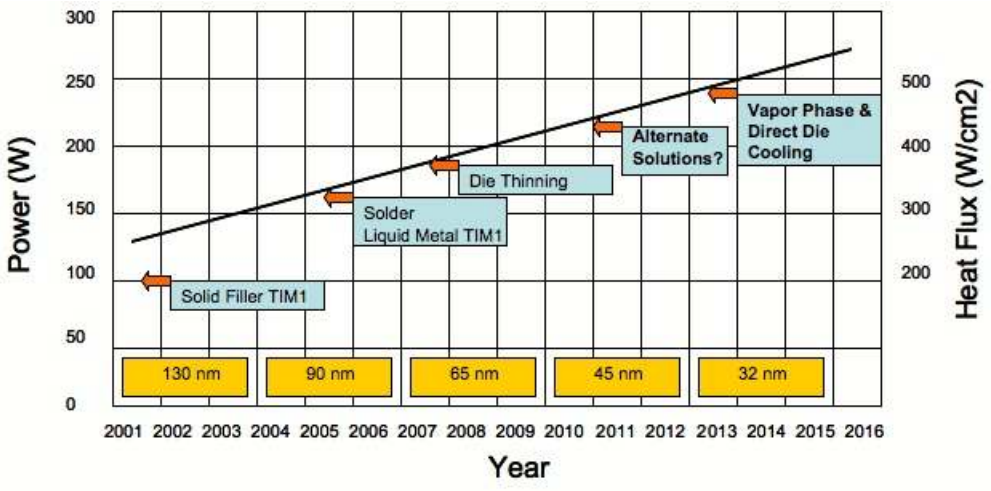

Figure 1.2 Cooling technology need as a function of chip power and heat flux, Tosaya (2006)

Advanced liquid cooling has started to emerge as a feasible solution for even cost performance electronics systems. The recent increase in CPU heat fluxes coupled with the need to thermally design for the highest possible heat flux, for speed reasons, caused thermal systems to become more complex and paved the way for active cooling.

Figure 1.3 displays implementations of two-phase cold plates for industrial power electronics systems, such as Integrated Gate Bipolar Systems (IGBT's), Howes (2008). The physical volume reduction achieved with the two-phase-cooled system concept is significant, as is the modest cost reduction versus the air-cooled system. The use of a vaporizable dielectric fluid, operating at its saturation temperature, allows the use of a smaller quantity of liquid, a smaller pump for low-flow operation, and smaller tubing diameters, when compared to a similar single-

phase water cooling system designed for use within the same type of cabinet and to dissipate the same module heat loads.

Figure 1.3 Integrated liquid cooled plate for IGBT module, Howes (2008)

Sharar et al (2011) compared the dissipated heat and heat transfer coefficients of single-phase and two-phase flow of water. Their study assumed two different values of temperature rise (delta) of 20 ^{o}C and 75 ^{o}C for the single-phase cooling, and an exit vapor quality of 0.5 while assuming saturation condition at the inlet of the cooler for the two-phase flow case.

As can be seen in Figure 1.4 from Sharar et al (2011), two-phase flow of water has the potential to transport heat dissipation over an order of magnitude greater than that of a single-phase flow of water.

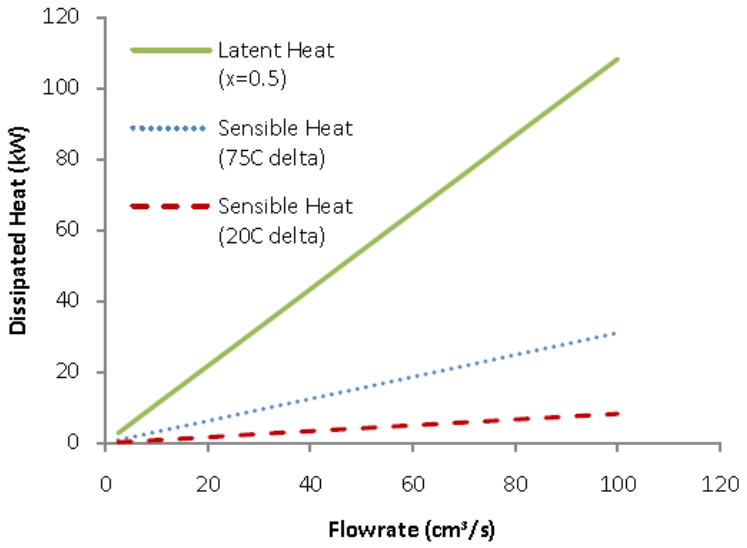

Figure 1.4 Dissipated heat vs flow rate for water using sensible heat (single-phase flow) and latent heat of vaporization (two-phase flow), Sharar et al (2011)

Wang et al (2011) performed first-order analytical model and system-level thermal simulation to compare single-phase and two-phase cold plate cooling performance for a package of 12 IGBT's and diodes. They concluded that for the same cold plate geometry, R134a two-phase cooling can substantially reduce the maximum IGBT temperature, allow all IGBT's to perform at a highly uniform temperature, and lower the pumping power by operating at lower flow rates than those required for single-phase cooling.

While direct contact cooling is thermally very efficient, in such configurations, it is the poorly understood two-phase flow phenomena that establish the upper bound on the heat removal capability. Thus, prediction of the thermal characteristics and limits, as well as the development of strategies for performance enhancement, of microgap coolers, requires an in-depth understanding of the underlying thermo-physics of two-phase flow in narrow channels.

This Dissertation begins with an analysis of two-phase flow regime data for small diameter tubes and channels and its comparison to the Taitel and Dukler flow regime predictions. The Taitel-Dukler predictions are found to agree qualitatively with the authors' observations; Annular flow dominates, Slug-Intermittent is seen at lower vapor quality.

Two-phase heat transfer data, gathered from the literature, and sorted by flow regime is compared to the predictions of 5 classical correlations; Chen, Shah, Gungor-Winterton, the revised Gungor-Winterton, and Kandlikar. It was found that specific correlations can provide improved accuracy in designated flow regimes and that the Chen correlation, in particular, can predict the low-to-moderate quality annular flow data in microgap channels with the same accuracy as usually associated with macrochannels, i.e. approximately +/- 25%. Examining the variation of the heat transfer data with quality has revealed the existence of a characteristic M-shaped heat transfer coefficient curve with two peaks, one associated with boiling incipience at near-zero but positive qualities and the other at moderate-to-high qualities, reflecting the deterioration of the heat transfer coefficient well before channel dryout.

Understanding the limitation imposed on thin film cooling by this premature deterioration in the heat transfer coefficient is at the heart of this Dissertation. Effort is devoted to defining, analyzing, and studying the possible mechanisms of the heat transfer coefficient deterioration and to modifying the Taitel-Dukler flow regime map to include a deteriorated heat transfer region within the parametric space of Annular flow. Along with other possible mechanisms, attention will be devoted to the Kelvin-Helmholtz instability, recent empirical results for wave structures on

liquid films and rivulet flow, and experimental data embedded in the venerable Chen correlation. In addition, original experimental data for two-phase heat transfer was obtained from a chip-scaled microgap cooler, across a range of operating conditions, and an effort was made to develop and demonstrate surface modifications that can postpone the deterioration in the heat transfer coefficient to higher flow quality.

Chapter 2

Two-Phase Flow Regimes in Microgap Coolers

The flow of vapor and liquid in a channel can take various forms depending on the distribution and extent of "aggregation" of the two phases, with each distinct vapor/liquid distribution referred to as a "flow regime." Four primary two-phase flow regimes: Bubble, Intermittent, Annular, and Stratified, as well as numerous sub-regimes, have been identified in the literature, Hetsroni (1982). Bubbly flow is associated with a uniform distribution of small spherical bubbles within the liquid phase. Intermittent flow is characterized by the flow of liquid "plugs" separated by elongated gas bubbles – often in the shape of "slugs" or bullets – though sometimes more chaotically mixed. In Annular flow, a relatively thin liquid layer flows along the channel walls, while the vapor flows in the center of the channel, creating a vapor "core" which may also contain entrained droplets. In vertical channels with heat addition, where the vapor content increases in the flow direction, the Bubbly regime is followed sequentially by the Intermittent and Annular regimes.

As part of an ongoing study at the Laboratory for Heat and Mass Transfer at the EPFL, the two-phase flow characteristics of R134a and R245fa, flowing through 509 micron and 790 micron diameter glass channels, at pressures ranging from 665 kPa to 887 kPa for R134a and at 213 kPa for R245fa, were observed. In these experiments, the two-phase mixtures were generated in similarly-sized electrically-heated, stainless steel channels. The length of the micro-evaporator varied from 30 to 70 mm and the mass flux ranged from 200 to 2000 kg/m^2s, along with inlet sub-cooling of 2 ^oC to 7 ^oC.

Visual observations of two-phase regimes are documented and compared to the predictions of the analytical flow regime models available in the literature; Taitel-Dukler, and later Ullmann-Brauner.

To avoid the confusion that might arise from the variety of names used by different authors for the same flow regime, as well as the subtle differences associated with specific sub-regimes, a common flow regime terminology – defined in Table 2.1 – is used to compare the observed and predicted two-phase flow regimes. It is to be noted that when the Revellin et al (2005) sub-regimes are combined into the primary two-phase flow regimes, 182 of the 2239 data points fall in the Bubble regime, 895 in the Slug, and 1162 in the Annular flow regime.

Revellin et al (2005) observed that the transition from Slug flow to the Annular regime occurred when the rear of the elongated bubbles (i.e. slugs) began to deform and adjacent slugs began to coalesce, progressing to a continuous central vapor core and a liquid film at the tube wall. The Bubble-to-Slug transition was associated with the coalescence of the dispersed bubbles to form elongated bubbles which have approximately the same diameter as the tube.

Table 2.1 Flow regime definition

Present Study	Taitel – Dukler (1976)	Ullmann – Brauner (2007)	Revellin et al (2005)
Bubble	Bubble	Dispersed Bubbly, Bubbly	Bubbly, Bubbly/Slug
Slug	Slug-Intermittent	Slug, Aerated Slug	Slug, Slug/Semi-Annular
Annular	Annular	Annular	Semi-Annular, Annular

2.1 Taitel-Dukler Flow Regime Maps

An appreciation for the dependence of thermofluid parameters on the form, as well as extent, of aggregation of each phase, led early researchers to describe and map the vapor-liquid flow regimes prevailing in channels used to generate and/or transport two-phase mixtures. Earliest among these was the empirical flow regime map developed by Baker (1954) and numerous other attempts to develop a generalized flow regime map followed; notably Mandhane et al. (1974), Taitel and Dukler (1976), and Weisman et al. (1979).

Most noteworthy among these was the pioneering effort by Taitel and Dukler, defining and mapping the four predominant flow regimes (Stratified, Intermittent, Bubble, and Annular) with superficial gas and superficial liquid coordinates and proposing physically-based criteria for the

transition from one regime to the next. After considerable additional contributions by Taitel and Dukler (1987), Barnea (1987), and Shoham (1982), in 1990 this effort culminated in the Unified Model for predicting flow regime transitions in channels of any orientation, based on simple physical criteria and using familiar two-phase non-dimensional groupings.

Figure 2.1 displays such a map, using the Froude number, the Martinelli number and the T parameter, relating the liquid pressure drop to buoyancy, as in Equation 2.2 below with the superimposed locus traced out by the data of Yang and Fujita (2004) for R113 flowing in a 0.2 mm channel.

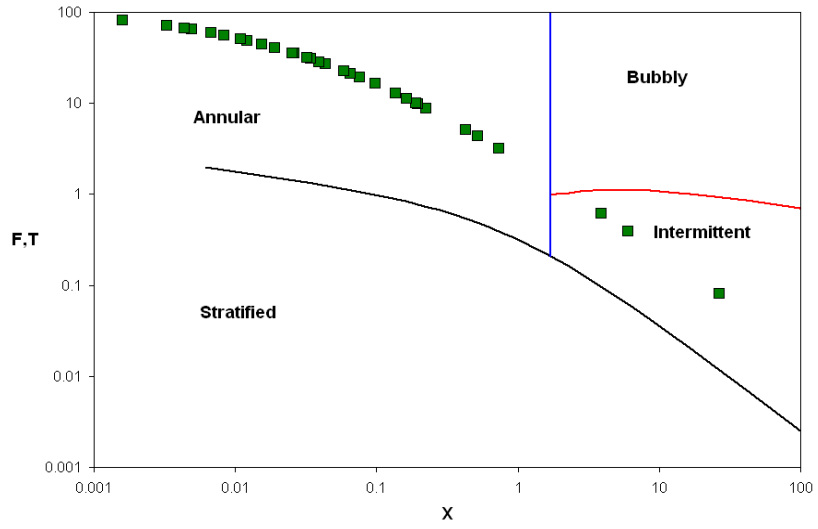

Figure 2.1 Taitel-Dukler non-dimensional two-phase flow regime map for horizontal tube. Data of Yang and Fujita (2004): 0.2 mm gap, R113, G = 100 kg/m^{2}s, q``= 20 kW/m^2

Where:

$$F = \sqrt{\frac{\rho_G}{\rho_L - \rho_G}} \frac{U_{SG}}{D\, g \cos\beta} \tag{2.1}$$

$$T = \left[\frac{\left[\left| dP/dx \right|_{SL} \right]}{(\rho_L - \rho_G)\, g \cos\beta} \right]^{1/2} \tag{2.2}$$

$$X = \left[\frac{\left[\left| dP/dx \right|_{SL} \right]}{\left[\left| dP/dx \right|_{SG} \right]} \right]^{1/2} \tag{2.3}$$

It is to be noted that the specific formulations used in developing the regime transition criteria reflect the distinction between surface tension driven regimes, such as Bubble and Intermittent flow, and shear force driven regimes, such as Stratified and Annular flow. The models contain little empiricism, and, therefore, can be applied to most fluids and be extrapolated to conditions other than water-air and water-steam flowing in 25 mm and larger pipes, which were used in the original experimental verification of the approach, Shoham (1982), Taitel and Dukler (1987).

In embracing the use of this flow regime map, it must, nevertheless, be recognized that the Taitel-Dukler methodology relies on adiabatic models that ignore the thermal interactions between phases, the pipe, and the environment all of which are present in diabatic systems, in which heat is added or extracted from the flowing two-phase mixture. Such an adiabatic model can provide a reasonable prediction of flow regimes if the applied heat flux is low, but high wall heat flux could be expected to shift the transition boundaries for both the Bubble/Intermittent and Stratified/Intermittent interfaces in comparison to that predicted by an adiabatic model, Bar-Cohen

et al (1987). Nevertheless, the model has proven to be exceedingly useful and has demonstrated its first-order accuracy in numerous studies, including those performed by Taitel and Dukler (1978), and Frankum et al. (1997).

Consequently, the physics-based models used in the Taitel and Dukler flow regime maps, originally developed for water-air and water-steam mixtures flowing in 25 mm and larger pipes, would appear to offer the best basis for determining the prevailing flow regimes in evaporating refrigerant and dielectric liquid flow within miniaturized channels and for facilitating the extrapolation of available macro-tube water-based correlations to such dielectric liquid microgap coolers. Although the non-dimensional maps provide a compact way to represent specific transitions, for ease of interpretation and a more comprehensive view of the flow regime distribution, subsequent sections will use the dimensional form of the Taitel and Dukler flow regime map, with superficial velocity coordinates.

2.1.1 Application to Miniature Channels

Figure 2.2 displays an example of a Taitel and Dukler flow regime map for R-113 flowing in a horizontal channel with a 1mm hydraulic diameter, in which the zones occupied by the four primary flow regimes are identified. The locus traversed by the Yang and Fujita (2004) data for such a channel, are shown on the superficial velocity coordinates of the map. It may be easily seen that, while all four regimes are well represented on this map, the locus of the data for this 1mm channel data falls largely in the Annular regime, as empirically observed by Yang and Fujita (2004).

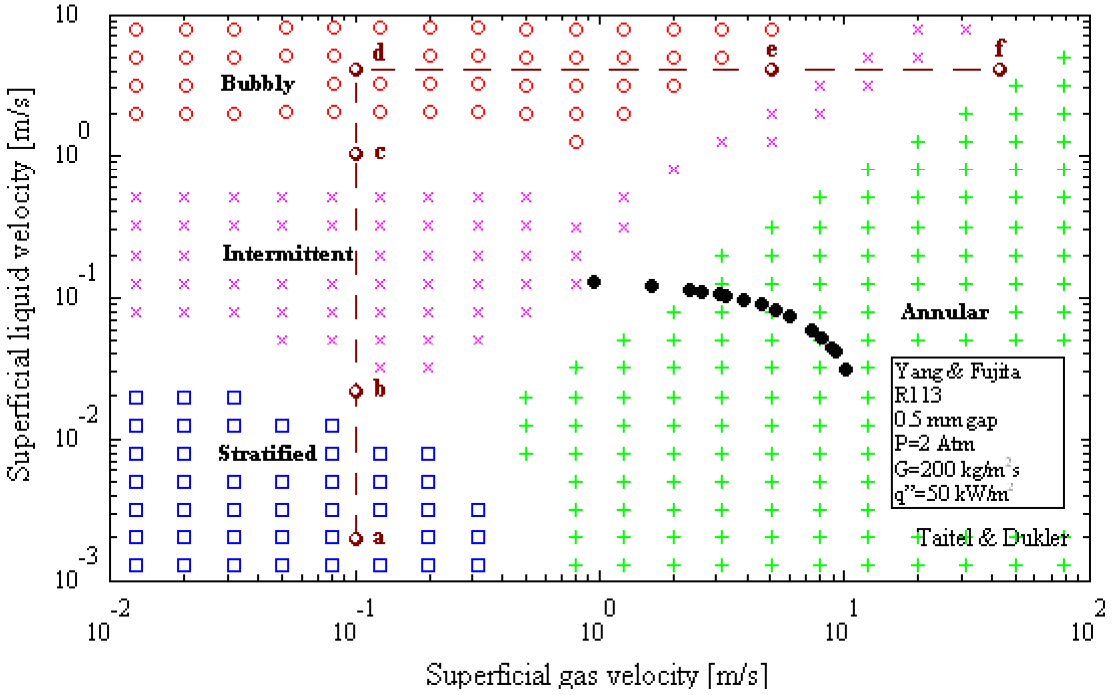

Figure 2.2 Taitel-Dukler flow regime map for the flow of refrigerant R113 in a 1 mm microgap channel. Data of Yang and Fujita (2004)

In the Stratified flow regime, seen in the lower left corner of the map, point (a) for example, gravity acts to separate the phases, with the liquid flowing along the bottom of the channel and the vapor along the top. Following Taitel and Dukler, it may be argued that increasing the superficial liquid velocity, as can be caused by a higher liquid flow rate or smaller diameter, will lead to a thicker layer of liquid in the channel and allow waves which develop on the liquid–vapor interface to more easily reach the top of the channel and form liquid "bridges" that can then "trap" vapor slugs and produce the phase distribution associated with the Intermittent (slug) flow regime. For the conditions of Figure 2.2, this transition occurs at a superficial liquid velocity of about 0.02 m/s for a superficial gas velocity of 0.1 m/s, as in point (b).

Further increasing the superficial liquid velocity, while keeping the superficial gas velocity constant at 0.1 m/s, will force the liquid to occupy more and more of the channel volume, disrupting the vapor slugs, creating dispersed bubbles, and leading to the appearance of Bubble flow. The Taitel and Dukler model predicts this transition to occur at a superficial liquid velocity of approximately 1 m/s, as in point (c), and places the Bubble regime across the top of the flow regime map.

Selecting a point deeper in the Bubble regime, point (d), with a superficial liquid velocity of 2 m/s and a superficial gas velocity of 0.1 m/s, and assuming downstream net vapor generation, as will occur in an evaporator, leads to a progressive increase in the superficial gas velocity along with growth in the number and size of the vapor bubbles. These bubbles can then be expected to agglomerate into slugs and lead to a transition into the Intermittent flow regime – predicted by Taitel and Dukler to occur at a superficial gas velocity of approximately 5 m/s, for the stated range of liquid velocities, as shown in point (e).

With a further increase in the flow quality and, therefore, the superficial gas velocity - to an approximate value of 14 m/s - the liquid bridges separating the vapor slugs can no longer be sustained; the vapor breaks through the liquid plugs, pushing this liquid volume into the liquid layer flowing along the channel walls and transitioning into the Annular flow regime, as in point (f). To sustain the annular flow regime, the vapor velocity must then be capable of providing sufficient shear stress to prevent the liquid film from rupturing or - for a horizontal channel - separating by gravity from the upper wall. At high flow qualities the necessary shear force is

generated by the high vapor velocity in the core and, in a diabatic channel experiencing evaporation, the Annular regime persists until all the liquid is evaporated.

Having established the applicability of the Taitel and Dukler methodology to a refrigerant flowing in a miniature channel, it is instructive to explicitly examine the channel diameter effect on the prevalence and relative position of the flow regimes on the superficial velocity coordinates. Figure 2.3 provides the flow regime maps for refrigerant R113, flowing in channels with diameters from 100 mm down to 0.1 mm, and displays the loci for mass fluxes of 50, 100, 200, and 400 kg/m^2s and qualities that range from 10% to 90%**.** A close examination of the four flow regime maps reveals no abrupt changes in the regime boundaries at progressively smaller channel diameters, but rather a gradual expansion of the Annular regime to lower superficial velocities and of the Bubble and Intermittent regimes to lower superficial liquid velocities. Consequently, as the channel diameter decreases from 100 mm to 0.1 mm, the Stratified zone is seen to shrink towards the origin of the map (lower left corner) while the Annular regime grows to include the operating domain for all 4 mass fluxes. Thus, in agreement with many empirical observations**,** the Taitel and Dukler map reveals that it is extremely difficult to sustain stratified flow of refrigerants in sub-millimeter channels, and that Annular flow dominates much of the operating envelope of such miniaturized heat transfer devices, Yang and Fujita (2004), Lee and Lee (2001). More specifically, the transition from Intermittent to Annular flow in the 0.1 mm diameter channel occurs at superficial liquid velocities of less than 0.005 m/s, which – together with superficial vapor velocities below 0.1 m/s - corresponds to a mass flux of just 73 kg/m^2-s and a saturated liquid mass flow rate of $7.8x10^{-9}$ kg/s at the inlet, of little interest in microgap cooler applications.

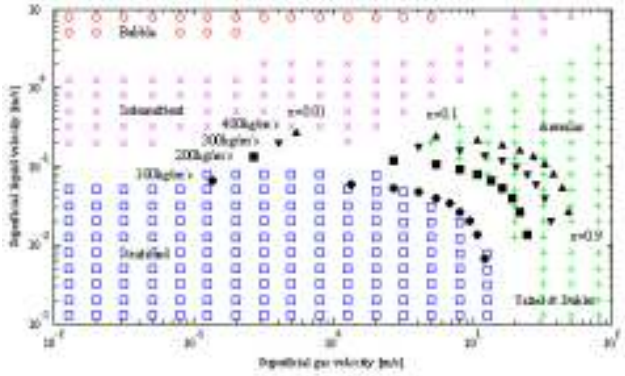

(a): D=100mm

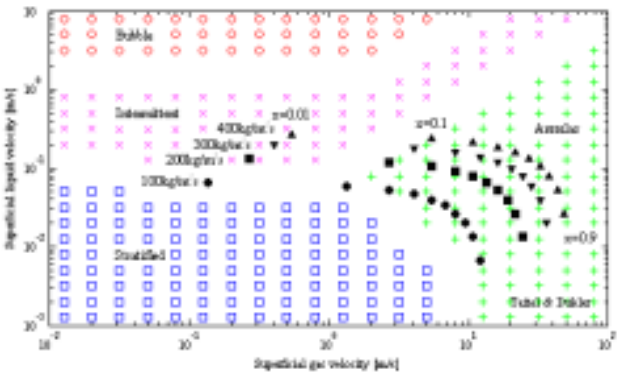

(b): D=10mm

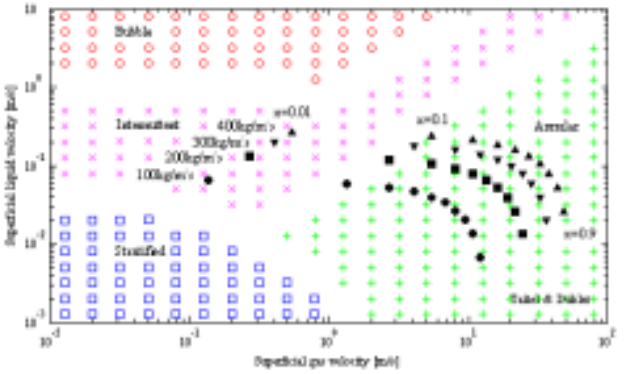

(c): D=1mm

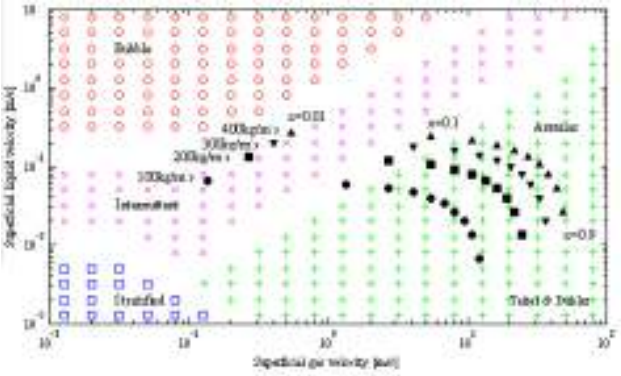

(d): D=0.1mm

Figure 2.3 Taitel-Dukler flow regime maps for refrigerant R113 flowing in a horizontal channel - diameters ranging from 100 mm To 0.1 mm (atmospheric pressure.)

These and similar results for miniature vertical channels with two-phase refrigerant flow suggest that, although the primary two-phase flow regimes encountered in large channels also occur in miniature channels, Annular flow becomes more prevalent as the channel diameter decreases and appears to dominate two-phase flow in microgap channels of approximately 0.1 mm diameter. The channel geometry at which Annular flow becomes the dominant flow regime, can perhaps serve as an approximate, regime-based criterion for microchannel behavior, i.e. diameter equal to 0.1 mm.

As a consequence of the growing dominance of Annular flow in miniature channels, correlations and operating experience derived from centimeter-scale refrigerant channels – that are not informed by flow regime observations or prediction - can not be easily extrapolated to sub-millimeter channels. Alternatively, it may be possible to extrapolate heat transfer data from large to miniature channels within the same flow regime.

2.1.2 Application to Miniature Tubes

A comparison of the more than 2200 flow regime observations documented by Revellin et al (2005) to the predictions of the Taitel-Dukler flow regime methodology revealed that 67% of the empirically observed flow pattern data were correctly identified.

The two-phase flow regime observations described earlier in Table 2.1 were compared to the predictions of the Taitel-Dukler Flow regime map. As can be seen in Figure 2.4, displaying the loci of distinct mass fluxes with symbols chosen to reflect the experimentally observed flow regimes, in each of 3 operating conditions, agreement in the dominant flow regimes can be observed between the data and the Taitel-Dukler model. Expanding this comparison to include the full Revelin et al (2005) dataset of flow regime observations, revealed that 67% of the 2239 empirically observed flow pattern data were in the theoretically predicted regime. However, it must be noted, that the location and slope of the observed Bubble to Slug transition boundary, with a somewhat sparse data sub-set, is not well predicted by Taitel-Dukler. Thus, 48% of the Slug

data and 92% of the Annular data, but only 2% of the limited Bubble data, is correctly predicted by Taitel-Dukler

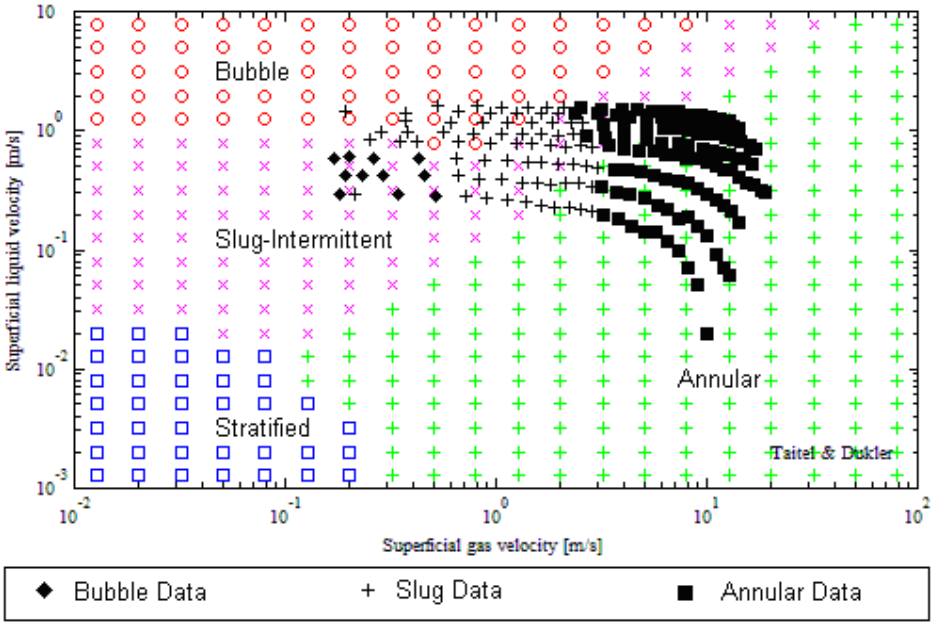

Figure 2.4 Taitel-Dukler flow regime map for data of R134a in 509 micron channel. T=26 ^{o}C, $T_{Inlet-sub}$=3 ^{o}C, G= 350 – 2000 kg/m^{2}s

More of the Revellin et al (2006) two-phase flow data with visual observations is displayed in Figure 2.5 and Figure 2.6

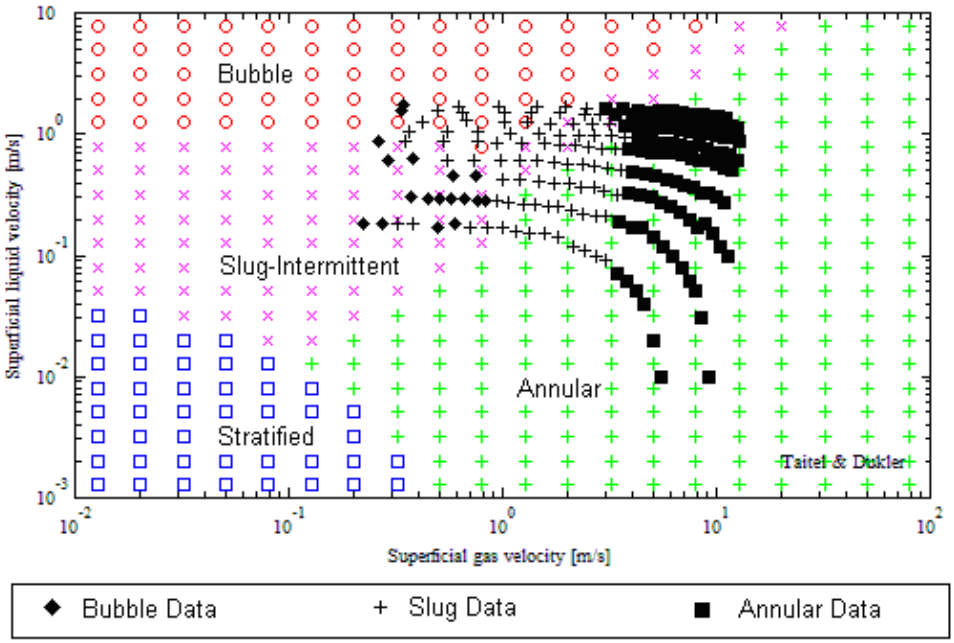

Figure 2.5 Taitel-Dukler flow regime map for data of R134a in 790 micron channel. T=30 ^{o}C, $T_{Inlet-sub}$=3 ^{o}C, G= 200 – 2000 kg/m^{2}s

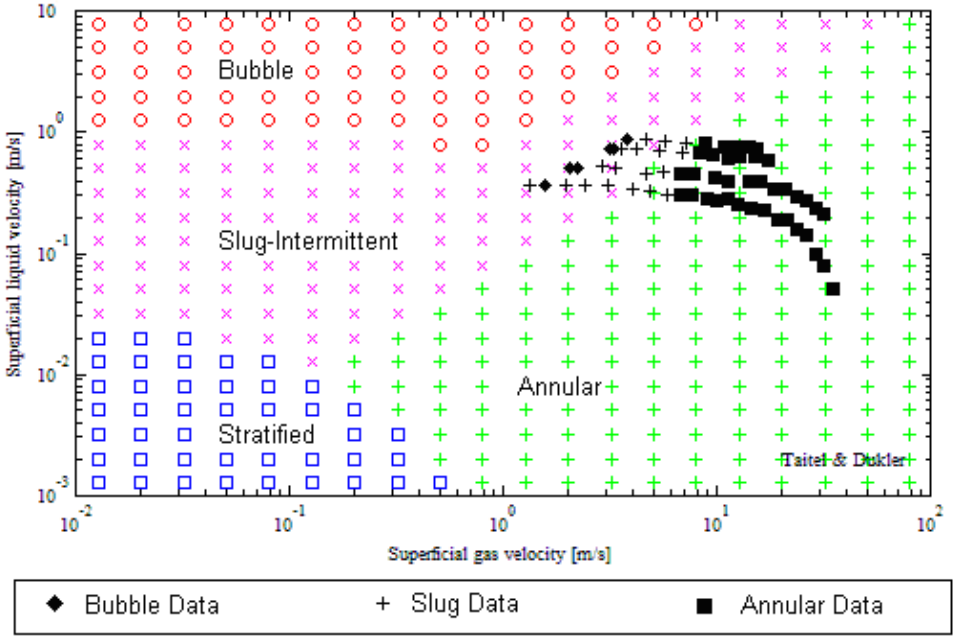

Figure 2.6 Taitel-Dukler flow regime map for data of R245fa in 509 micron channel. T=35 ^{o}C, $T_{Inlet-sub}$=6 ^{o}C, G= 500 – 1200 kg/m^{2}s

2.2 Weismann Intermittent to Annular Transition

In addition to the Taitel and Dukler mapping methodology, the literature describes other analytical approaches to the identification of two-phase flow regime transitions. Given the importance of the Intermittent-to-Annular transition to the flow of refrigerants in miniature channels, it is appropriate to single out the work of Weismann et al (1979) who correlated this transition in terms of the Froude number and the Kutadelaze number. The boundary between these two regimes in the data gathered by these investigators, as well as data of Simpson et. al (1977), were well fitted by:

$$1.9(V_{SV}/V_{SL})^{1/8} = Ku^{0.2}Fr^{0.18} = \left(\frac{V_{SV}\rho_V^{1/2}}{\left[g(\rho_L-\rho_V)^{1/4}\right]}\right)^{0.2}\left(\frac{V_{SV}^{2}}{g\,d}\right) \qquad (2.4)$$

This transition boundary is plotted for the flow of R113 in a 0.8 mm hydraulic diameter channel in Figure 2.7, using the Taitel and Dukler superficial velocity coordinates. The area on the map shaded with light yellow represents the Annular regime according to Weisman et al, with the Intermittent zone to the left of the Annular domain. The Weismann et al Annular zone is, thus, expanded to include a substantial segment of the Taitel and Dukler Intermittent and Bubble zones, at the higher superficial gas and liquid velocities, and is less extensive than Taitel and Dukler at the lower superficial liquid velocities.

It is also noticeable that the slope of this Weismann Intermittent/Annular boundary is opposite to the Taitel-Dukler Intermittent/Annular boundary, transitioning from (wavy) Stratified behavior to Annular flow rather than from the Bubble and Slug flow domains into Annular flow. Regrettably, much of the limited microgap refrigerant data currently available in the literature, including the Yang and Fujita (2004) data, shown in Figure 2.7, falls in the Annular domain common to both maps, and clusters around the intersection of these two transition boundaries, making it difficult to judge the relative accuracy of these two distinct transition criteria.

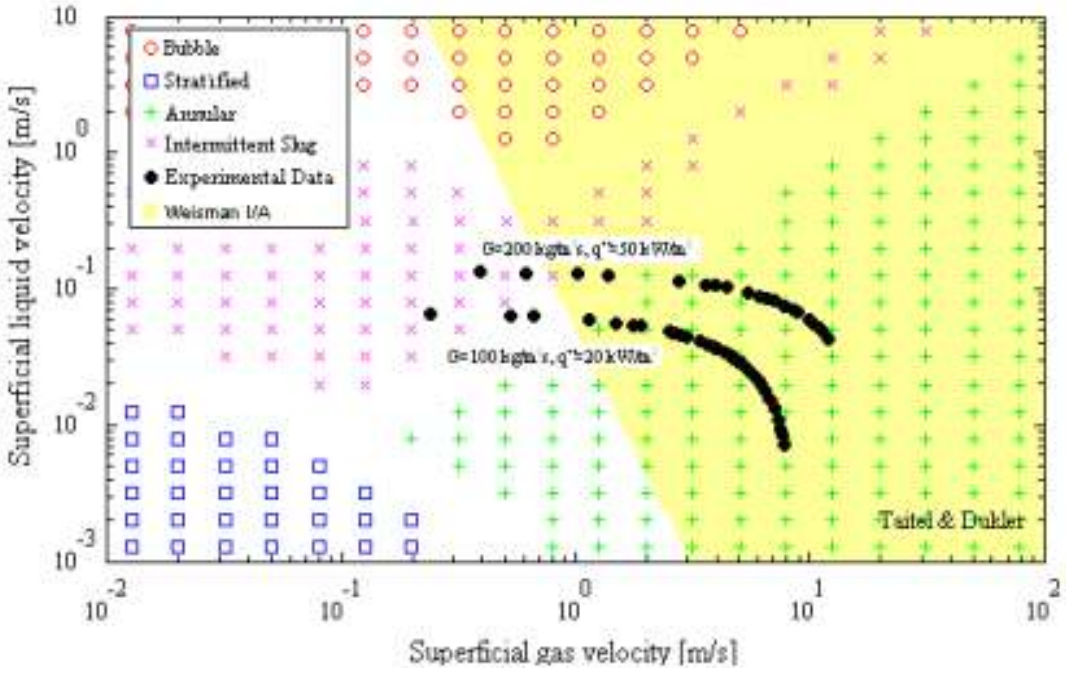

Figure 2.7 Flow regime map for R113 flowing in a 0.4 mm channel, including the Weisman bounday - Yang and Fujita data (2004)

2.3 Tabatabai and Faghri

Tabatabai and Faghri (2001) proposed a modification to the Taitel and Dukler flow regime map based on a criterion for the transition from surface tension dominated behavior to shear-dominated behavior, as displayed on the superficial velocity coordinate of the map in Figure 2.8. Since it is the Bubble and Intermittent regimes that can be expected to reflect the dominance of surface tension effects, in this map as well as other maps for miniature passage configurations, this new regime is seen to combine large swaths of the Bubble and Intermittent regimes (with a small section of the Stratified domain) into a "surface tension domain" that occupies the upper left corner of the Taitel and Dukler flow regime map. At larger vapor and lower liquid velocities than captured in this domain, corresponding to the space occupied by the vast majority of the available refrigerant data, the Tabatabi and Faghri map leaves the Taitel and Dukler regime boundaries unaltered.

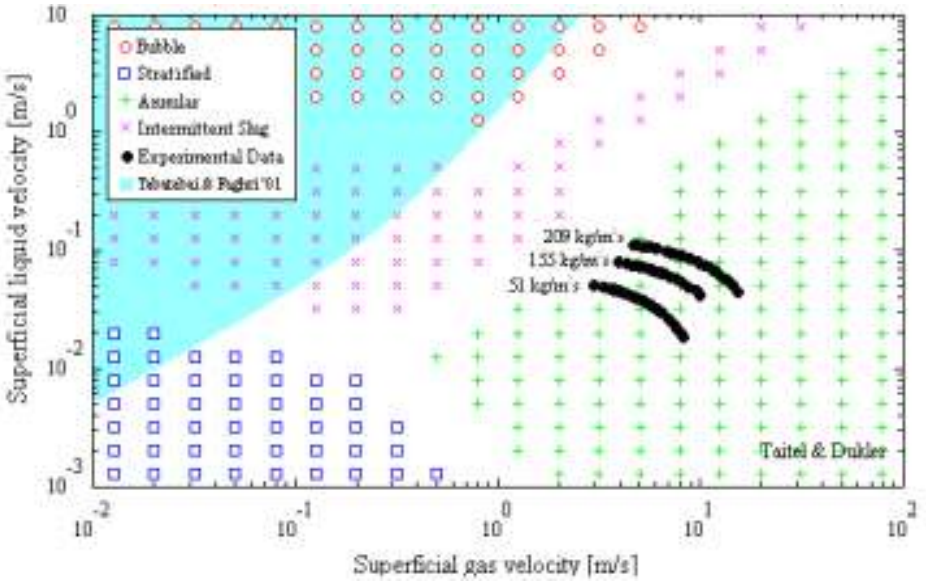

Figure 2.8 Flow regime map for the flow of R113 in a 0.4 mm gap channel , including the Tabatabai and Faghri boundary - data of Lee & Lee (2001), q''= 3 – 10 kW/m^2, Pressure = 128 kPa

2.4 Empirical Flow Regime Maps

In their 2006 paper, Revellin and Thome proposed a new diabatic flow regime map for evaporating flow in microchannels. They used an optical technique to observe the prevailing flow regime at the exit of single 0.5 mm and 0.8 mm diameter glass tubes, serving as the evaporator section of their test apparatus. Coupling visual observations with measured bubble frequencies, they identified 3 primary flow regimes: Isolated Bubble, Coalescing Bubble, and Annular flow.

The vapor quality at which the maximum bubble frequency occurs marks the transition from the Isolated Bubble regime to the Coalescing Bubble regime and was correlated by Revellin and Thome in terms of the Webber number, Reynolds number, and the Boiling number, as:

$$x_{IB/CB} = 0.763\left(\frac{\mathrm{Re}_{LO}\ Bg}{We_{GO}}\right)^{0.41} \tag{2.5}$$

The transition from the Coalescing Bubble regime to the Annular regime was given by:

$$x_{CB/A} = 0.00014\ \mathrm{Re}_{LO}^{1.47}\ We_{LO}^{-1.23} \tag{2.6}$$

A new version of Katto-Ohno (1984) CHF correlation was used to correlate the transition from Annular flow to Dryout, as proposed by Wojtan et al (2005).

$$q_{crit} = 0.437\left(\frac{\rho_V}{\rho_L}\right)^{0.073} We^{-0.24}\left(\frac{L}{D}\right)^{-0.72} G\, h_{LV} \qquad (2.7)$$

These three transition boundaries, with their observed error bands of 15 % to 20 %, are plotted in Figure 2.9, Revellin and Thome (2006), on mass flux and vapor quality coordinates. All three transitions are seen to follow a hyperbolic trajectory, leading to progressively lower qualities at the respective transition as the mass flux increases. Moreover, the Annular flow regime is again seen to dominate the operational domain of the test channel and to become more dominant as the mass flux increases, with transition to this regime occurring at qualities below 10 % for mass fluxes in excess of 1200 kg/m^{2}s.

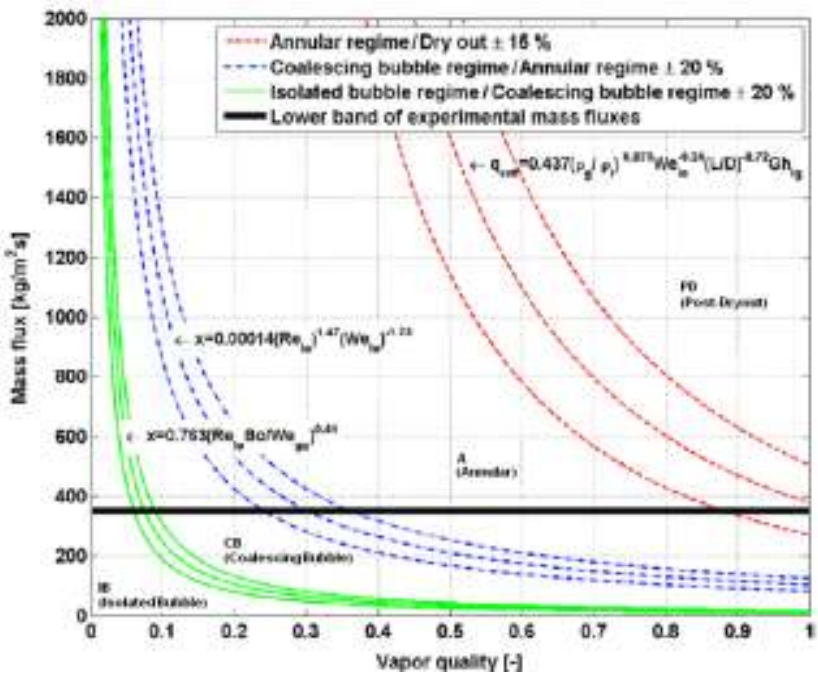

Figure 2.9 Diabatic flow regime map for evaporating R134a flow in circular uniformly heated 0.5 mm channel, (L = 70 mm, T_{sat} = 30 ^{o}C, q``=50 kW/m^2), Revellin and Thome (2006)

The Serizawa et al. (2001) study of 50 micron and 20 micron channels with steam-water and air-water flow, respectively, deals with perhaps the smallest channels reported in the literature. They observed the anticipated progression in flow regimes from Bubble flow to Intermittent (slug) flow and – after a small perturbation – transition into Annular (dispersed droplet) flow. In the 20 micron channel with air-water flow they did, however, observe a "liquid ring" and "liquid lump flow," domain, displaying significant spatial variations in liquid film thickness, for a range of qualities just prior to the emergence of the more traditional uniform film thickness annular flow. Nevertheless, even in this truly "micro" channel flow, the three primary flow regimes – Bubble, Intermittent (Slug), and Annular flow were in clear evidence.

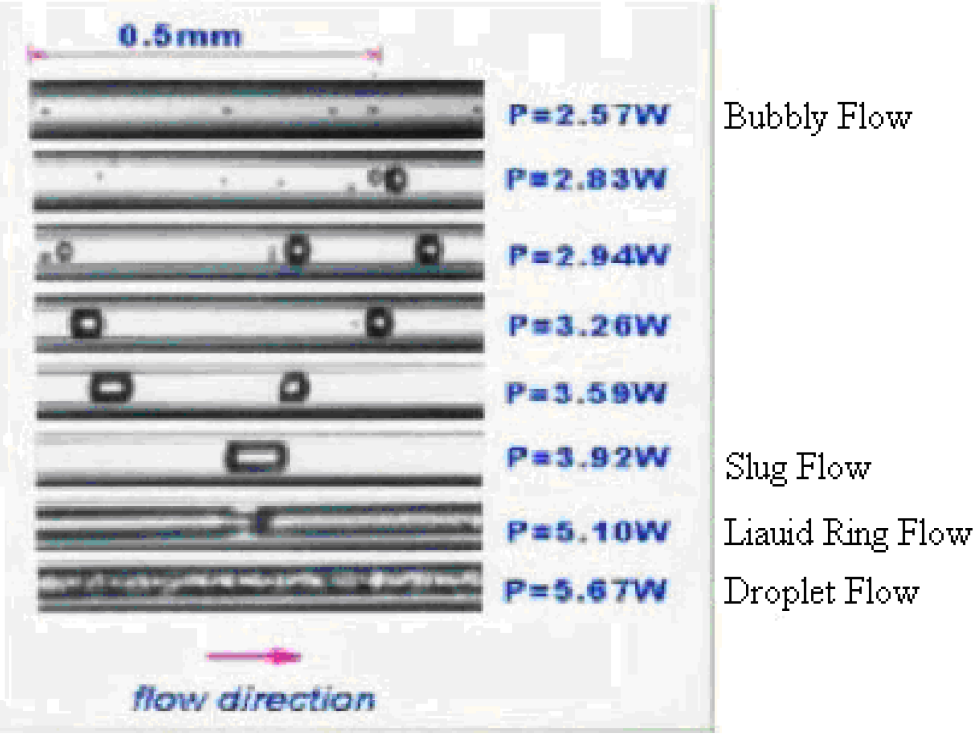

Figure 2.10 Observed steam-water flow in 50 micron channels, Serizawa et al (2001)

The importance of the flow regime in determining the heat transfer coefficients in two-phase flow was investigated in a study by Ghajar et al (2006), who performed a systematic investigation of two-phase heat transfer in a 27.9 mm stainless steel horizontal pipe with a length to diameter ratio of 100. A flow of air-water mixtures was used to find a heat transfer correlation that accounts for the flow pattern in the pipe. The two-phase heat transfer coefficient was found to be influenced by the flow pattern – through a flow pattern factor, F_p, introduced into the correlation - the superficial liquid Reynolds number, Re_{LS} , representing the liquid flow rate, and the superficial gas Reynolds number, Re_{GS}, representing the gas flow rate. The flow pattern factor was defined as:

$$F_P = \tilde{S}^2_{L,eff} = \left(\frac{S_{L,eff}}{\pi D} \right)^2 = (1-\alpha) + \alpha F_S^2 \tag{2.8}$$

Where F_s is the shape factor defined as:

$$F_S = \frac{2}{\pi} \tan^{-1} \left(\sqrt{\frac{\rho_G (V_G - V_L)^2}{g D (\rho_L - \rho_G)}} \right) \tag{2.9}$$

Ghajar et al. carefully mapped and photographed the prevailing flow regimes in their horizontal test pipe, as displayed in Figure 2.11. While the Stratified, Slug, and Annular regimes are easily recognizable from the previous discussion, an additional set of sub-regimes were found to exist in the region between the Slug and Annular regimes. In the coarser Taitel and Dukler regime classification, these sub-regimes along with Slug flow would fall into the Intermittent flow regime, which clearly dominates the two-phase behavior of this relatively large pipe in the range tested.

In the data gathered by Ghajar et al., the heat transfer coefficient was found to increase at low Re_{GS}, which corresponds to the Intermittent-slug flow regime, then experience a positive change of slope when approaching Annular flow, and then shift to higher values as the Re_{GS} increases further and enters into the Annular flow regime. The heat transfer correlation proposed by the authors was expressible as:

$$h_{TP} = F_P h_L \left\{ 1 + C \left[\left(\frac{x}{1-x} \right)^m \left(\frac{1-F_P}{F_P} \right)^n \left(\frac{\mathrm{Pr}_G}{\mathrm{Pr}_L} \right)^P \left(\frac{\mu_G}{\mu_L} \right)^q \right] \right\} \tag{2.10}$$

where h_L comes from the Sieder and Tate (1936) correlation for turbulent flow given as:

$$h_L = 0.027 \mathrm{Re}_L^{4/5} \mathrm{Pr}_L^{1/3} \left(\frac{k_L}{d} \right) \left(\frac{\mu_B}{\mu_W} \right)_L^{0.14} \tag{2.11}$$

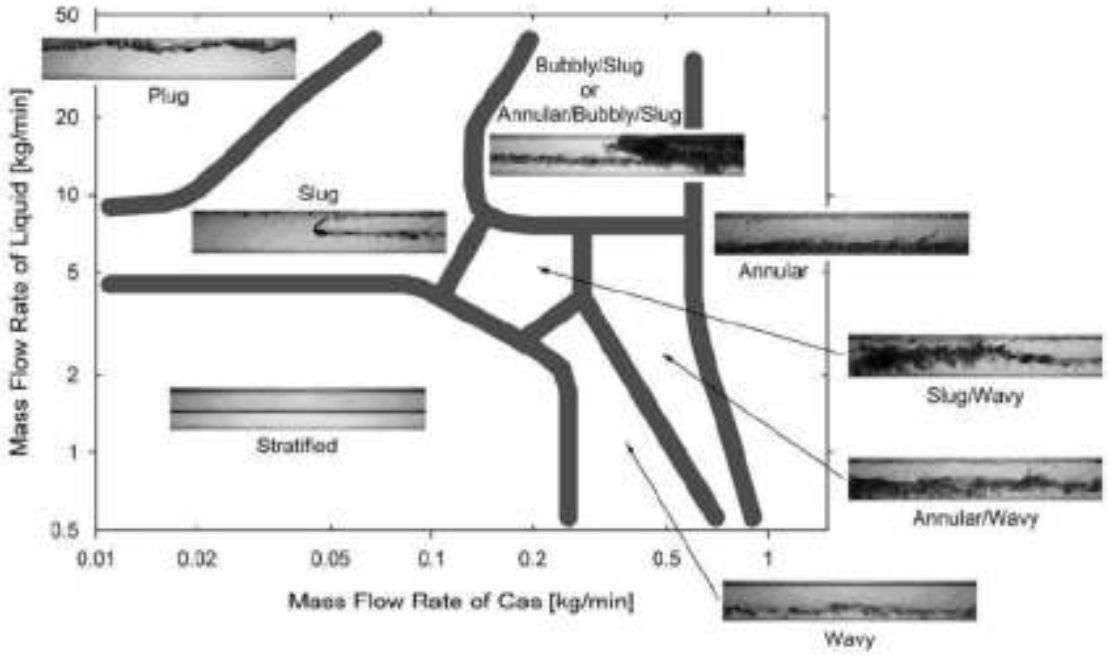

Figure 2.11 Flow regime map for 30 mm horizontal pipe, Ghajar (2006)

2.5 Ullmann-Brauner Flow Regime Maps

Ullmann and Brauner (2007) reexamined the effect of the channel diameter on the flow regime transitions and suggested that new mechanistic models be expressed in terms of the non-dimensional Eötvös number, Eo_D, defined as:

$$Eo_D = \frac{(\rho_L - \rho_V) g \, D^2}{8\sigma} \tag{2.12}$$

More specifically, Ullmann and Brauner suggested that in small Eötvös Number systems (of the order of 0.04), the negligibly small bubble velocity, even in vertical systems, leads to flow regimes resembling those obtained in conventional channels under microgravity conditions. They used the experimental flow regime data presented by Triplett et al (1999) for air-water in 1.097 mm Pyrex pipe, corresponding to an Eötvös number of 0.021, to calibrate and determine the efficacy of this approach for small Eo_D configurations.

The Ullman-Brauner flow regime map describes 5 flow regimes; Dispersed Bubble, Bubble, slug, aerated slug, and Annular.

2.5.1 Transition to Dispersed Bubble Flow

The transition into the Dispersed Bubble regime was assumed to occur when the turbulence in the continuous phase is sufficient to stabilize the dispersed phase in the form of spherical bubbles. For liquid-vapor flow, the maximum bubble size, d_{max}, should then be smaller than a

critical size, d_{crit}, of coalescing bubbles. The maximum bubble size for a dilute dispersion of coalescing bubbles, $d_{max,o}$, was estimated by Ullmann and Brauner by equating the momentum exerted by the turbulent eddy relative to the surface tension. Specifically, the maximum bubble size in a dense dispersion, $d_{max,}$ was estimated based on equating the turbulent energy flux and the flux of the surface energy generated in the recurrently renewed dispersion. The greater value of these two estimates was taken as the maximum bubble size in the system.

The critical size of the coalescing bubble was taken as the smallest of three characteristic values: the size of a deformable bubble, $d_{c\sigma}$, the size of a floating bubble due to buoyancy, d_{cb}, and a value that was set as half the channel diameter. This transition was summarized by Ullmann and Brauner (2007) as follows:

$$d_{\max} = MAX\left\{d_{\max,o}, d_{\max,\varepsilon}\right\} \le d_{crit} = MIN\left\{d_{c\sigma}, d_{cb}, 0.5D\right\} \tag{2.13}$$

2.5.2 Bubble to Slug Flow Transition

The Bubble-to-Slug transition value of the liquid superficial velocity was found as:

$$U_L = \frac{1-(\varepsilon_G)_{crit}}{(\varepsilon_G)_{crit}} U_G \tag{2.14}$$

where ε_G is the critical void fraction at which this transition occurs. It was assumed by Ullmann and Brauner that the void fraction marking the transition from Bubble flow, with spherical bubbles, to Slug flow, with elongated bubbles, can be obtained from simple geometrical

considerations relating to the void fraction of trains of contacting bubbles. This led them to conclude that the Bubble to Slug transition would occur when the bubble diameter was *half* the pipe diameter, corresponding to a void fraction value of 0.16. However, a void fraction value of 0.15 was eventually used in the Ullmann and Brauner model.

2.5.3 Transition from Stratified to Annular Flow

Ullmann-Brauner attributed the transition from Stratified to Annular flow to two mechanisms:

Loss of Stability of the Stratified Flow Structure: For thin liquid films flowing in horizontal pipes, the breakdown in Stratified Flow occurs at a critical superficial gas velocity of:

$$U_G \geq C_1 \left[\frac{D\ \Delta\rho\ g\ \cos\beta + D\ \sigma\ k^2}{\rho_G} \right]^{0.5} \tag{2.15}$$

where k is the typical long wave number :

$$k \approx 2\pi / D \tag{2.16}$$

and

$$C_1 \approx 0.63 \left(\frac{h}{D} \right)^{-0.25} \tag{2.17}$$

and h is the height of the liquid layer in a stratified flow. The application of this criterion requires knowledge of the liquid layer thickness for given gas and liquid flow rates (assuming steady and fully developed stratified flow)

Drop Entrainment. Alternatively, it may be argued that the annular film is formed due to impingement of liquid drops, entrained from the wavy interface of the stratified liquid layer by the inertia of the fast moving core gas flow. The critical relative velocity between the phases – leading to entrainment – was expressed as:

$$\Delta u_G = u_G - u_L \geq 4.36\left[\frac{\sigma \Delta\rho \cos\beta}{\rho_G^{\,2}}\right]^{1/4} F(on) \tag{2.18}$$

where

$$F(On) = \left\{1 + 1.443\,(N_{vd}\cos\beta)^{0.4}\right\}^{0.5} \tag{2.19}$$

and

$$N_{vd} = \frac{\mu_L^{\,4}\,\Delta\rho\, g}{\rho_L^{\,2}\,\sigma^3} \tag{2.20}$$

Ullman and Brauner (2007) described these as two competing mechanisms. For a given liquid velocity, u_L, the smaller of the two predicted values of u_G, was assumed to dominate.

2.5.4 Transition from Slug to Annular Flow

The transition from Slug to Annular flow was attributed by Ullman-Brauner to the prevention of *Wave Bridging,* which would otherwise act to deliver liquid from the lower layer to the upper layer of liquid, thus creating a liquid plug. To assure that such bridging does not occur, they determined that the superficial gas velocity, U_G, needed to exceed:

$$U_G \geq \tilde{\varepsilon}\left[\tilde{\varepsilon}\frac{\mu_L}{\mu_G}+2\right]U_L \tag{2.21}$$

Where

$$\tilde{\varepsilon} = \frac{1-\varepsilon_L^{crit}}{\varepsilon_L^{crit}} \tag{2.22}$$

Ullmann and Brauner found an average liquid holdup (ε_L^{crit}) of 0.4 to be sufficient to maintain the Annular flow. The empirical regime observations of Revellin and Thome (2007) were next compared to the Ullmann-Brauner two-phase flow regime predictions, based on their proposed Bubble-to-Slug, Stratified-to-Annular, and Slug-to-Annular flow regime transitions. As may be seen in Figure 2.12 the Slug-to-Annular transition is nearly vertical at low superficial liquid velocities and curves to the left at higher values of the liquid superficial velocity, as the Bubble flow regime is approached. Interestingly, this curvature in the Slug-Annular boundary does not appear to improve the predictability of the flow regimes prevailing in the Revellin et al test sections. It is also to be noted that, while the transition boundary from Bubble flow to Slug flow appears to display the appropriate slope, it is far to the left of the empirically observed transition.

Despite these discrepancies, the Ullmann-Brauner model correctly predicted the appropriate flow regime for 81% of the full Revellin and Thome (2007) dataset of flow regime observations. The Ullmann-Brauner model achieved this accuracy by offering improved predictability in the Annular and Slug regimes, relative to Taitel and Dukler, properly accounting for 99% of the Annular data and 74% of the Slug data, respectively, but failing to correctly identify any of the 182 Bubble data points. While the Ullmann-Brauner model was, thus, able to predict

the slope of the Slug to Annular transition, for the smaller diameter tube (0.509 mm), it predicted the transition to Annular flow to occur at a lower vapor quality than observed by Revellin et al.

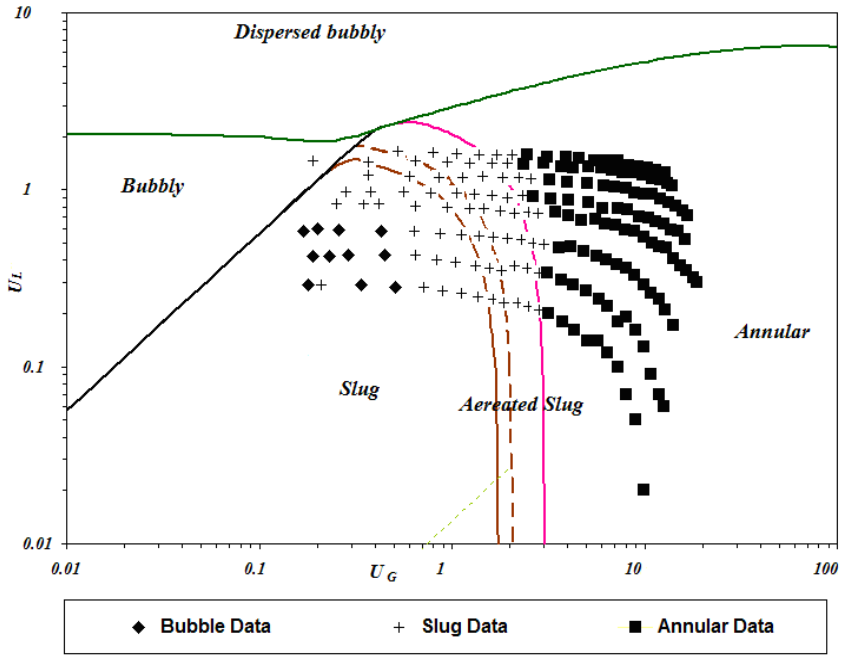

Figure 2.12 Ullmann – Brauner flow regime map for data of R134a in 509 micron channel. T=26 ^{o}C, $T_{Inlet-sub}$=3 ^{o}C, G= 350 – 2000 kg/m^{2}s

More data from Revellin and Thome (2005) which was presented in Rahim et al (2011) can be seen in Figure 2.13 and Figure 2.14.

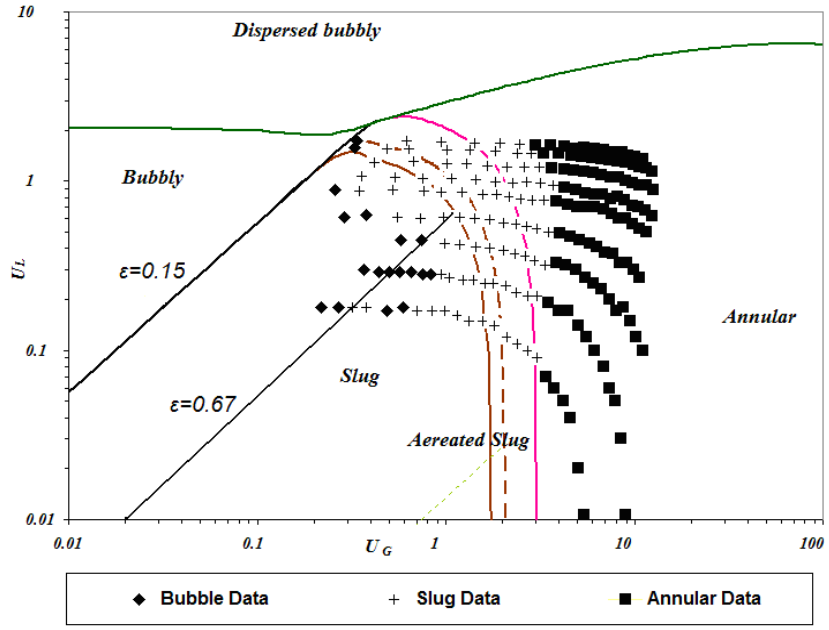

Figure 2.13 Ullmann – Brauner flow regime map for data of R134a in 790 micron channel. T=30 ^{o}C, $T_{Inlet\text{-}sub}$=3 ^{o}C , G= 200 – 2000 kg/m^{2}s

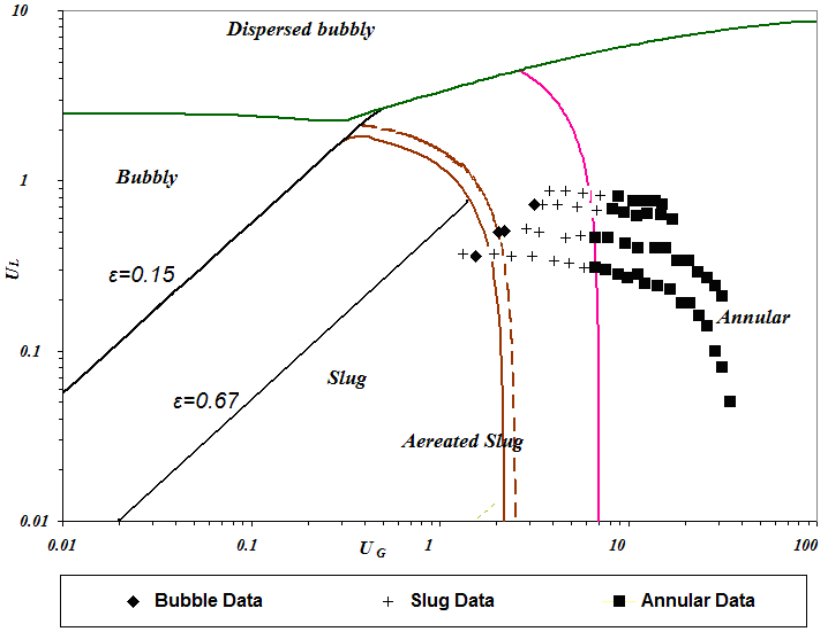

Figure 2.14 Ullmann – Brauner flow regime map for data of R245fa in 509 micron channel. T=35 ^{o}C, $T_{Inlet-sub}$=6 ^{o}C, G= 500 – 1200 kg/m^{2}s

2.6 Flow Regime Map Modifications for Miniature Channels

The preceding has established the efficacy of using the classical Taitel-Dukler map to determine the prevailing flow regimes in the two-phase flow of refrigerants in miniature tubes. Despite the significant difference in scale between the majority of the data originally used to validate the Taitel-Dukler regime transitions and the sub-millimeter tubes studied herein, the dominant regime (Annular flow) and nearly 67% of the observations, were correctly identified by the Taitel-Dukler methodology. Modifications to the Bubble-to-Slug, Stratified-to-Annular, and Slug-to-Annular flow regime transitions, proposed by Ullman-Brauner (2007) yielded a further improvement and correctly identified the flow regime of 81% of the miniature tube observations.

2.6.1 Modified Bubble-to-Intermittent Transition

As previously noted, while the Ullmann-Brauner transition from Bubble flow to Slug flow appears to display the appropriate slope, it is far to the left of the empirically observed transition for the miniature tubes studied herein. However, when the boundary is modified to allow transition when the critical void fraction is 0.67, i.e. the diameter of the bubble is essentially equal to the tube diameter, the boundary moves to the right, as in Figure 2.15, capturing much of the observed Bubble data at mass fluxes of ($G \leq 700$ kg/m^{2}s), i.e. 123 out of the 182 Bubble data points at low

mass flux are now correctly predicted, yielding an agreement of 68%. However, the use of the revised Bubble to Slug transition boundary over the entire range of mass fluxes yielded less satisfactory results, since many of the Slug data points were falling in the Bubble region at moderate and high mass fluxes ($G > 700$ kg/m^{2}s).

2.6.2 Modified Intermittent-to-Annular Transition

As is visible in Figure 2.15, the nearly vertical U-B Slug-to-Annular transition at low mass fluxes is consistent with the shape of the empirically-observed boundary between these two regimes and some discrepancies are generated by the "curvature" of this boundary to the left and lower gas superficial velocities at the higher mass fluxes. Interestingly, setting the transition from Slug to Annular to occur as a vertical line at a superficial vapor velocity equivalent to that where the transition occurs at low mass flux ($G \leq 500$ kg/m^{2}s) results in a significant improvement in the predictive accuracy, with a greater fraction of the Slug data properly categorized, and the prediction accuracy rising from 74% to 84%.

Implementing this change yields an average accuracy of 84% for the Slug data and 99% for the Annular data, which results in an overall accuracy improvement from 88% to 92% for the combined Slug and Annular data.

An example of the proposed modifications in the flow regime map is shown in Figure 2.15.

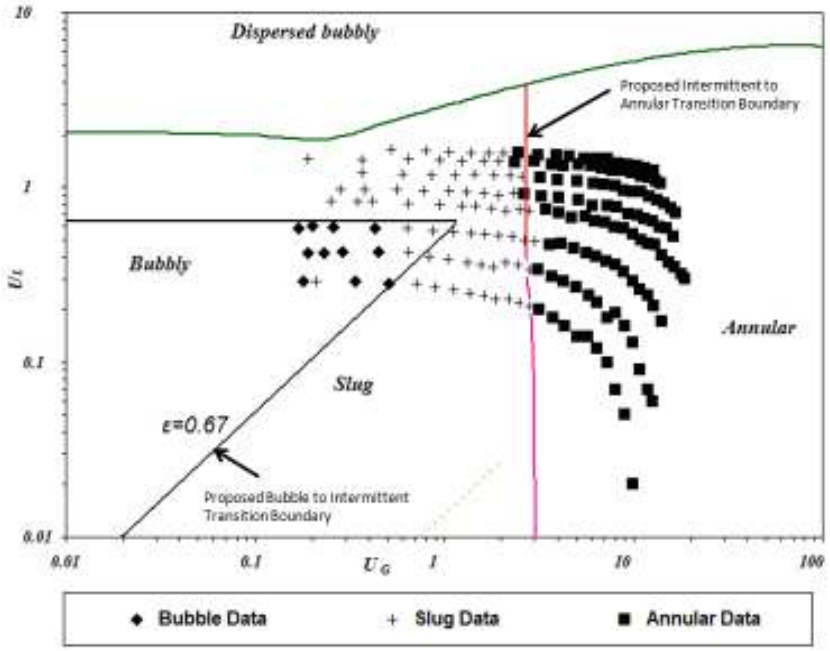

Figure 2.15 Ullmann – Brauner flow regime map, with modified transition boundaries, for data of R134a in 509 micron channel. T=26 ^{o}C, $T_{Inlet-sub}$=3 ^{o}C, G= 350 – 2000 kg/m^{2}s

2.6.3 Taitel Vertical Intermittent-to-Annular Transition Boundary – Further Modifications

As observed by Ullmann and Brauner (2007) and Thome (2006), among others, and discussed extensively by Bar-Cohen and Rahim (2009), stratification in miniature channels is generally not sustainable and this regime is confined to a vanishingly small parametric space of low superficial gas and liquid velocities. Furthermore, the role of gravity forces in small, low Eötvös number channels is almost negligible, compared to the shear and the surface tension forces (Ullmann and Brauner, 2007; Tabatabai and Faghri, 2001). It may thus be argued that further

improvements in the fidelity of the Annular/Slug flow regime boundary for miniature horizontal channels can be achieved by use of a model previously developed for vertical channels.

Taitel et al (1980) proposed a Slug to Annular flow regime boundary for upward two-phase flow in vertical tubes, based on a transition at a critical gas velocity expressed as

$$u_G = \left(\frac{4K}{3C_d}\right)^{1/4} \frac{[\sigma g(\rho_L - \rho_G)]^{1/4}}{\rho_G{}^{1/2}} \tag{2.23}$$

where K is the critical Weber number for an accelerated liquid droplet, and takes the value of 30, as suggested by Turner et al (1969).

Interestingly, when the gas velocity is replaced by the superficial gas velocity, the Annular flow regime transition criteria takes the form of equation 2.24 , yielding a constant superficial gas velocity, U_G, for a fixed fluid and operating pressure (Taitel 1980).

$$\frac{U_G \rho_G{}^{1/2}}{[\sigma g(\rho_L - \rho_G)]^{1/4}} = 3.1 \tag{2.24}$$

This transition value of U_G is found to equal 1.4m/s and 3.5m/s for R134a and R245fa, respectively.

While a vertical locus on the superficial velocity flow regime map best fits the empirical observations for the Slug to Annular transition, use of equation 2.24 was found to consistently

under predict the transition values of the present data. This trend allowed the model to predict all of the Annular data correctly, while providing an accurate prediction for only 58% of the Intermittent data. However, an increase in the critical superficial velocity by a factor of 2, providing a modified transition superficial gas velocity equal to:

$$U_G = \frac{6.2[\sigma g(\rho_L - \rho_G)]^{1/4}}{\rho_G^{1/2}} \tag{2.25}$$

or:

$$\frac{We^{1/2}}{Bo^{1/4}} = 6.2 \tag{2.26}$$

results in a significant improvement in the predictive accuracy, with a greater fraction of the Slug data properly categorized, and yielding an average accuracy of 96% for the Slug and Annular data.

An example of the proposed model is shown in Figure 2.16.

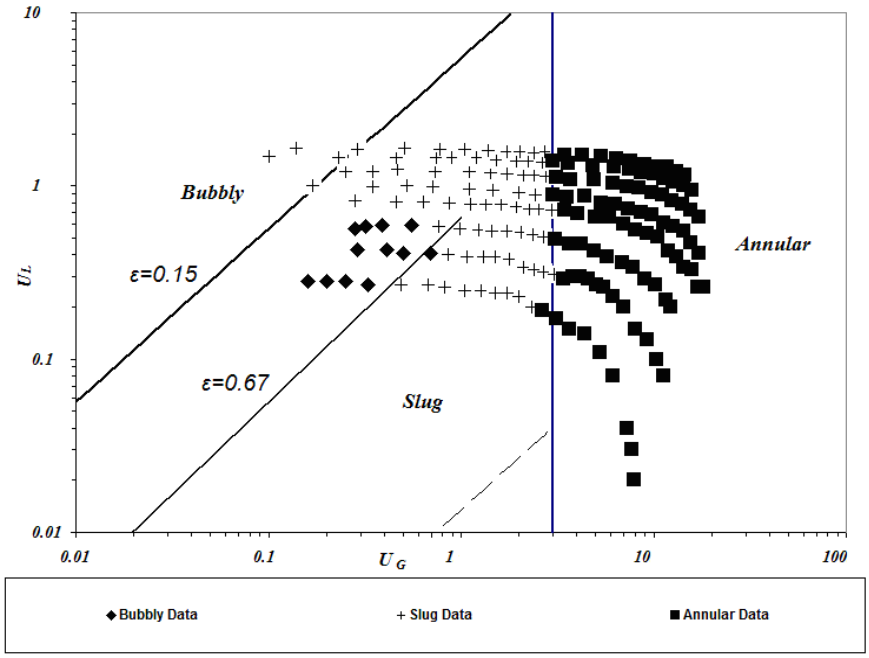

Figure 2.16 The proposed flow regime model for data of R134a in 509 micron channel. T=30 ^{o}C, $T_{Inlet\text{-}sub}$=3 ^{o}C, G= 350 – 2000 kg/m^{2}s

Specific Parametric Dependencies

To complete the comparison of observed and predicted flow regime transitions, the specific parametric dependencies associated with mass flux, fluid properties, saturation temperature, inlet subcooling, and tube diameter were examined, with the use of the modified flow regime map.

*Mass flux***:** The data were divided into three ranges of mass flux: low mass flux (200 – 700 kg/m^{2}s), moderate mass flux (1000 – 1500 kg/m^{2}s) and high mass flux (1800 – 2000 kg/m^{2}s). It was found the best Taitel-Dukler predictions occurred for the low and moderate mass flux data,

with the ability to predict the correct regime for 65% and 76% of these data points. This predictability was as low as 54% for the data points in the high mass flux range.

The best range of predictions by the Ullmann-Brauner model was achieved for the moderate mass flux data. The percentages of data points predicted correctly were 76%, 86%, and 83% for the low, moderate, and high mass flux data, respectively.

The proposed modified map was found to better predict the correct flow regime at moderate mass fluxes, with agreement of 95%, followed by the highest mass flux, with predictability of 90%, while yielding 80% for the lowest range of mass flux data.
While the Annular flow data was consistently predicted with a very good accuracy (96 %, 97%, and 93% for the low, moderate and high mass flux data, respectively), there was a variation in the predictability of the Slug data, with the lower mass flux predicted best by 97% agreement, followed by 96% for the moderate mass flux, and 88% for the low mass flux data.

*Fluid Properties***:** The two fluids used in the present study, R-134a, and R-245fa, have a considerable difference in surface tension, a key parameter in two-phase physics (see for instance, Tabatabai and Faghri 2001), with the surface tensions of R-134a and R-245fa equaling 0.007 N/m and 0.013 N/m, respectively.

It was found that the Taitel-Dukler map performed with better accuracy for R245fa than R134a, while the predictions of the Ullmann-Brauner model was nearly unaffected by this variable. Taitel-Dukler predicted the correct flow regime for 185 of the 235 R245fa data points or 79%, and

1320 out of the 2004 R134a data points for an accuracy of 66%. Ullmann – Brauner predicted correctly 83% of the R245fa data points and 81% of the R134a data points.

The newly proposed model's overall predictability was 83% and 89% of the data points of R245fa and R134a, respectively.

Saturation Temperature and Inlet Subcooling: The experiments examined in this study were run at three different values of saturation temperatures (26, 30, and 35^{o}C) with the inlet subcooling ranging from 2 to 6 ^{o}K. It was observed that the saturation temperature has a noticeable effect on the models' predictions: Taitel-Dukler providing the correct regimes for 67%, 64%, and 72% of the data points at saturation temperatures of 25, 30, and 35^{o}C. Ullmann-Brauner model performed best when predicting the flow regime for the 25^{o}C inlet temperature data, with 91% accuracy, while the 30^{o}C and 35 ^{o}C data are predicted with 77% and 85% accuracy, respectively.

The influence of the saturation temperature on the overall predictability of the newly proposed model was negligible, with 88% – 90% of the data points predicted correctly for each saturation temperature. As expected, the influence of the relatively small subcooling on the flow regimes exiting the micro-evaporator channel was very limited for both models, with no significant variation in the prediction discrepancy for the different values of inlet subcooling.

Tube Diameter: The current database consists of 1591 data points in a 0.509 mm diameter tube, and 648 data points in a 0.790 mm diameter tube. It was found for the present dataset that both existing models predicted the correct regime with better accuracy for the smaller tube. The

Taitel Dukler model predicts the correct regime with an accuracy of 70% and 62%, for the 0.509 mm and 0.79 mm data, while the Ullmann-Brauner model prediction accuracy is 86% and 70%.

Alternatively, the overall accuracy of the newly proposed modified model was not affected significantly by the tube diameter, with the proposed model predicting 88% and 87% of the 0.509 mm and 0.790 mm diameter data points, respectively.

2.7. Conclusions

Observed two-phase flow patterns for R134a and R245fa in tubes with inner diameter of 0.509 mm and 0.790 mm were compared to the predictive analytical models of Taitel and Dukler (1976), Taitel et al (1980) and Ullmann and Brauner (2007). Among the 2239 flow regime data points, no stratified flow was observed and a small number of bubble flow data existed, with Annular flow and the Intermittent (Slug) flow dominating. The Taitel-Dukler model predicted the correct regime for 67% of the data points, while the Ullmann-Brauner model predicted the correct regime for 81% of the total data points.

Despite the overall predictive accuracy of the Ullmann-Brauner regime boundaries, it was found that this model predicted the Bubble-to-Slug flow transition with a very large discrepancy and displayed progressively poorer agreement with the Slug-to-Annular transition as the mass flux increased.

It has been shown that further selective improvement in the prediction of the two-phase flow regimes for the flow of refrigerants in these miniature tubes can be obtained through modification of both the Bubble-to-Slug and Slug-to-Annular transitions. Use of a constant superficial velocity criterion for the Slug-to-Annular transition yields an overall agreement of 88%.

The assumption that the Bubble-to-Slug transition occurs when the bubble diameter equals the tube diameter, yields a good agreement at a low mass flux values, predicting the correct regime for 77% of the Bubble data points. The predictability of the proposed Bubble to Slug transition decreases at higher mass fluxes, revealing the demand for further research and larger database in this parametric space.

2.8 Rivulets Flow

One "sub-regime" – which might also be responsible for the deterioration in the heat transfer coefficient at moderate and high vapor quality and the onset of local dryout – is the "Rivulets" flow regime.

Most of the Rivulets flow research has been motivated by the need to characterize heat and mass transfer for high flux heat exchangers. Among the more prominent studies are those by Barajas and Panton (1993), and Lee and Lee (2006, 2007, 2008).

Lee and Lee examined the influence of the surface wettability on the transition of the two-phase flow pattern in round mini-channels by testing three different cases: Highly wetting,

marginally wetting, and poorly wetting. The contact angle ranges for the three cases were: less than 50°, between 50° and 90°, and greater than 90°, respectively. Visual observations of the two-phase flow were used to create generalized, yet tentative, flow regime maps for each case.

The transition boundary to Rivulets flow, established by Lee and Lee, was added to Taitel-Dukler flow regime map, as shown in Figure 2.17.

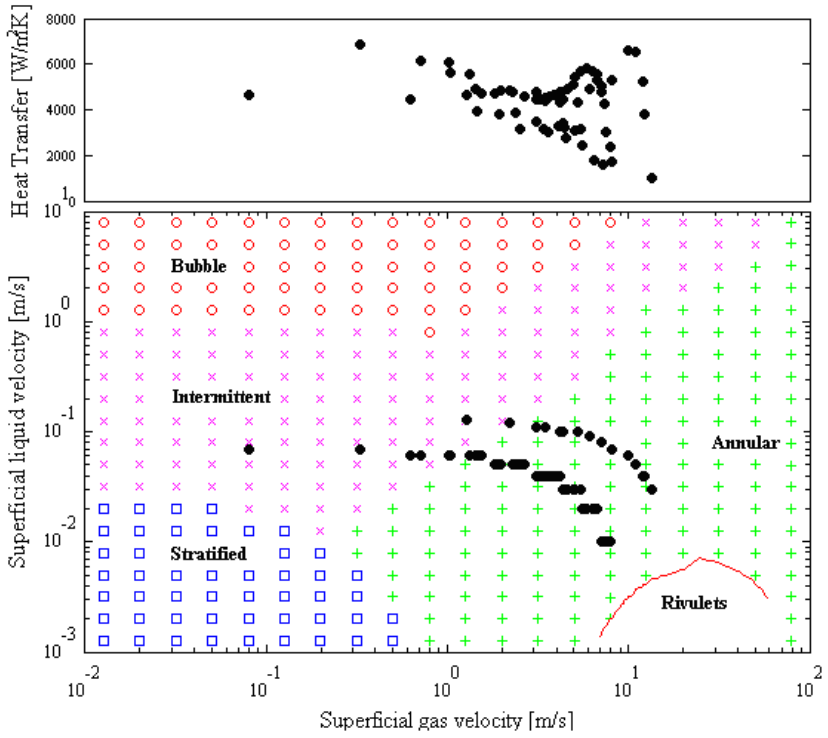

Figure 2.17 Taitel-Dukler map for Data of Yang and Fujita (2004), R113, G = 100 – 200 kg/m²s, q'' = 20 – 50 kW/m², P = 218 kPa

Though tentative, the comparison in Figure 2.17 shows that the deterioration of the heat transfer coefficient occurs in the vicinity of the transition from annular flow to rivulets flow.

2.9 Kabov et al Empirical Flow Regime Map for Short Channels

Kabov et al (2009) studied the flow of thin and ultrathin liquid films in microgap channels. A detailed experimental investigation, with local heating of a shear-driven film of water was performed and reported.

The test section was set horizontally, and the heater of 22 x 6.55 mm size was embedded into a copper block. The channel height was 1.5 mm and the film flow width varied from 65 to 120 mm. The experiments revealed the existence of three subregimes in the stratified flow – smooth, 2D waves, 3D waves.

It was found that a liquid film driven by the action of a gas flow in a channel is stable in a wide range of liquid/gas flow rates, Figure 2.18. For small liquid and gas flow rates the film surface is smooth. With increasing Re_L and Re_G, first, two dimensional waves form at the film surface (Kelvin-Helmholtz instability) and then they break into three dimensional ones. At relatively small Re_L and relatively high Re_G the film ruptures.

The above progression, along with the limit of Kelvin-Helmholtz instability can be seen in Figure 2.18.

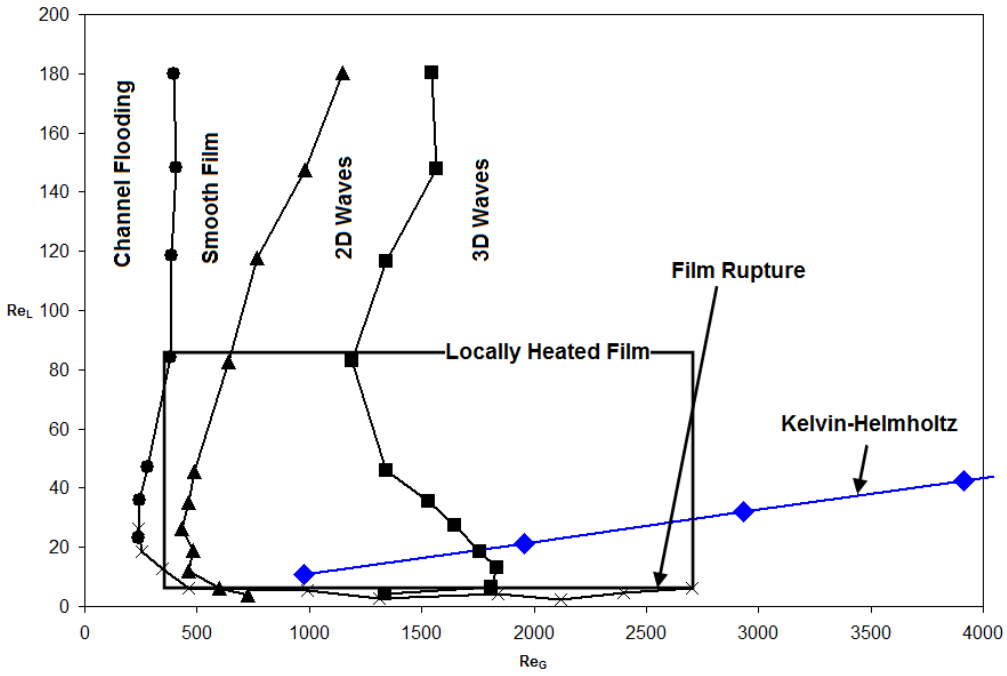

Figure 2.18 Flow regime map of Kabov et al (2009). Water flow, gap height is 1.5 mm, and gap width is 30 mm

Chapter 3

Two-Phase Heat Transfer in Microgap Coolers

In This chapter, the flow-regime-informed approach is applied to the analysis and evaluation of the two-phase heat transfer coefficients in miniature channels, the predictive accuracy of five classical two-phase heat transfer correlations, namely those due to Chen (1966), Kandlikar (2004), Gungor-Winterton (1985), Gungor-Winterton Revised (1986), and Shah (1977), was studied by comparing these predictions to the microgap two-phase flow heat transfer data collected from the open literature.

3.1 Microgap Channel Heat Transfer Coefficients

The paucity of currently available two-phase data for miniature channels and the large inherent parametric variations in the essential parameters, most notably in the heat transfer coefficient, as reflected in Figure 3.1, Lin et al (2001), suggest that the use of regime-linked correlations may achieve significant improvements in the predictability of two-phase flow parameters. Several recent studies of both conventional and small diameter tubes provide direct evidence of the link between flow regimes and key two-phase parameters and inspire confidence that regime-informed approaches can succeed in improving the predictive accuracy of two-phase formulations, beyond the current typical range of ±25% even in well studied geometries under common operating conditions.

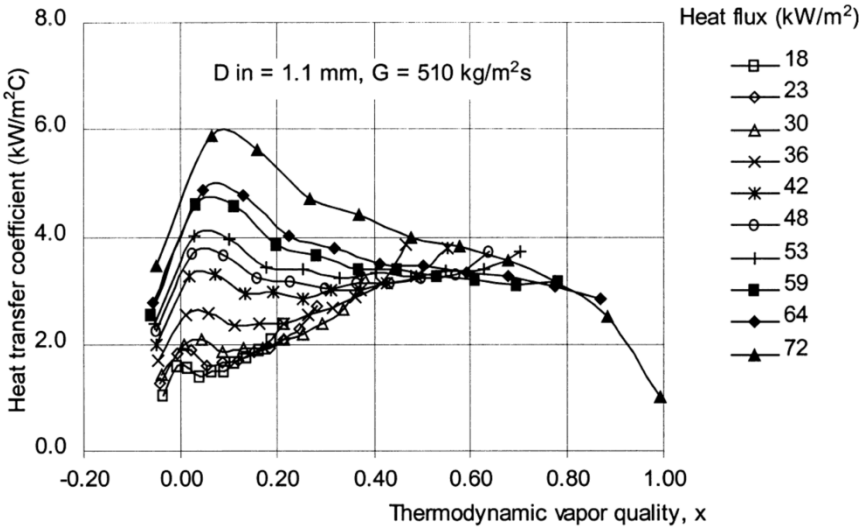

Figure 3.1 Typical heat transfer coefficient variations in two-phase flow through a tube, Lin et al (2001)

To evaluate the efficacy of using a flow-regime-informed approach to the prediction and correlation of two-phase microchannel and microgap cooler behavior, an extensive set of experimental studies of two-phase heat transfer and fluid mechanics behavior in miniature tubes and channels was identified and is listed in Table 3.1. The available data is seen to span a broad range of geometries, operating conditions, and working fluids. The hydraulic diameter ranges from 0.2 mm to 3.6 mm, with aspect ratios are as high as 100.

1612 data points were obtained from flows in single miniature, or loosely defined mini- and microgap.

Table 3.1 Microgap channels literature data

Author	Year	Fluid	Test Section	D_h [mm]	q'' [kW/m^2]	G [kg/m^{2}s]	Pressure [kPa]	Data Points	x
Lee & Lee	2001	R113	Single gap 2x20, 1x20, and 0.4x20	3.6, 1.9, 0.8	3-15	52-208	108-128	481	0.18-0.76
Yang & Fujita	2004	R113	Single gap 2x20, 1x20, 0.5x20, and 0.2x20	3.6, 1.9, 0.98, 0.4	20-90	100-200	101-219	292	0.01-0.96
Cortina-Diaz & Schmidt	2006	n-hexane, n-octane	Single vertical rectangular channel	0.59	11.6-148.3	100-400	101.3	724	Sub-cooled-0.8
Huh & Kim	2006	Water	Single rectangular channel	0.1	223-506	90-363	101-139	31	0.04-0.37
Sobierska et. al.	2006	Water	Single Vertical rectangular channel	0.48	35-196	200-1500	60-120	67	Sub-cooled-0.27
Kuzentsov & Shamirzaev	2006	R21	Single vertical Channel	2.552	6	215	194	17	0.04-0.98

3.2 Characteristic Heat Transfer Coefficient Variation

The inherent complexity of two-phase thermal transport and its parametric sensitivities in miniature channel flow can be expected to lead to substantial variations in the heat transfer coefficient as the vapor quality increases from near-zero (saturated liquid) to near-unity (saturated vapor) conditions. Examination of the data obtained in studies spanning the full range of qualities, as in Figure 3.2, not only confirms the anticipated variability of the heat transfer coefficient but also reveals the possible existence of a characteristic, M-shaped, heat transfer coefficient curve for

microchannel two-phase flow, with several phenomenological inflection points and segments of distinct and possibly opposite slope.

Referring to Figure 3.2, the experimental two-phase heat transfer coefficients obtained in the studies by Yang and Fujita (2004) and Cortina-Diaz and Schmidtt (2006), respectively, provide clear evidence of a possible M-shaped variation with thermodynamic quality. The empirical heat transfer coefficients are seen to rise steeply from the values attained for slightly subcooled conditions to a local maximum at a near-zero quality, after which the heat transfer coefficient values are seen to fall with higher quality towards a plateau-like region, only to reach another inflection point at moderate qualities (15%-40%), where the curve once again attains a positive slope. Beyond this point, the heat transfer coefficient rises with increasing quality until it reaches a second local peak, at elevated quality values, of approximately 50% and 75%, respectively, for the two data sets. For even higher vapor qualities, the heat transfer coefficient deteriorates until reaching the minimum reported values, at qualities approaching unity, generally associated with observed dryout conditions.

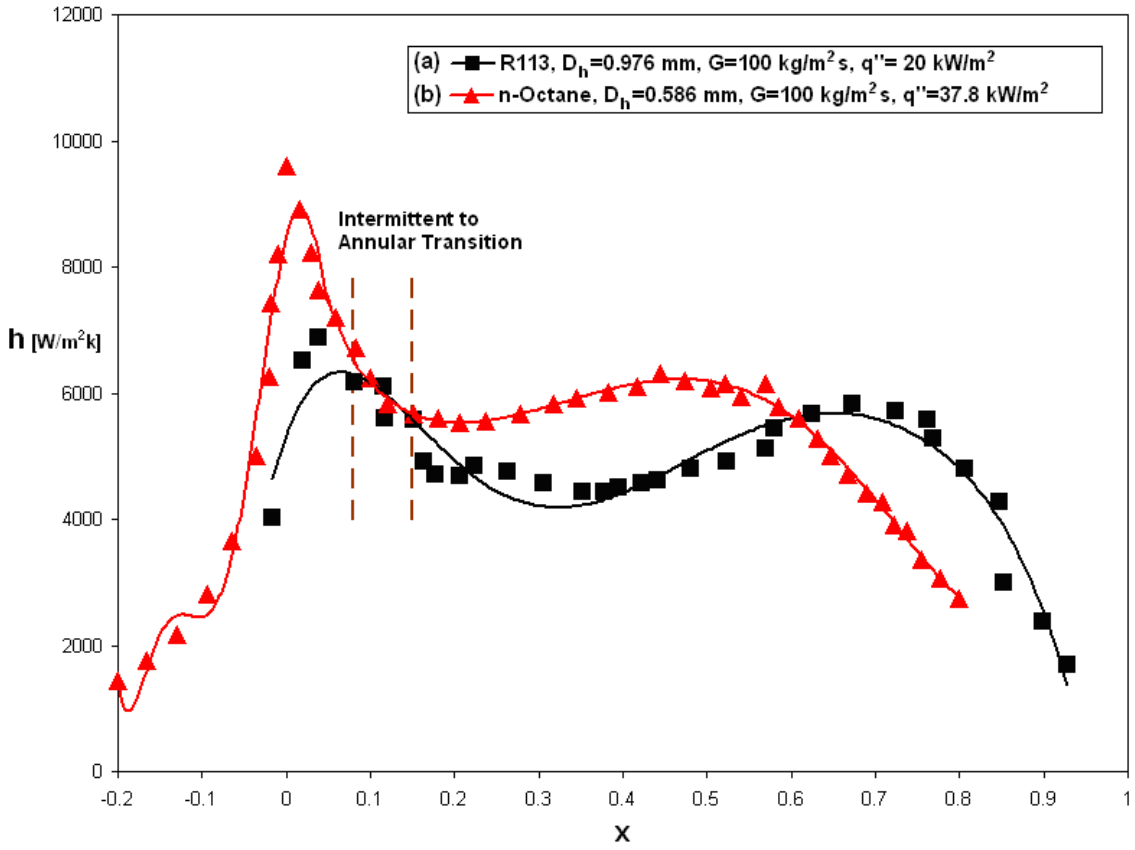

Figure 3.2 Characteristic heat transfer coefficient curve in microgap channel. (a) Yang and Fujita (2004), (b) Cortina-Diaz and Schmidt (2006)

The behavior captured in the characteristics M-curve for the two-phase heat transfer coefficient can be understood to reflect the underlying thermo-physics of two-phase phenomena in these miniature channels. The onset of nucleate boiling on the wall and the resulting acceleration of the bulk liquid velocity in Bubble flow, possibly occurring even in subcooled liquid, raises the heat transfer coefficients substantially above the single-phase forced convection values, giving rise to the first steep branch of the M-shaped curve. Bubble agglomeration limits any further increases in the heat transfer rates, followed by transition to Intermittent flow which leads to decreasing heat transfer coefficients, as trains of vapor slugs (separated by liquid plugs) induce alternating patches

of thin film evaporation and wall dryout. As the end of the Intermittent regime is approached the locus of the heat transfer coefficient flattens, but transition to Annular flow and the dominance of thin film evaporation, leads – once again – to rising heat transfer coefficients, due to thinning of the evaporating liquid film. Deep into the annular regime, but prior to the experimentally observed dryout limit, a decrease in the heat transfer coefficient occurs, apparently resulting from the local dryout of the liquid film.

Regrettably, it is rare to find in the literature data sets, of the type shown in Figure 3.2, that provide microchannel heat transfer coefficients over the full range of qualities. Rather, many of the examined data sets span only a modest range of qualities and, consequently, display only segments of the full M-shaped characteristic curve. This behavior is illustrated in Figure 3.3, which presents different sets of two-phase heat transfer experimental data by Yang and Fujita (2004), Lee and Lee (2001), Cortina-Diaz and Schmidt (2006), Sobierska et al. (2006), and Kuznetsov and Shamirzaev (2006).

A close examination of Figure 3.3 reveals that heat transfer coefficients of different data sets display similar behavior in the corresponding sections of the characteristic M-shape curve. For example, the locus of dataset “b” taken from the study by Lee and Lee in which the flow quality varied from 20% to 70%, displays a continuously rising heat transfer coefficient, as would be appropriate for the low-to-moderate quality Annular segment of the characteristic M-shaped heat transfer coefficient curve. Thus, when aggregated, these partial data sets appear to display and corroborate, albeit in somewhat less dramatic fashion, the existence of the M-shaped characteristic curve for the two-phase heat transfer coefficient.

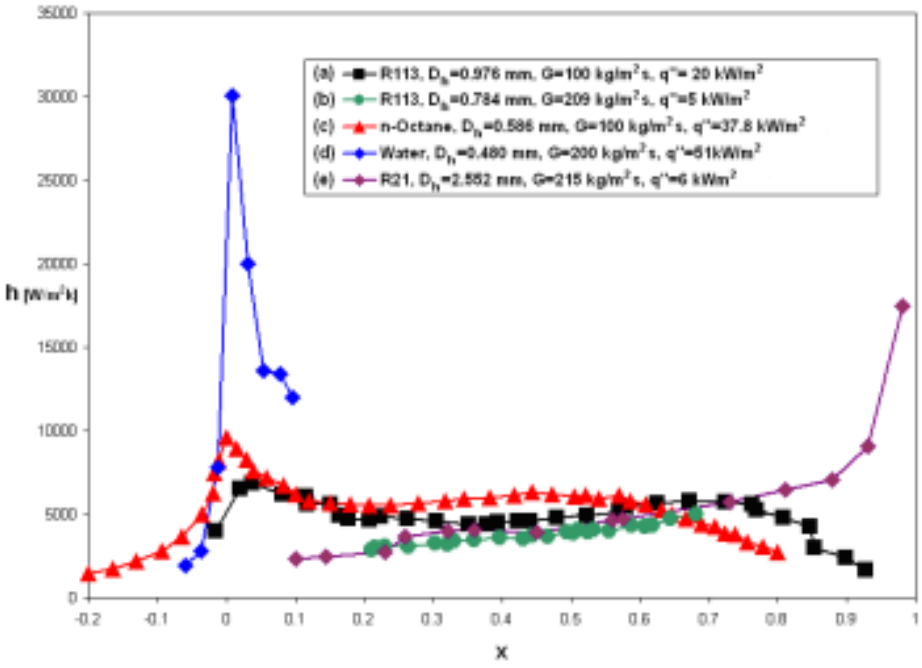

Figure 3.3 Heat transfer coefficient variation with vapor quality in single minigap channels

3.3 Flow Regime Maps Overlays

A more detailed examination of the heat transfer data, by overlaying the empirical values on the Taitel and Dukler flow regime maps, can provide additional insight into the observed inflection points and slope variation in the functional dependence of the heat transfer coefficient on superficial gas velocity (or vapor quality). Each of the data subsets shown in Figure 3.3 will now be overlaid on an appropriate Taitel-Dukler flow regime map to examine the affinity between the inflection points and the prevailing flow regimes.

Phase change heat transfer in single, parallel plate mini-gaps was investigated by Lee and Lee (2001) using R113 in a 300 mm long single horizontal rectangular gap. Hydraulic diameter

varied from 0.4 mm to 3.6 mm and seven thermocouples were used to measure wall temperature along the channel. For the 491 data points reported, Lee and Lee accounted for the variable saturation temperature along the channel using a model-predicted pressure variation along the channel. The total pressure drop was measured experimentally and reached up to 40 kPa. Annular flow was observed by Lee and Lee to dominate the hydrodynamic behavior of this channel, which agrees with the prediction of Taitel-Dukler flow regime methodology.

The operating loci for a R113 flowing in 0.4mm and 1 mm gaps, along with the measured heat transfer coefficient values, are shown in Figure 3.4.a and Figure 3.4.b and against the background of a flow regime map generated for this configuration. The operating loci are seen to fall well within the annular flow regime and the heat transfer coefficient is seen to rise continuously and reach local maxima of about 5000 W/m^{2}k and 3200 W/m^{2}k, respectively.

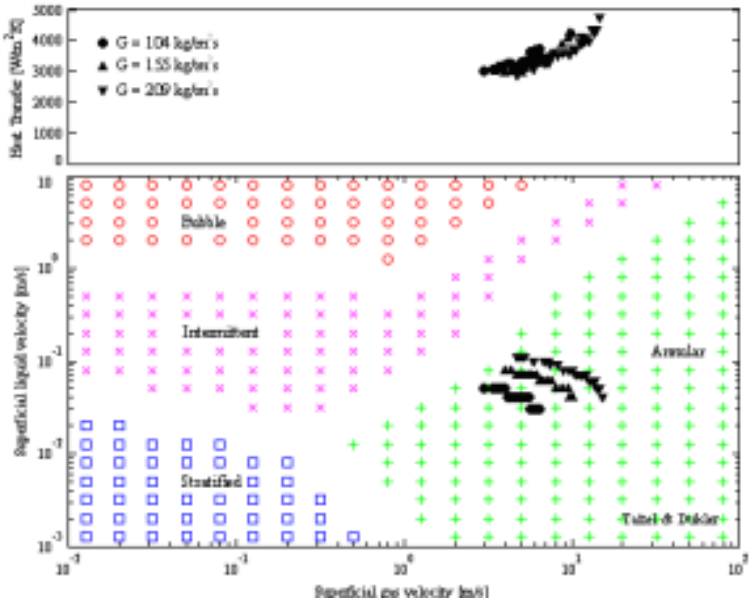

Figure 3.4.a Two-Phase flow parameters and heat transfer coefficients for R113 flowing in a miniature channel. Data of Lee and Lee (2001), 0.4 mm gap, q"= 5 kW/m^2, P=128 kPa

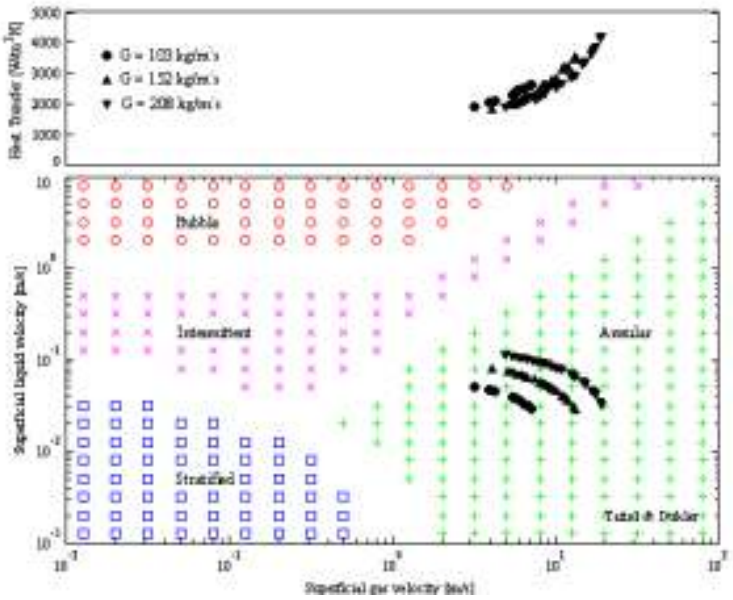

Figure 3.4.b Two-Phase flow parameters and heat transfer coefficients for R113 flowing in a miniature channel. Data of Lee and Lee (2001), 1 mm gap, q"= 10 kW/m^2, P=108 kPa

Yang and Fujita (2004) used R113 in a very similar experimental setup to that of Lee & Lee; 100 mm long single horizontal rectangular gap, with the width fixed at 20 mm while the height varied from 0.2 to 2 mm to yield hydraulic diameters from 0.4 to 3.6 mm. Five pairs of thermocouples were used to determine the wall temperature and the heat flux. In their database of 292 points, the mass flux varies from 50 to 200 kg/m^{2}s and the heat flux from 20 to 90 kW/m^2.

The flow regime map and heat transfer coefficient variation for all configurations in the Yang and Fujita mini-gap channel are displayed in the following figures. The authors observed Intermittent flow at the lower vapor quality and Annular flow occupying the region of vapor quality higher than 0.2 with a decided absence of Bubble flow. This observation agrees with the flow regime map generated for the average channel pressure, as previously discussed. While the

variation of the heat transfer coefficient with the superficial vapor velocity for the three larger channels displays the anticipated trends, the authors observed a different behavior for the smallest gap size of 200 micron, Figure 3.5, where the heat transfer coefficient reached a peak value at a low vapor quality and then failed to display the later inflection points. The deterioration in the heat transfer coefficient values might be due to non-uniformity in thin liquid film, and local dryout in the channel. The rest of Yang and Fujita data is shown in figure 3.6, Figure 3.7, and Figure 3.8, for gap sizes of 500 micron, 1 mm, and 2 mm, respectively. The larger diameter show more segments of the M-shape heat transfer coefficient curve.

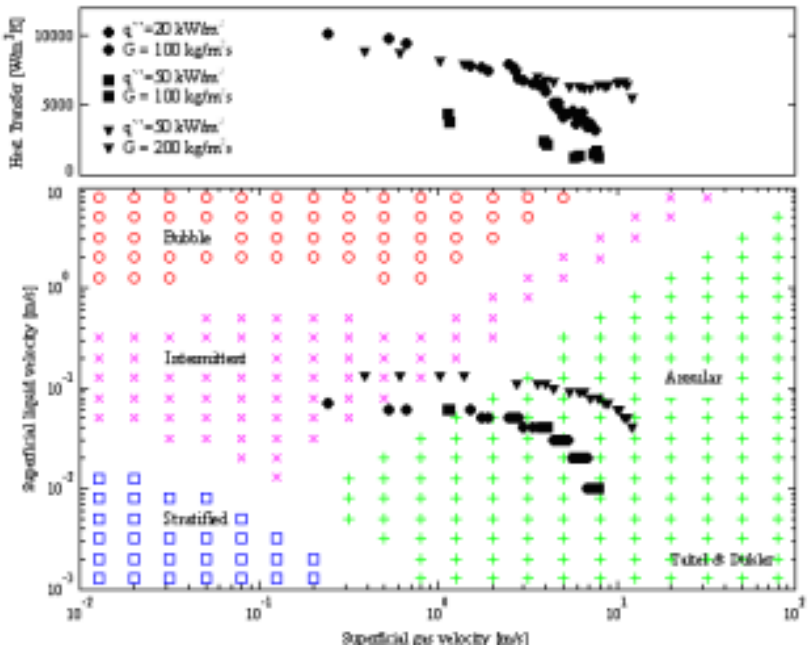

Figure 3.5 Two-Phase flow parameters and heat transfer coefficients for R113 flowing in a 0.2 mm microgap at 1.5 atmosphere pressure Yang and Fujita (2004)

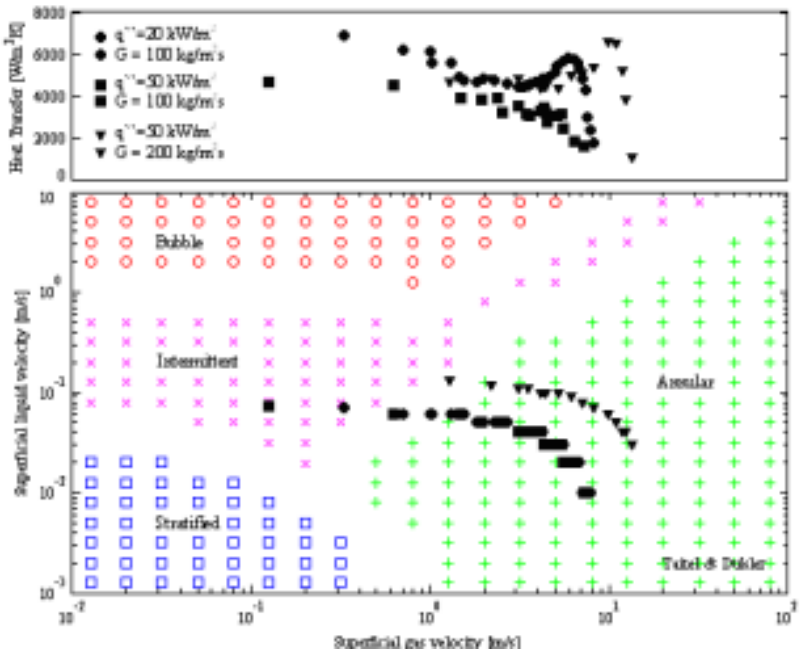

Figure 3.6 Two-Phase flow parameters and heat transfer coefficients for R113 flowing in a 0.5 mm microgap at 1.5 atmosphere pressure Yang and Fujita (2004)

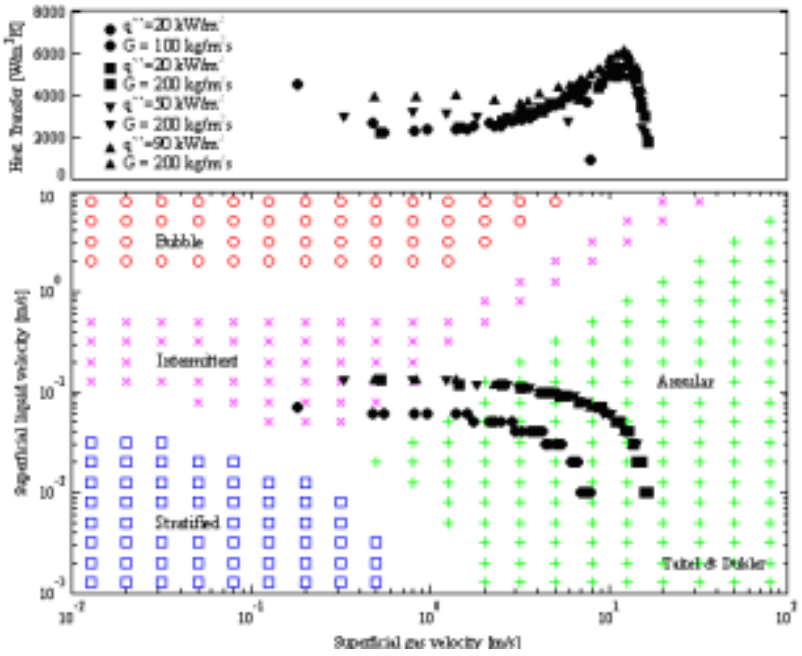

Figure 3.7 Two-Phase flow parameters and heat transfer coefficients for R113 flowing in a 1 mm microgap at 1.5 atmosphere pressure Yang and Fujita (2004)

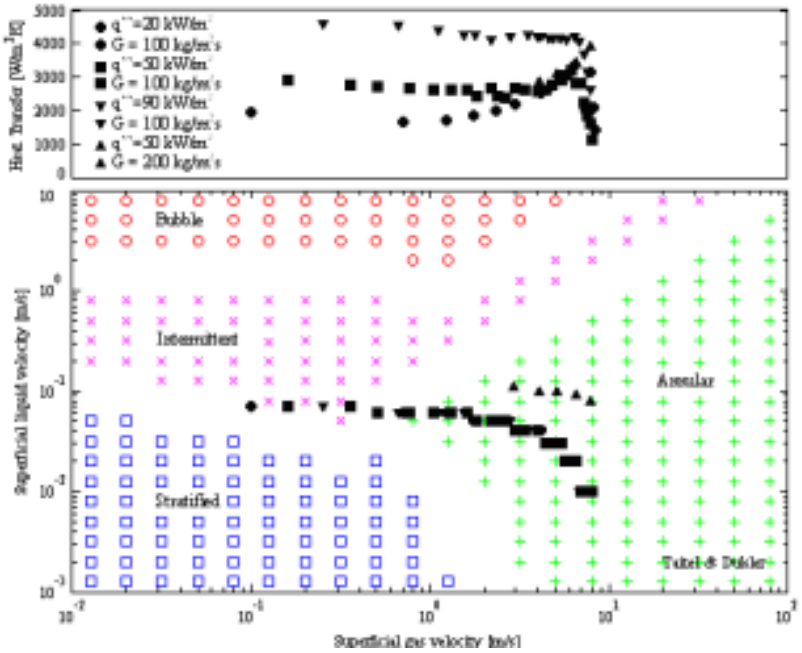

Figure 3.8 Two-Phase flow parameters and heat transfer coefficients for R113 flowing in a 2 mm microgap at 1.5 atmosphere pressure Yang and Fujita (2004)

Kuznetsov and Shamirzaev (2006) used R21 in a single vertical channel, 6.3 mm wide by 1.6 mm high, yielding a hydraulic diameter of 2.552 mm, and heated with a modest heat flux of 6 kW/m^2 or 0.6 W/cm^2. Four thermocouples were used along the channel length of 290 mm. The heat transfer coefficient was calculated based on the saturation temperature at each site, assuming that the pressure varied linearly between the inlet and outlet of the channel. As seen in Figure 3.9, following a slight decreasing trend in the Intermittent zone, after crossing the predicted transition to Annular flow at a quality of approximately 10%, the heat transfer coefficient was found to increase continuously with superficial gas velocity, with a steep increase after a quality of 50%, achieving a remarkable value of 18 kW/m^2K at a quality of 98%. This behavior and the authors' reference to thin film evaporation as the governing thermal transport mechanism are clearly

consistent with the expected heat transfer coefficient locus in the Intermittent and Annular flow regimes. It is noteworthy, however, that the highest heat transfer coefficients, which occurred at qualities above 90% and are associated with small wall excess temperature and low applied heat flux, can be expected to display relatively high uncertainties.

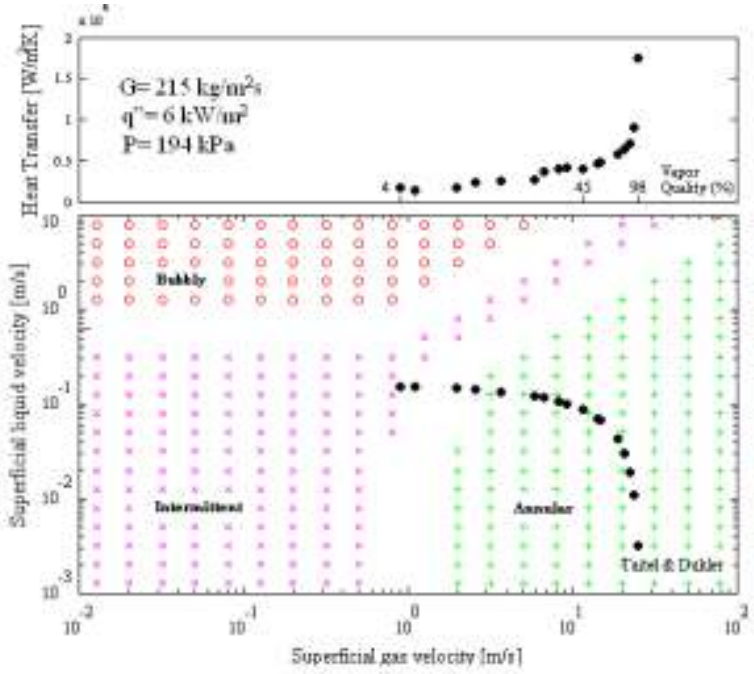

Figure 3.9 Two-Phase flow parameters and heat transfer coefficients for R21 flowing at 194 kPa in a single miniature channel with 1.6 mm gap, (D_h= 2.552 mm).

3.4. Classical Heat Transfer Correlations

In this section, the classical two-phase heat transfer correlations are presented, with emphasis on the Chen (1966) correlation which was based mainly on Annular flow regime.

3.4.1 Chen Heat Transfer Correlation for Annular Flow

One of the earliest and most successful correlations for heat transfer in two-phase flow was proposed by Chen (1966). The correlation was based on an Annular flow regime and viewed the two-phase heat transfer coefficient at the heated wall as a summation of the "micro" contribution - reflecting nucleate boiling, and the "macro" contribution – reflecting forced convection. The starting point for the Chen correlation is:

$$h = h_{mic} + h_{mac} \tag{3.1}$$

The macroscopic contribution was calculated using the modified correlation proposed by Bennett and Chen (1980) with a Prandtl number correction factor to generalize the correlation beyond water as the working fluid, i.e.

$$h_{mac} = h_l F\left(X_{tt}\right) \mathrm{Pr}_l^{0.296} \tag{3.2}$$

The enhancement factor, F, was meant to represent the shear-induced acceleration of flow along the wall, due to relatively high vapor velocity in the core of the channel. The single phase, liquid only, convective coefficient (h_l) is calculated via the Dittus-Boelter (1930) equation:

$$h_l = 0.023 \left(\frac{k_l}{D} \right) \mathrm{Re}_l^{0.8} \mathrm{Pr}_l^{0.4} \tag{3.3}$$

Where:

$$\mathrm{Re}_l = \frac{G(1-x)D}{\mu_l} \tag{3.4}$$

The microscopic contribution was calculated using the Forster-Zuber (1955) correlation for pool boiling with an additional correction factor in the form of a suppression factor:

$$h_{mic} = 0.00122 \cdot \left[\frac{k_l^{0.79} c_{pl}^{0.45} \rho_l^{0.49}}{\sigma^{0.5} \mu_l^{0.29} h_{lv}^{0.24} \rho_v^{0.24}} \right] \cdot \left[T_w - T_{sat}(P_l) \right]^{0.24} \cdot \left[P_{sat}(T_w) - P_l \right]^{0.75} \cdot S \tag{3.5}$$

The suppression factor, S is required to account for the fact that nucleation is suppressed when the macroscopic convective effect increases in strength, leading to a reduced wall superheat. To calculate this suppression factor, Chen used a regression analysis of the data to fit S as a function of a two phase Reynolds number defined as:

$$\mathrm{Re}_{tp} = \mathrm{Re}_l \left[F(X_{tt}) \right]^{1.25} \tag{3.6}$$

Chen originally presented the suppression data in graphical format. However, Collier (1981) found the following empirical fit for the suppression factor (which is used in this study):

$$S(\mathrm{Re}_{tp}) = \left(1.25 + 2.56\, x 10^{-6}\, \mathrm{Re}_{tp}^{1.17} \right)^{-1} \tag{3.7}$$

Collier, also, provided empirical fits for the "macro" enhancement factor, F(Xtt), in the form:

$$F(X_{tt}) = 1 \qquad \text{for } X_{tt}^{-1} \le 0.1 \tag{3.8}$$

$$F(X_{tt}) = 2.35 \left(0.213 + \frac{1}{X_{tt}} \right)^{0.736} \qquad \text{for } X_{tt}^{-1} > 0.1 \tag{3.9}$$

The Martinelli parameter X_{tt} is calculated as:

$$X_{tt} = \left(\frac{1-x}{x}\right)^{0.9}\left(\frac{\rho_g}{\rho_l}\right)^{0.5}\left(\frac{\mu_l}{\mu_g}\right)^{0.1} \tag{3.10}$$

Figure 3.10 displays the variation of the Chen-derived heat transfer coefficient for two-phase flow in a channel of 500 micron diameter, with a mass flux of 500 kg/m^{2}s along with the variation of the convective and boiling heat transfer coefficients; h_{mic} and h_{mac}.

Interestingly, for much of the quality range, the strong shear-induced enhancement, embodied in the F factor, overcomes the decrease in the liquid-only heat transfer coefficient, h_l, associated with the drop in the two-phase Reynolds number, to yield a steeply rising "macroscopic," and hence total two-phase, heat transfer coefficient. However, at the highest qualities – commencing around 85% for the conditions of Figure 3.10 – the enhancement is no longer sufficient to drive increases in h_{mac} and the two-phase heat transfer coefficient begins to drop significantly. Thus, while the physics underpinning the Chen correlation does not anticipate the effects of local dryout on h, the data used to correlate the F factor apparently does capture that effect and the Chen correlation is- thus - qualitatively in agreement with the Annular heat transfer coefficient data for miniature channels.

The microscopic contribution in the form of the boiling heat transfer coefficient, h_{mic}, is plotted in Figure 3.10, against vapor quality for an assumed wall superheat of 8 K in a 0.5 mm diameter channel operating at a 500 kg/m^{2}s mass flux. Figure 3.10 reveals that the microscopic contribution, under these typical two-phase conditions, is far lower than the macroscopic heat transfer coefficient and diminishes further under the influence of the suppression factor, as the

quality increases. It is, consequently, apparent that the macroscopic contribution, h_{mac}, is dominant in miniature channels and that the nucleate boiling term, i.e. the microscopic contribution, h_{mic}, can be neglected in determining the two-phase heat transfer rate in a miniature channel.

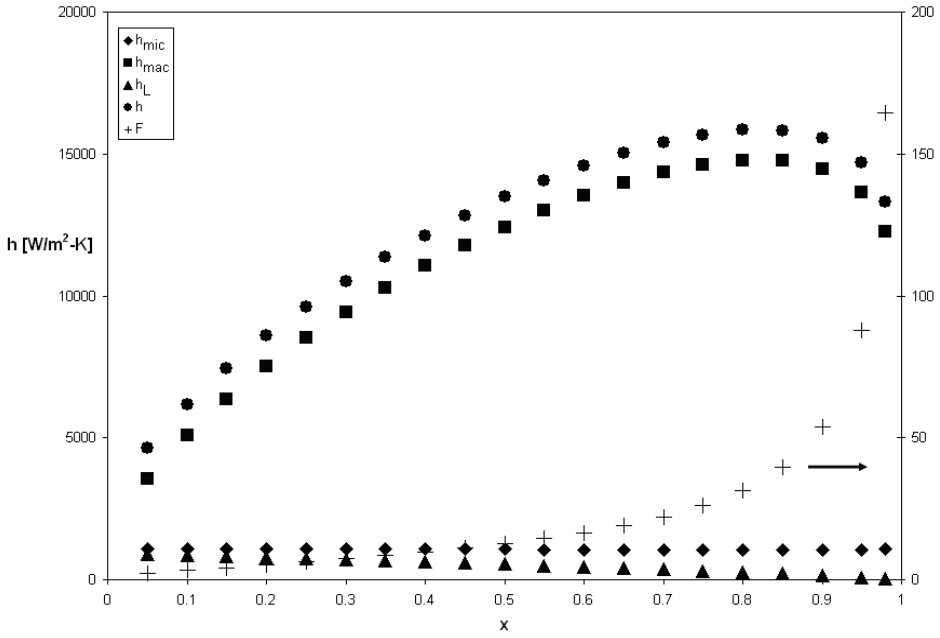

Figure 3.10 Single- and two-phase heat transfer coefficient predicted by Chen correlation for D = 500 micron, G = 500 kg/m^{2}s, $T_{wall,Superheat}$ = 8 K

3.4.1.1 Diameter Effect on Heat Transfer Coefficients in Microgap Channels

In the analysis of microgap refrigerant data, it was found that the classic Chen correlation, Chen, (1966) gave the best agreement with the data that was associated with annular flow, yielding an MAE of just 24% for the heat transfer coefficients falling on the up-sloping branch of the M-

shaped locus. Attention was then turned to exploring the parametric dependence of annular flow heat transfer in microgaps, as reflected in the Chen correlation.

The behavior of the annular flow heat transfer coefficient, predicted by the Chen correlation, is examined, with particular emphasis on the effect of diameter.

In Figure 3.11, the two-phase, annular flow heat transfer coefficient predictions are shown for R113 flowing in tube diameters ranging from 100 micron to 1 cm and experiencing an increase in thermodynamic quality from 0.15 to 1.0, reflecting an evaporating flow. For purposes of this figure, the mass flux was held constant at a typical value of 500 kg/m^2s. It can be seen the heat transfer coefficient variation with quality is quite sensitive to diameter, increasing far more steeply and reaching a significantly higher value for the small 0.1 mm diameter than for the large 1 cm diameter tube. More specifically, the maximum heat transfer coefficient is seen to increase from 8 kW/m^2K to 20 kW/m^2K when the diameter decreases from 1 cm to 100 micron, reflecting the anticipated beneficial effects of progressively thinner liquid films and higher shear forces as the tube diameter decreases. Interestingly, all 4 tube diameters display a peak heat transfer coefficient at a quality of approximately 0.85 and then a significant drop off as the quality trends towards unity.

The single-phase (all-vapor) heat transfer coefficients at a quality of unity ($x = 1$) are shown for comparison in Figure 3.11 and, at approximately 500 W/m^2K to 1000 W/m^2K for the 4 diameters considered, are far below the two-phase values discussed. Inspection of Figure 3.11 does, however, suggest that these all-vapor values could provide an asymptote for the two-phase heat transfer coefficient as full dryout conditions are approached.

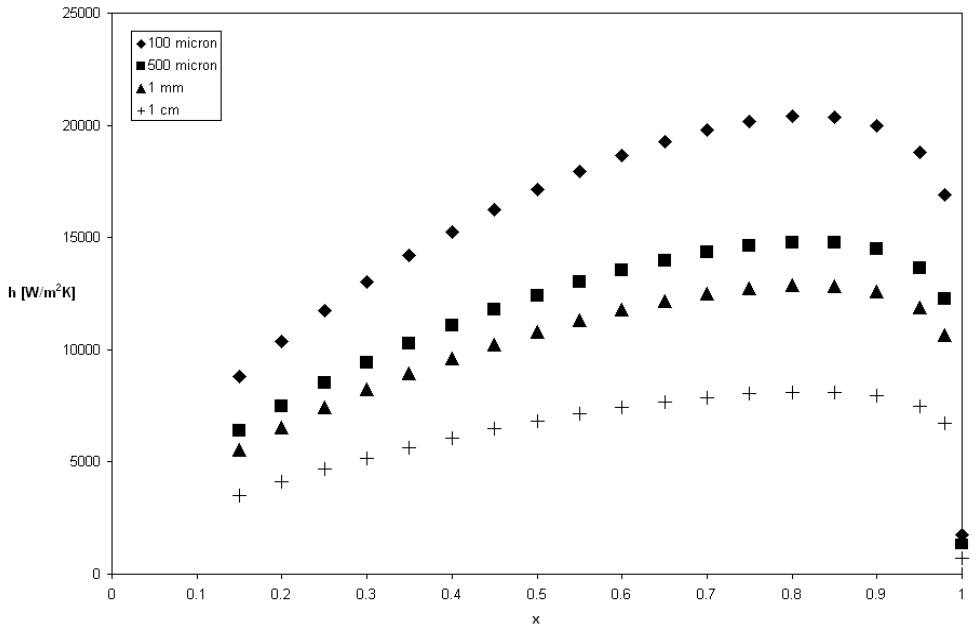

Figure 3.11 Dependency of heat transfer coefficient on the channel diameter, R113, G = 500 kg/m^{2}s

3.4.1.2 Mass Flux Effect

The effect of mass flux on the R113 annular flow heat transfer coefficient is shown in Figure 3.12, for values ranging from 100 kg/m^{2}s to 1000 kg/m^{2}s, an assumed tube diameter of 0.5 mm, and for a range of qualities from 0.15 to 1.0. Based on

$$h_l = 0.023\left(\frac{k_l}{D}\right)\mathrm{Re}_l^{0.8}\,\mathrm{Pr}_l^{0.4} \tag{3.11}$$

$$\mathrm{Re}_l = \frac{G(1-x)D}{\mu_l} \tag{3.12}$$

It may be expected that the higher mass fluxes will lead to larger values of the two-phase Reynolds Number and, hence, higher liquid-only heat transfer coefficients. When multiplied by the enhancement factor, F, which is only dependent on fluid properties and the quality, higher values of h_l result in higher predicted values of the macroscale heat transfer coefficient. Thus, Figure 3.12 reveals a strong dependence of the two-phase heat transfer coefficient on mass flux, at every value of x. For the highest value of G, at 1000 kg/m^{2}s, the heat transfer coefficient is seen to increase steeply up to a quality of 0.85, peaking at over 25 kW/m^{2}K before declining to approximately 17 kW/m^{2}K at a quality of 0.98. The peak two-phase heat transfer coefficients appear to reach 14 kW/m^{2}K and 3 kW/m^{2}K, for the 500 kg/m^{2}s and 100 kg/m^{2}s mass fluxes, respectively. Interestingly, at the lowest value of G, the heat transfer coefficient is found to be relatively insensitive to the thermodynamic quality.

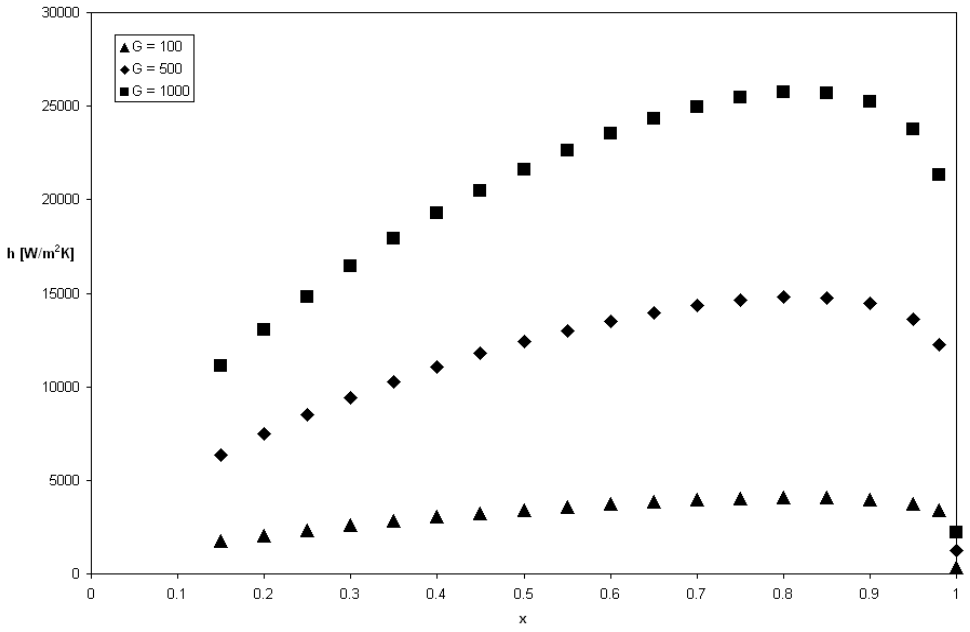

Figure 3.12 Parametric dependency of heat transfer coefficient on the mass flux. R113, D = 500 micron

3.4.1.3 Fluid Property Effect

Figure 3.13 shows a comparison of the two-phase heat transfer coefficients for two common refrigerants, R134a and R113, and two dielectric liquids, FC72 and HFE7100, commonly used in electronic cooling applications. The calculated values are for a 500 micron diameter channel operating at a mass flux of 500 kg/m^{2}s, over the range of qualities, 0.1 to 0.98 where annular flow is expected to prevail. Refrigerant 134a, with its superior thermal properties, is found to provide relatively high heat transfer coefficients for this full range, peaking at an h of 24 kW/m^{2}K at a quality of 0.85 and offering heat transfer coefficients above 20 kW/m^{2}K for all x values above 0.5, except for the dryout asymptote at an x value of unity.

Interestingly, HFE7100 – a relatively new electronic cooling fluid – appears to provide significantly higher two-phase heat transfer coefficients than the more common FC-72, peaking at 16.5 kW/m^{2}K vs. the 12.5 kW/m^{2}K for FC-72, under the same operating conditions. It must, nevertheless, be noted that, due to some uncertainty in the relevant properties of HFE7100, particularly the latent heat of vaporization and liquid thermal conductivity, some caution must be taken in applying this result.

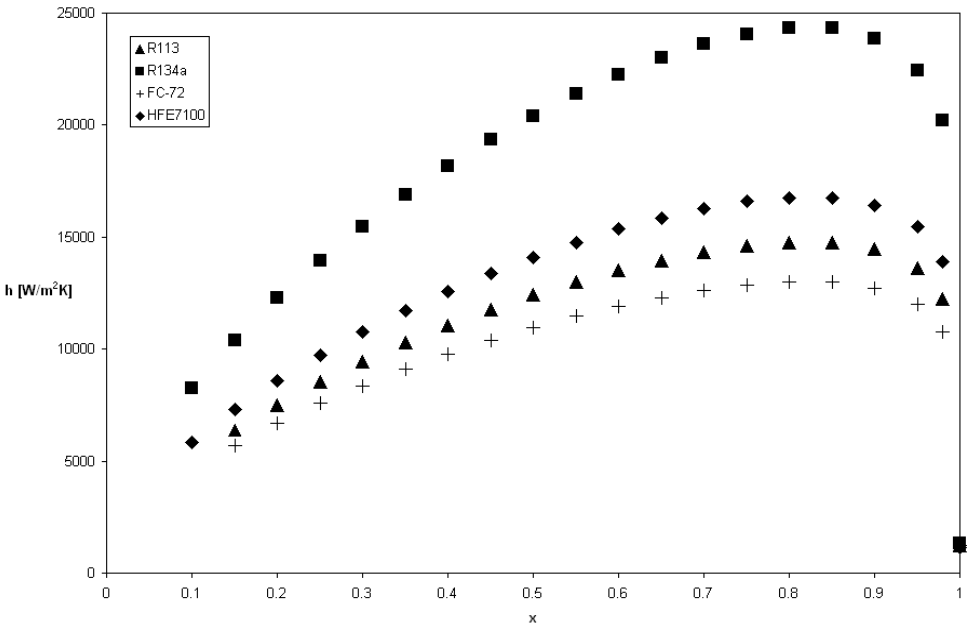

Figure 3.13 Parametric dependency of heat transfer coefficient on Fluid properties in D = 500 micron, G = 500 kg/m^{2}s

3.4.2 Shah Heat Transfer Correlation

For Shah (1976) Correlation the heat transfer coefficient takes the form

$$\psi_s = \frac{h_{\text{tp}}}{h_{\text{l}}} = f\left(\text{Co}, \text{Bo}, \text{Fr}_{le}\right) \tag{3.13}$$

with the relevant dimensionless parameters provided as

$$\text{Co} = \left(\frac{1-x}{x}\right)^{0.8}\left(\frac{\rho_{\text{g}}}{\rho_{\text{l}}}\right)^{0.5} \tag{3.14}$$

$$\text{Bo} = \frac{q^{"}}{GC_{\text{lg}}} \tag{3.15}$$

$$\mathrm{Fr}_{le} = \frac{G^2}{\rho_1^2 g D} \tag{3.16}$$

The original Shah correlation was presented in graphical form. In 1982 Shah provided a computational representation of his correlation. This computational representation was outlined as

$$N_s = \mathrm{Co} \text{ for } \mathrm{Fr}_{le} \geq 0.04 \tag{3.17}$$

$$N_s = 0.038\,\mathrm{Fr}_{le}^{-0.3}\mathrm{Co} \text{ for } \mathrm{Fr}_{le} < 0.04 \tag{3.18}$$

$$F_s = 14.7 \text{ for Bo } \geq 11\text{E-4} \tag{3.19}$$

$$F_s = 15.4 \text{ for Bo } < 11\text{E-4} \tag{3.20}$$

$$\psi_{cb} = 1.8 N_s^{-0.8} \tag{3.21}$$

For $N_s > 1$:

$$\psi_{nb} = 230\,\mathrm{Bo}^{0.5} \text{ for Bo } > \text{ 0.3E-4} \tag{3.22}$$

$$\psi_{nb} = 1 + 46\,\mathrm{Bo}^{0.5} \text{ for Bo } \leq \text{ 0.3E-4} \tag{3.23}$$

$$\psi_s = \max\left(\psi_{cb}, \psi_{nb}\right) \text{for } N_s \leq 1 \tag{3.24}$$

For $0.1 < N_s \leq 1$

$$\psi_{bs} = F_s \mathrm{Bo}^{0.5} \exp\left(2.74 \mathrm{N}_{\mathrm{s}}^{-0.1}\right) \tag{3.25}$$

$$\psi_s = \max\left(\psi_{cb}, \psi_{bs}\right) \tag{3.26}$$

For $N_s \leq 0.1$

$$\psi_{bs} = F_s \mathrm{Bo}^{0.5} \exp\left(2.47 \mathrm{N}_{\mathrm{s}}^{-0.15}\right) \tag{3.27}$$

$$\psi_s = \max\left(\psi_{cb}, \psi_{bs}\right) \tag{3.28}$$

This computational representation is used in this work.

3.4.3 Kandlikar Heat Transfer Correlation

This correlation was published in Kandlikar and Balasubramanian (2004), and can be summarized as:

A. Turbulent Region: $Re_{LO} \geq 3000$

$$h_{TP,NBD} = 0.6683\,CO^{-0.2}(1-x)^{0.8} f_2(Fr_{LO})\, h_{LO} + 1058\,Bo^{0.7}(1-x)^{0.8} F_{Fl}\, h_{LO} \tag{3.29}$$

$$h_{TP,CBD} = 1.136\,CO^{-0.9}(1-x)^{0.8} f_2(Fr_{LO})\, h_{LO} + 667.2\,Bo^{0.7}(1-x)^{0.8} F_{Fl}\, h_{LO} \tag{3.30}$$

Where:

$$f_2(Fr_{LO}) = (25\,Fr_{LO})^{0.3} \quad if\ \ horizontal\ \ and\ \ Fr_L \leq 0.04 \tag{3.31}$$

$$f_2(Fr_{LO}) = 1 \qquad if\ \ vertical\ \ or\ \ Fr_L > 0.04 \tag{3.32}$$

$$h_{LO} = \frac{\mathrm{Re}_{LO}\,\mathrm{Pr}_L (f/2)(K_L/D)}{1 + 12.7(\mathrm{Pr}_L^{2/3} - 1)(f/2)^{0.5}} \quad for\ \ 10^4 \leq \mathrm{Re} \leq 5\times 10^6 \tag{3.33}$$

$$h_{LO} = \frac{(\mathrm{Re}_{LO} - 1000)\,\mathrm{Pr}_L (f/2)(K_L/D)}{1 + 12.7(\mathrm{Pr}_L^{2/3} - 1)(f/2)^{0.5}} \quad for\ \ 3000 \leq \mathrm{Re} \leq 10^4 \tag{3.34}$$

$$f = [1.58\ln(\mathrm{Re}_{LO}) - 3.28]^{-2} \tag{3.35}$$

The two phase heat transfer coefficient is the greater of $h_{TP,NBD}$ and $h_{TP,CBD}$.

B. Transitional Flow Region: $1600 \leq Re_{LO} \leq 3000$

$$h_{TP,NBD} = 0.6683\,CO^{-0.2}(1-x)^{0.8}\, h_{LO} + 1058\,Bo^{0.7}(1-x)^{0.8} F_{Fl}\, h_{LO} \tag{3.36}$$

$$h_{TP,CBD} = 1.136 CO^{-0.9}(1-x)^{0.8}\, h_{LO} + 667.2\,Bo^{0.7}(1-x)^{0.8} F_{Fl}\, h_{LO} \tag{3.37}$$

With h_{LO} taken from linear interpolation between the turbulent value using Gnielinski (1976) equation and the laminar value using

$$h_{LO} = (Nu^*K/D_h) \tag{3.38}$$

The two phase heat transfer coefficient is the greater of $h_{TP,NBD}$ and $h_{TP,CBD}$.

C. Laminar Flow Region: $Re_{LO} \leq 1600$

$$h_{TP,NBD} = 0.6683\,CO^{-0.2}(1-x)^{0.8}\,h_{LO} + 1058\,Bo^{0.7}(1-x)^{0.8}\,F_{Fl}\,h_{LO} \quad (3.39)$$

$$h_{TP,CBD} = 1.136\,CO^{-0.9}(1-x)^{0.8}\,h_{LO} + 667.2\,Bo^{0.7}(1-x)^{0.8}\,F_{Fl}\,h_{LO} \quad (3.40)$$

$h_{LO} = (Nu*K/D_h)$

The two phase heat transfer coefficient is the greater of $h_{TP,NBD}$ and $h_{TP,CBD}$.

D. Low Reynolds Number Flow in Minichannels: $100 \leq Re_{LO} \leq 410$

$$h_{TP,NBD} = 0.6683\,CO^{-0.2}(1-x)^{0.8}\,h_{LO} + 1058\,Bo^{0.7}(1-x)^{0.8}\,F_{Fl}\,h_{LO} \quad (3.41)$$

$$h_{TP,CBD} = 1.136\,CO^{-0.9}(1-x)^{0.8}\,h_{LO} + 667.2\,Bo^{0.7}(1-x)^{0.8}\,F_{Fl}\,h_{LO} \quad (3.42)$$

$h_{LO} = (Nu*K/D_h)$ (3.43)

The two phase heat transfer coefficient is the greater of $h_{TP,NBD}$ and $h_{TP,CBD}$.

E. Very Low Reynolds Number in Microchannels: $Re_{LO} \leq 100$

$$h_{TP,NBD} = 0.6683\,CO^{-0.2}(1-x)^{0.8}\,h_{LO} + 1058\,Bo^{0.7}(1-x)^{0.8}\,F_{Fl}\,h_{LO} \quad (3.44)$$

Where: $h_{LO} = (Nu*K/D_h)$ (3.45)

In this region, The two phase heat transfer coefficient is equal to $h_{TP,NBD}$

3.4.4 Gungor-Winterton Heat Transfer Correlation

Gungor and Winterton (1986) heat transfer correlation has the following form:

$$h = E\,h_l + S\,h_{nb} \tag{3.46}$$

h_l is the liquid single phase heat transfer coefficient and found using Dittus-Boelter (1930) equation . The factor E is termed the enhancement factor and is given via:

$$E = 1 + 24000\ Bo^{1.16} + 1.37\left(\frac{1}{\chi_{\text{tt}}}\right)^{0.86} \tag{3.47}$$

$$S = \left(1 + 0.00000115\,E^2\,\text{Re}_l^{1.17}\right)^{-1} \tag{3.48}$$

And the nucleate boiling heat transfer coefficient is calculated using the Cooper correlation:

$$h_{nb} = 55\text{Pr}^{\,0.12}\left(-\log_{10} p_r\right)^{-0.55}\text{M}^{-0.5}\text{q}''^{0.67} \tag{3.49}$$

3.4.5 Gungor-Winterton Revised Heat Transfer Correlation

This simpler form of the Gungor-Winterton correlation was published by Gungor and Winterton (1987), and is given by:

$$h = h_l\left[1 + 3000\,Bo^{0.86} + \left(\frac{x}{1-x}\right)^{0.75}\left(\frac{\rho_l}{\rho_v}\right)^{0.41}\right] \tag{3.50}$$

3.5 Heat Transfer Correlations Predictions – Comparison to Literature Data

In this analysis, the local channel pressure (for determination of fluid properties and gas velocities) was evaluated by the method described in each of the selected studies, which frequently involved an assumed linear variation from the inlet to the outlet of the channel. The hydraulic diameter for the two-phase heat transfer comparison purposes was defined as:

$$d_h = \frac{4\times(Channel\ \ Cros\,\mathrm{sec}\,tional\ \ Area)}{Heated\ \ Perimeter} \tag{3.51}$$

Where the heated perimeter in microgaps was taken as only one side of the miniature channel. Applying the procedure mentioned above, a statistical analysis was performed to determine the discrepancy between the values predicted by each of the aforementioned classical two-phase heat transfer correlations and the miniature channel heat transfer data in the selected studies listed in Table 3.1. The relative discrepancy in the prediction of the heat transfer coefficients was calculated as:

$$\varepsilon_i = \frac{\left|h_{predicted} - h_{measured}\right|}{h_{measured}} \tag{3.52}$$

The average relative discrepancy for a set of data was calculated as

$$\varepsilon_{average} = \frac{1}{n}\sum_{i}^{n}\varepsilon_i \tag{3.53}$$

The standard deviation of the data from the values predicted by each correlation was here defined as:

$$\sigma = \frac{1}{n}\sqrt{\sum_{i=1}^{n} \varepsilon_i^2} \tag{3.54}$$

Table 3.2 provides a summary of the calculated discrepancy between the selected correlations and the examined dataset of 790 microgap refrigerant data points.

Table 3.2 Predictive cccuracy of classical two-phase correlations for refrigerants flowing in single miniature channels

Regime		Intermittent	Annular-Low Quality	Annular-Moderate Quality	Total
Number of Data Points		44	687	59	790
Chen	ε_{AVE}	72%	24%	39%	28%
	σ	75%	31%	64%	38%
Kandlikar	ε_{AVE}	36%	57%	48%	55%
	σ	44%	62%	52%	61%
Gungor-Winterton	ε_{AVE}	72%	36%	54%	39%
	σ	85%	58%	92%	63%
Gungor-Winterton Revised	ε_{AVE}	34%	33%	37%	34%
	σ	42%	40%	52%	41%
Shah	ε_{AVE}	32%	32%	40%	39%
	σ	40%	39%	59%	41%

As may be seen in Table 3.2, for single channel refrigerant flow, surprisingly good predictive accuracy for two-phase flow is provided by 3 of the 5 correlations, namely that due to Chen, Gungor-Winteron (revised), and Shah. In particular, the best-fitting Chen correlation, shows an average discrepancy of 28% and a standard deviation of 38% with the data in this category, meaning that nearly 70% of the 790 data points fall within 38% of the Chen predictions. For

Gungor-Winteron and Shah, this spread rises to an average discrepancy of 34% and 39%, respectively, and an identical standard deviation of 41%.

Large discrepancies are seen, as well, between these correlations and the heat transfer coefficient values for refrigerants and dielectric liquids flowing in multiple microchannel configurations. These classical correlations provide standard deviations from the data that range from 100% to 200%, and no better than the average discrepancy of 52% (along with the standard deviation of 101%) achieved by the Kandlikar correlation. It may well be that these large variations are due primarily to the nonuniform flow distribution and two-phase flow instabilities often observed, but frequently left unreported, in microchannel coolers with multiple channel configurations, as noted by Bergles and Kandlikar (2005). Similarly poor agreement is seen for the classical correlations applied to the multiple microchannel water data, with the Kandlikar correlation again offering the best agreement, though with an average discrepancy of 67% and a standard deviation of 94% relative to this data.

Reflecting the observed value of a flow-regime-informed approach to the interpretation of two-phase heat transfer parameters, further comparison was conducted by dividing the available data into three categories: Intermittent Flow, Annular Flow-low quality, and Annular Flow–moderate quality, as was shown in Table 3.2 The peak heat transfer coefficient reported for each set of conditions was used as the criteria for separating the “low quality” and “moderate quality” sub-regimes of annular flow. When viewed in this “classified” form, significant differences emerge in the predictive accuracy of the classical correlations. Thus, the Chen correlation, with an overall standard deviation of 38%, shows significantly better agreement with the Annular-low

quality data, with a standard deviation of 31%, than it does with data in the Intermittent (σ=75%) and Annular-moderate quality (σ=64%) categories. Similarly, the Kandlikar correlation, with an overall standard deviation of 61%, agrees far better with the Intermittent data (σ=44%) than with the Annular-low quality data (σ =62%) and the Annular-moderate quality data (σ =52%). Interestingly, the standard deviations of the Gungor-Winterton (revised) and the Shah correlations, respectively, display less profound variations with the classification category, both providing a standard deviation of approximately 40% for data in the Intermittent and Annular-low quality categories and standard deviations with Annular-moderate quality data that fall in the 52%-59% range .

In the dominant, Annular-low quality category, containing 87% of the data, the standard deviation of the Chen, Shah, and Gungor-Winterton correlations is less than 40%. Moreover, the average discrepancy of the Chen correlation is just 24% and the standard deviation 31%. It is to be noted that the relatively good agreement of the Chen correlation with this data may well be traceable to the inclusion of the phenomenological relationships appropriate to thermal transport in the Annular flow regime, i.e. thin film evaporation, in this correlation.

In the Intermittent regime, the Shah correlation offers the best agreement with the 44 data points with a mean average error of 32% and a standard deviation of 40%. However, the discrepancies between the other correlations and the data in this regime vary from an average of 34% to 72% and standard deviations from 42% to 85%. The five classical correlations were able to predict the heat transfer in the Annular-moderate quality category with a mean average error that

ranges from 37% for Gungor-Winterton (revised) to 54% for Gungor-Winterton, with a standard deviation value of 52% and 92%, respectively.

Shah and Chen correlations have provided the best predictability among classical correlations, and therefore were used later in this dissertation as their predicted heat transfer coefficients were compared to the experimental data.

Chapter 4

The Experimental Apparatus

The experimental apparatus is described in this section. The current apparatus has had two microgap test section installed; short channel and long channel. The short channel was primarily operated on by Ali et al (2010). In the present work, the longer channel was designed to allow for more "uniform" flow to enter the micro-evaporator (test chip) section of the microgap channel in order to eliminate the surface temperature non-uniformity resulting from flow irregularities.

4.1 General Description

The experimental apparatus was designed and built around Intel's the thermal test vehicle (TTV) test chip, based on Intel's Merom microprocessor (Intel 2005). The loop was designed to allow for single phase flow as well as flow boiling of both water and dielectric fluids.

An overall schematic layout of the setup is shown in Figure 4.1. The apparatus consists of the following parts; microchannel evaporator, condenser, reservoir, pump, flow meter, in-line pre-heater, absolute and differential pressure transducers, various thermocouples, as well as 9 thermistors embedded in the TTV die.

The absolute pressure transducer is used to measure the channel inlet pressure, the pressure readings – coupled with the temperature readings of the thermocouple at the channel inlet – are

monitored to confirm the saturation condition at the inlet to the microgap channel, which is achieved by raising the fluid temperature using the in-line pre-heater. The onset of saturated flow boiling is then taking place over the TTV surface.

The flowmeter is a Kobold Pelton wheel type. It requires 5V activation voltage and generates 4 mA to 20 mA current, representing the wheel's revolutions per minute, which are measured by the flow meter embedded optical sensor.

The pump is a KAG M 42x30 – a positive displacement, magnetic-drive gear pump. The pump supplies a maximum pressure of 100 psi or a maximum volumetric flow rate of 9 ml/s.

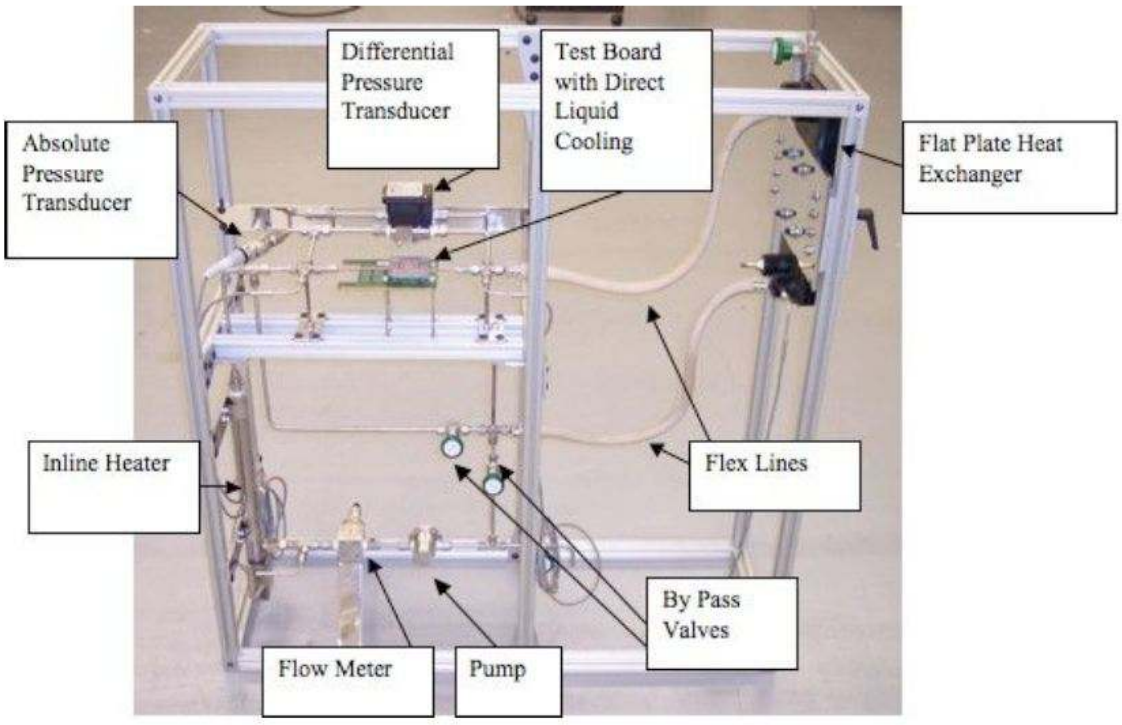

Figure 4.1 The microgap test apparatus

The absolute pressure sensor is a Gems Series 2200. It puts out a current ranging from 4 mA to 20 mA which linearly corresponds to a pressure of – 15 psi to + 45 psi, respectively.

The differential pressure transducer is a Setra Systems Model 230. The sensor emits voltage signal between 0.05 and 5.05 V, which corresponds to a pressure differential of 0 – 2 psi.

The condenser is a flat plate heat exchanger and it can be cooled either by natural convection air or by forced convection water. Water cooling of the condenser was used when boiling experiments took place, in order to condense the working fluid and bring it down to the desired temperature before it goes into the fluid reservoir and again into the pump. A schematic of the experimental apparatus is shown in Figure 4.2.

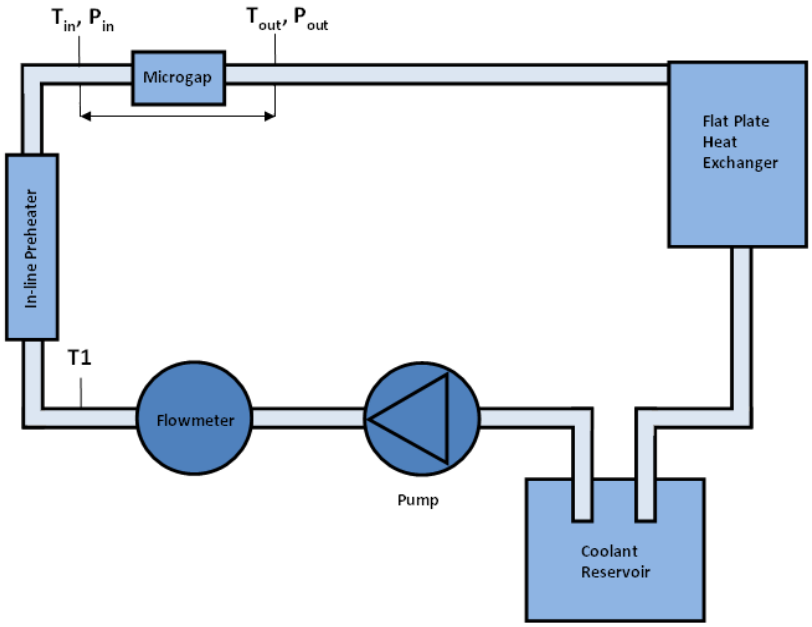

Figure 4.2 Schematic of the test apparatus

4.2 The Chip Thermal Test Vehicle

The experimental apparatus described in paragraph 4.1 was built by Ali (2010) around the thermal test vehicle based on the Intel's Merom microprocessor. The system was designed to enable flow boiling.

The Thermal Test Vehicle (TTV) is a thermal test chip emulating the Intel Merom microprocessor. The chip is packaged in a C4 flip chip die mounted via a BGA layer on an organic substrate. The TTV is depicted in Figure 4.3.

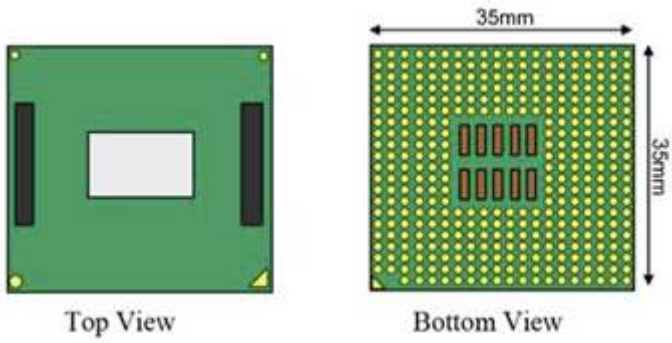

Figure 4.3 Intel Merom processor thermal test vehicle

The TTV is equipped with temperature sensors, Figure 4.4, that are pre-calibrated using a four-wire resistance calibration method.

Figure 4.4 Intel's TTV schematic three different power zones with locations of temperature sensors

Power dissipation on the test chip is generated by powering, via external power supplies, the three serpentine-type heater zones, as in Figure 4.5, embedded in the chip junction plane.

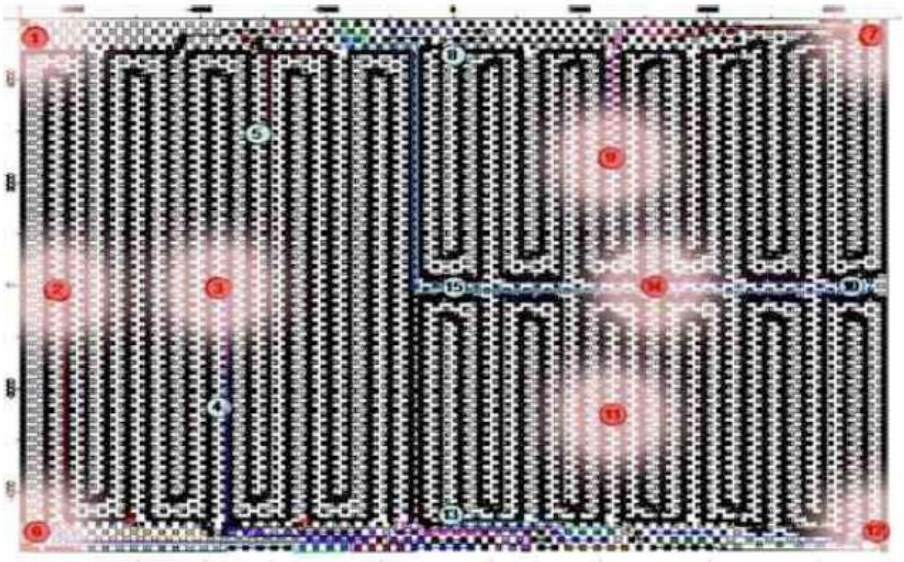

Figure 4.5 Intel's TTV serpentine type heating zone and locations of temperature sensors

These three zones, superimposed in Figure 4.5, at the die area, emulate the half-die (Cache) and the two quadrants (Cores) of the microprocessor. The TTV is enabled to power the heater zones in 3 ways: together to produce uniform power dissipation in the plane of the resistors, the zones can be powered individually, or in various combinations to produce various non-uniform power dissipation distributions. The heat flux achievable for uniform power dissipation is 50 W/cm^2 and it can rise to 200 W/cm^2 for non-uniform power dissipation where the full power is concentrated on one quadrant of the chip area.

The TTV is mounted via a socket connector onto a test board, as shown in Figure 4.6, that provides the connection necessary to power the TTV chip and read the resistors from the temperature sensors and convert them into temperature values through the data acquisition system.

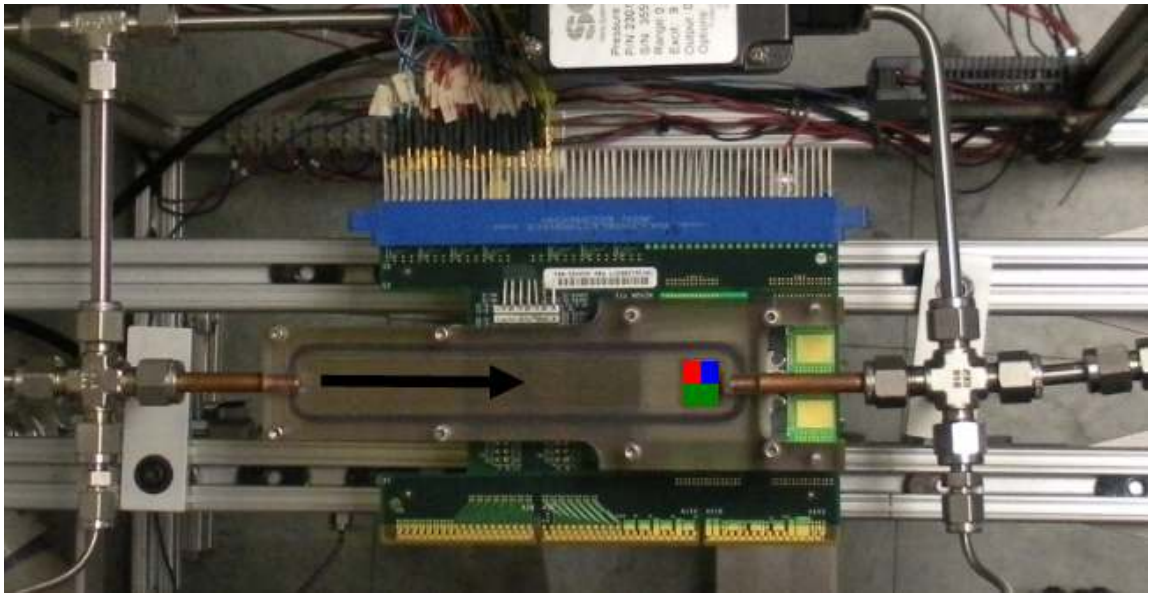

Figure 4.6 Assembled Intel TTV showing locations of the three heater zones

4.3 The Microgap Test Channel

A new test section was manufactured and installed. The test section is a microgap channel pre-evaporator and evaporator built around the TTV. The pre-evaporator section is 125 mm long, creating an L/D ratio that varies between 100 and 500. The motivation behind manufacturing the new test section was the earlier results shown by Ali (2010).

As shown in Figure 4.7, the chip-scale, "short channel" configuration causes flow non-uniformity, the inlet expansion and outlet contraction of the flow affects the thermal performance of the microgap cooler, and predictability of correlations, mostly created for fully developed flow.

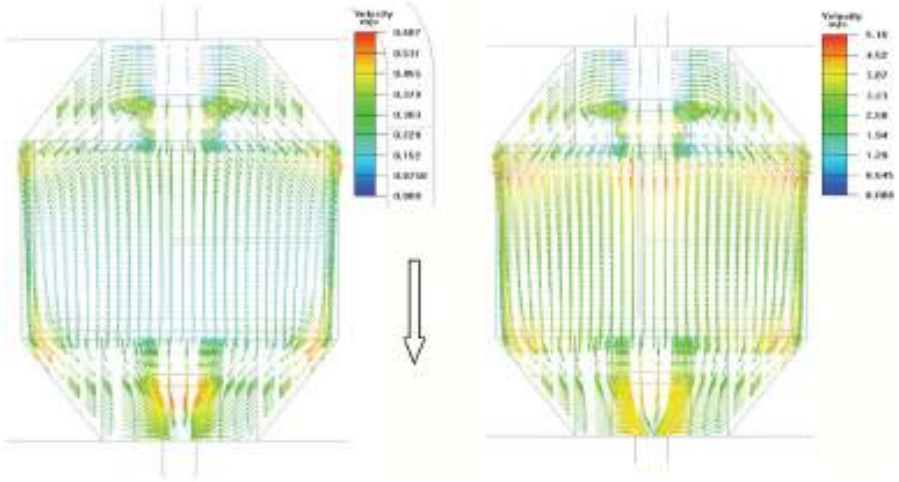

Figure 4.7 Mid-height fluid velocity vectors distribution for a 100-micron uniformly heated microgap channel - (a) 0.7m/s, (b) 6.5m/s, Ali (2010)

The long channel was made of two parts of Polycarbonate (Lexan) and Polyetherimide (Ultem), with the microgap channel formed in between the two walls when the channel is assembled. Thermal and mechanical properties of the Polycarbonate and Polyetherimide used are listed in Table 4.1.

Table 4.1 Thermal properties of Polyetherimide (Ultem) and Polycarbonate (Lexan)

Property	**Polyetherimide (Ultem)**	**Polycarbonate (Lexan)**
Density [g/cc]	1.27	1.34
Thermal Conductivity [W/m-K]	0.22	0.195
Deflection Temperature at 1.8 MPA [^{o}C]	201	143.3

The TTV die serves as a heater, and was aligned to be in plane with the inner surface of the bottom piece which is made of Ultem, and to be integrated as a part of the microgap wall. O-ring was used between the two parts. Details of the assembly can be seen in Figure 4.8, and 4.9.

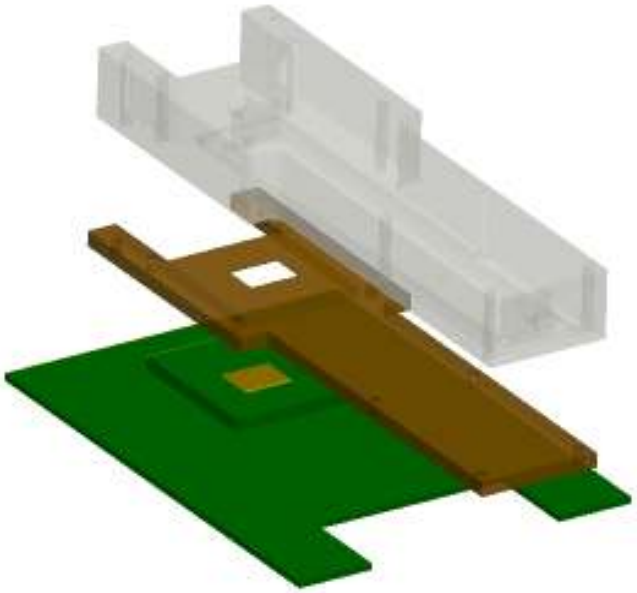

Figure 4.8 Design of the long microgap channel

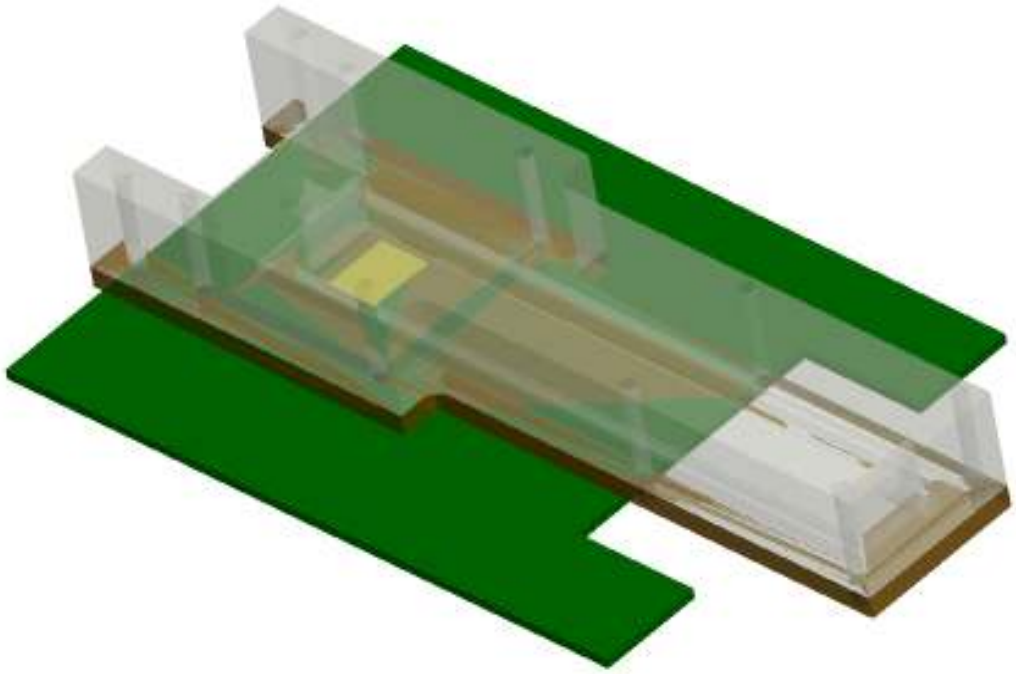

Figure 4.9 The microgap channel assembled

To obtain two-phase heat transfer data, the following experimental procedure was used: the flow rate is set at the desired value and is controlled by monitoring the readings of the flowmeter. The in-line pre-heater is then turned on and controlled through a variable AC transformer, raising the working fluid temperature, until the measured liquid temperature at the inlet to the microgap channel meets the saturated condition at the channel pressure. The input power then is applied to the test chip, raising the temperature of the channel wall and initiating saturated flow boiling in the microgap channel.

The onset of saturated boiling occurs over the surface of the test chip, which is meant to represent a commercially available microprocessor, and is 13.75 mm wide, and 10.47 mm long (in the direction of flow), thus providing a total wetted surface area of 1.44 cm^2.

4.4 Fluid Selection and Properties

Water is an excellent coolant, as it possesses very good thermal characteristics such as high thermal conductivity and high latent heat of evaporation. However, water is electrically conductive and can cause major device failure and IC shorting in the case of leakage. Therefore, dielectric coolants such as 3M's Fluorinert FC's and Novec HFE's are preferred for liquid cooling of electronic packages.

In the present work, 3M engineered dielectric fluids Novec HFE-7100 and Fluorinert FC-87 are used. Both coolants have an Ozone Depletion Potential (ODP) value of zero. However,

HFE-7100 has an additional advantage of possessing a very low global warming potential (GWP). The high GWP of FC-87 is due to its long atmospheric residence time. The properties of the selected fluids are listed in Table 4.2.

Table 4.2 Thermal properties of various refrigerants and coolants

Property	**HFE-7100**	**FC-87**	**FC-72**	**R-134a**	**R-245fa**	**Water**
Chemical Formula	C4F9OCH3	C5F12	C6F14	C2H2F4	CHF2CH2CF3	H2O
Boiling Point (1atm) [^{o}C]	61	30	56	-26	14.9	100
Density [kg/m^{3}]	1510	1650	1680	1377	1366	1000
Surface Tension [N/m]	0.0123	0.009	0.012	0.0153	0.0154	0.0589
Kinematic Viscosity [cSt]	0.38	0.27	0.38	2.74	3.43	2.87
Latent Heat of Vaporization [kJ/kg]	121.2	93	88	212.1	197.3	2257
Specific Heat [kJ/kg-K]	1.25	1.01	1.1	1.28	1.31	4.08
Thermal Conductivity [W/m-K]	0.062	0.059	0.057	0.105	0.084	0.681
Dielectric Constant	7.4	1.73	1.76	9.5	6.82	78.5

Additional fluids are listed in Table 4.2, namely FC-72, a very common electronics cooling working fluid with a boiling temperature at atmospheric pressure of 56.6 ^{o}C, comparable to that of HFE-7100 used in this study (61 ^{o}C). Furthermore, the properties of refrigerants R-134a and R245fa are listed for comparison. These two refrigerants were extensively used in the flow regime database of Revellin and Thome (2006), which was the basis for the comparison and analysis of

different flow regime methodologies presented in Chapter 2. The refrigerants listed in Table 4.2 have higher latent heat of vaporization, and therefore better cooling potential than both FC's as well as HFE-7100. However, both refrigerants are high pressure fluids, requiring running the system at a loop pressure way beyond the modest pressure values normally expected in microgap coolers designated for cooling of electronics. Water is also listed for comparison, as it is the best coolant with the highest latent heat of vaporization, alas it is extremely difficult to continuously provide the system with de-ionized water as required for direct liquid cooling of electronics.

As can be seen in Table 4.2, the fluids used in this work have a significantly different boiling point and latent heat of vaporization. This allowed a wide range of exit vapor qualities as well as wall superheat, as will be seen later in this dissertation.

4.5 Error Analysis

The experimental measurements error can be divided into bias errors and precision errors (Patankar, 1980). The bias error remains constant during the measurements under a fixed operating condition, and it can be estimated by calibration, concomitant methodology, inter-laboratory comparison, and experience. The precision error, however, is affected by the repeatability and resolution of the sensors, the temporal and spatial variation of variables, and variations in operating and environmental conditions during the measurement process. Only the precision error is affected by the aforementioned factors when measurements are repeated under fixed operating condition.

A first order estimate of the uncertainty in the measurement due to the individual errors can be computed by the root-sum-square method, as described by Figliola et al (1995)

$$u = \sqrt{e_1^2 + e_2^2 + ... + e_n^2}$$

(4.1)

Where u is the uncertainty in measurement and e is the elemental error of equipment.

The uncertainty in the measured single-phase pressure drop across the microgap channel is determined by the accuracy of the pressure transducer, the error of the data logger, and it is also linearly dependent on the uncertainty of the flow measurements. Therefore, the resulting uncertainty can be expressed as:

$$\frac{\delta \Delta P}{\Delta P} = \sqrt{\left(\frac{\delta \dot{m}}{\dot{m}} \right)^2 + \left(\frac{\delta V}{V} \right)^2_{read\ out} + \left(\frac{\delta \Delta P_t}{\Delta P_t} \right)^2}$$

(4.2)

Where ΔP is the pressure drop and $\delta \Delta P$ is the uncertainty of pressure drop measurement, and $\frac{\delta \Delta P_t}{\Delta P_t}$ is the error range of the pressure transducer (+/- 0.25% full scale). The accuracy in the flow rate measurements is equal to that of the flow meter, with error range of +/- 1.5% of full scale. The measurement error of the data logger output of DC voltage is 0.05%. Inserting these values into Equation 4.2, the error in the pressure drop measurement is found to equal 1.5%.

Figure 4.10 shows the measurement results of pressure drop of single phase flow of water in the 500 micron gap. The average standard deviation of the experimental results is within 5% of the predicted values by equations 5.1 and 5.2, as will be shown in the following chapter.

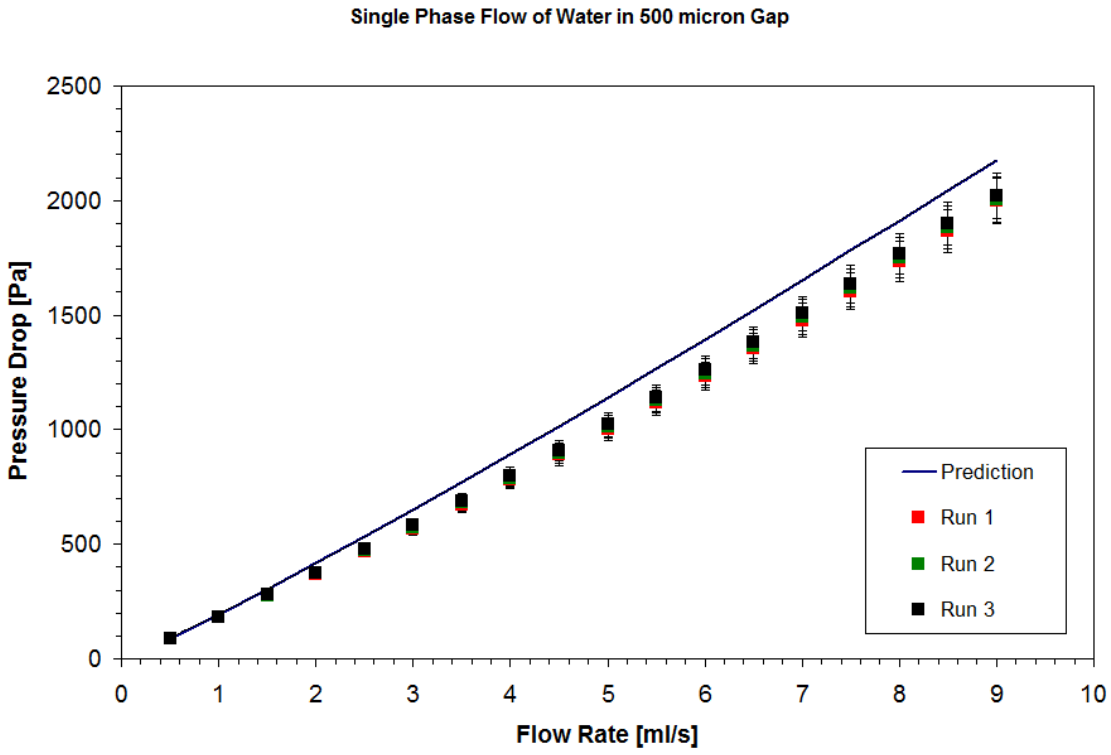

Figure 4.10 Single-phase pressure drop results and repeatability for water flow in 500 micron gap channel at 25^{o}C. Error bars of +/- 5% are added

The uncertainty in the single-phase heat transfer coefficient is linear and is affected by the uncertainties in the measured parameters including flow rate, wall temperature, inlet and outlet temperature, as well as the stability of the data logger and power supply.

The single-phase heat transfer coefficient is obtained from the following equation:

$$h = \frac{q}{A\Delta T}$$

(4.3)

Where q is the heat transfer rate to the coolant, A is the heat transfer area (test chip area), and ΔT is the temperature difference between the heated surface and coolant.

The heat transfer rate can be determined from the energy balance on the channel as:

$$q = \dot{m} C_p (T_{out} - T_{in})$$

(4.4)

Where $\dot{m}$ is the mass flow rate of the working fluid, T_{out} and T_{in} are the measured coolant temperature at the outlet and inlet of the channel, respectively.

Thus, the uncertainty in the single-phase heat transfer coefficient can be expressed as:

$$\frac{\delta h}{h} = \sqrt{\left(\frac{\delta \dot{m}}{\dot{m}}\right)^2 + \left(\frac{\delta q}{q}\right)^2 + \left(\frac{\delta \Delta T_{wall}}{\Delta T_{wall}}\right)^2 + \left(\frac{\delta (T_{out} - T_{in})}{(T_{out} - T_{in})}\right)^2}$$

(4.5)

Where δh is the uncertainty of heat transfer coefficient, $\delta \dot{m}$ is the uncertainty in flow rate which is caused by error in the flowmeter as well as uncertainties in working fluid properties, δq is the uncertainty of input power caused by error of input power, $\delta \Delta T_{wall}$ is the uncertainty in the measurement of wall excess temperature and $\delta (T_{out} - T_{in})$ is the measurement error of the fluid temperature difference of inlet and outlet.

Water is a very well known fluid, and we trust the uncertainty in water properties to be negligible. It was not possible to get the uncertainty in fluid properties of HFE-7100 and FC-87. Single-phase tests were performed for water, and the uncertainty in fluid properties was not accounted for. The error in the flow rate measurement is +/- 1.5%. The error in the Agilent power supply is +/- 2.5%.

The error in the wall (test chip sensors) temperature measurement is defined by the uncertainty in the readings of the embedded sensors. Each sensor (diode) is a 4-wired Ohmic resistance, with an uncertainty of 0.1^{o}C. The maximum possible error in the excess wall temperature is a combination of the error in the measurements of the diodes and the J-type thermocouples. Since the lowest measured wall excess temperature between the test chip and the working fluid is 3^{o}C, , the error in ΔT_{wall} can be estimated as: (0.1+0.2)/3 = 10%.

The error in the J type thermocouples is +/- 0.2 ^{o}C. However, the relative error in $T_{out} - T_{in}$ is assumed as 10% since a 0.2 ^{o}C error yields a maximum of 10% in the heat transfer rate defined in equation 4.4.

Therefore, the maximum uncertainty in measured single-phase heat transfer coefficient is equal to

$$\frac{\delta h}{h} = \sqrt{1.5^2 + 2.5^2 + 10^2 + 10^2} = 0.144 = 14.4\%$$

4.6 Conjugate Heat Transfer and Heat Flux Conversion Rate

In order to account for the heat losses to the ambient, a computational fluid dynamics (CFD) model was developed and tested by Ali (2010) for the TTV test channel. The simulation used a fully conjugate heat transfer model, solving for heat transfer internal to the channel as well as external to it involving convective and radiative heat transfer. The CFD model resulted in a range of conversion rates, i.e. the percentage of the applied heat flux flowing into the channel divided by the full values of the applied heat flux.

For the long channel configuration, the single-phase heat transfer experiment was repeated at the same test conditions performed when the short channel was installed. The long channel single-phase conversion rates were then experimentally verified to be in a very good agreement with those of the short channel, with a discrepancy of only 4% between the two sets.
Therefore, it was decided the short channel two-phase conversion rates calculated by Ali (2010) will be used with the long channel test section throughout this study.

Chapter 5

Single-Phase Data and Discussion

In this chapter, the hydrodynamic and thermal characteristics of the microgap cooler are studied, and preliminary experiments are performed and compared with theoretical prediction.

Single-phase flow of water and HFE 7100 in the microgap channel were studied. The theoretical predictions were compared with the experiment results in order to confirm the reliability of the experimental setup and the validity of measured data.

Since water properties are well known, the measured water single-phase pressure drop results were compared to theoretical predictions, and used to confirm the size of the microgap.

5.1 Single-Phase Pressure Drop

The pressure drop of laminar flow in parallel plate channel can be predicted accurately as it has been studied by numerous researchers. It has been found by Garimella and Singhal (2004) that classical "marco" parallel plate channel correlations can be applied accurately to microgap scale, to channels with hydraulic diameter as small as 250 micron. Generally, the liquid enters the microgap channel through an upstream plenum, and exits the microgap channel through a downstream plenum. Kays and London (1984) correlated the overall pressure drop in a parallel plate channel as:

$$\Delta P = \frac{\rho V^2}{2}\left[(1-\sigma^2+K_C)+4f\frac{L}{D_h}-(1-\sigma^2+K_e)\right] \tag{5.1}$$

Where:

$\frac{\rho V^2}{2}$ is the dynamic pressure associated with the flow

$\sigma_c = \frac{A_C}{A_{in}}$ is the ratio associated with contraction at the channel inlet

$\sigma_e = \frac{A_e}{A_{out}}$ is the ratio associated with expansion at the channel outlet

K_c and K_e are loss coefficients associated with the flow irreversibility.

The friction factor *f* accounts for losses resulting from friction in the channel. Shah and London (1978) correlated the friction factor in a parallel plate channel in the form of:

$$f = \frac{\left[\frac{3.44}{(x^+)^{\frac{1}{2}}} + \frac{24 + \frac{0.674}{4 \cdot x^+} - \frac{3.44}{(x^+)^{\frac{1}{2}}}}{1 + 0.000029 \cdot (x^+)^{-2}}\right]}{Re}$$

(5.2)

Where x^+ is the non-dimensional hydrodynamic axial distance, which is expressed as:

$$x^+ = \frac{\frac{x}{D_h}}{Re}$$

(5.3)

The friction factor asymptotically approaches 96/Re in the fully developed region, i.e. for $x^+ >> 0.1$.

Similarly to Figure 4.10, the pressure drop data of the single-phase flow of water in the 200 micron and 500 micron microgap channels is shown in Figure 5.1 and Figure 5.2, respectively.

Error bars were added to both figures, and the error bars' ranges are equivalent to the standard deviation of the data; 8% for the 200 micron gap, and 12% for the 100 micron gap.

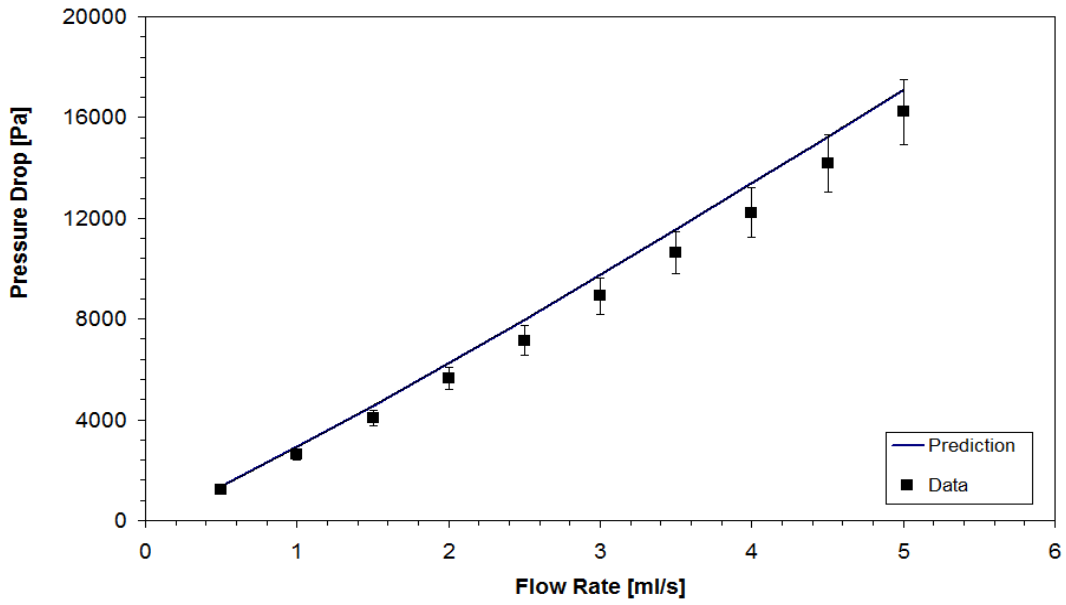

Figure 5.1 Single-phase pressure drop results and repeatability for water flow in 200 micron gap channel at 25°C. Error bars of +/- 8% are added

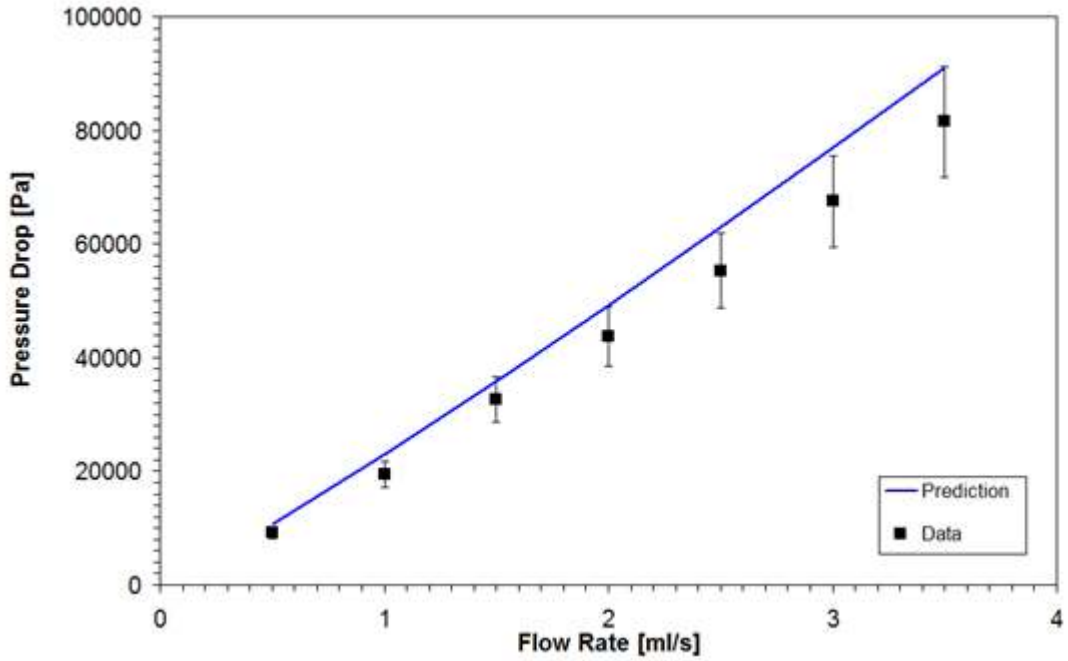

Figure 5.2 Single-phase pressure drop results and repeatability for water flow in 100 micron gap channel at 25°C. Error bars of +/- 12% are added

As can be seen from Figure 5.1 and Figure 5.2, the pressure drop scales with the gap size's cubes, therefore the 100 micron gap is 8 times higher than that of 200 micron microgap channel at the same flow rate. The cube dependence of pressure drop on gap size, along with the good agreement between predictions and measurements, confirms the actual gap sizes are within few microns from the nominal 100, 200, and 500 micron gaps used in this study. The empirically determined and nominal gap sizes are listed in Table 5.1.

Table 5.1 Nominal and empirically determined gap size of microgap coolers used in this study

Gap Size (micron)	
Nominal	**Empirical**
100	110
200	225
500	476

5.2 Single-Phase Heat Transfer

5.2.1 Theoretical Background

The thermal performance of a microgap cooler is evaluated with the non-dimensional Nusselt number, defined as:

$$Nu = \frac{h\ D_h}{k}$$

(5.4)

Where h is the heat transfer coefficient, D_h is the hydraulic diameter, and k is the thermal conductivity of the working fluid.

The hydraulic diameter is calculated as:

$$Dh = 4 \cdot \frac{Microgap Wetted\ Surface}{Microgap\ Perimeter}$$

(5.5)

And the heat transfer coefficient is defined as:

$$h = \frac{q}{A\,\Delta T}$$

(5.6)

Where ΔT is the temperature difference between the heated surface (test chip) and coolant, and q is the heat transfer rate to the coolant.

The heat transfer rate is determined from the energy balance on the channel, as:

$$q = \dot{m} C_p (T_{out} - T_{in})$$

(5.7)

Where $\dot{m}$ is the mass flow rate of the coolant, and C_p is the specific heat of the coolant.

From equations 5.4, 5.6, and 5.7, the empirical Nusselt number can be calculated by the following equation, using the experimental data:

$$Nu = \frac{\dot{m} C_p (T_{out} - T_{in})}{A \Delta T} \cdot \frac{D_h}{k}$$

(5.8)

Kays and Crawford (1966) presented several available Nu number equations for uniform surface temperature as well as uniform heat flux boundary conditions. These correlations were applied to circular tubes and rectangular tubes and cover the laminar flow of fluids for a wide range of Prandtl numbers for both thermally-developing and fully-developed flows. Therefore, single-phase laminar flow heat transfer is a well-established science, and the heat transfer coefficient and Nusselt number can be predicted very well (to +/- 5 – 10%) in most cases, including both symmetric and asymmetric heating.

Mercer et al (1967) performed heat transfer experiment with 12.7 mm parallel plate copper channel with air flow. They correlated their experimental data in terms of the thermally-developing length x*. The local and mean Nusselt number for an isoflux, asymmetrically-heated, parallel plate channel can be predicted with the following equations:

$$Nu_x = \left[\frac{1}{6} - \sum_{n=1}^{\infty} \frac{\exp(-4 n^2 \pi^2 x^*)}{n^2 \pi^2} \right]^{-1}$$

(5.9)

And

$$Nu_m = \left[\frac{1}{6} - \sum_{n=1}^{\infty} \frac{1 - \exp(-4 n^2 \pi^2 x^*)}{n^2 \pi^2} \right]^{-1}$$

(5.10)

Where the non-dimensional thermal axial distance x* is defined as:

$$x^* = \frac{x / D_h}{\mathrm{Re}\,\mathrm{Pr}}$$

(5.11)

5.2.2. Experimental Results

Single-Phase, asymmetric heating heat transfer experiments were performed for all three microgap channels using HFE-7100 and water. The inlet temperature was kept at room temperature (23 – 25 ^{o}C), and flow rate range of 1 – 10 ml/s for water and 2 – 6 ml/s for HFE-7100. The experimental results were compared to the theoretical predictions of equation 5.10. For the single-phase experiment of HFE-7100, the wall temperature was controlled to lower than 40 ^{o}C in order to avoid any pseudo-boiling (air coming out of the solution and inducing boiling-like behavior).

The results show that heat transfer coefficient linearly increased with the flow rate for both fluids. Heat transfer coefficients for water, typically in the range of 25 kW/m^{2}K reached as high as 3 times those of HFE-7100, which peaked at 9 kW/m^{2}K.

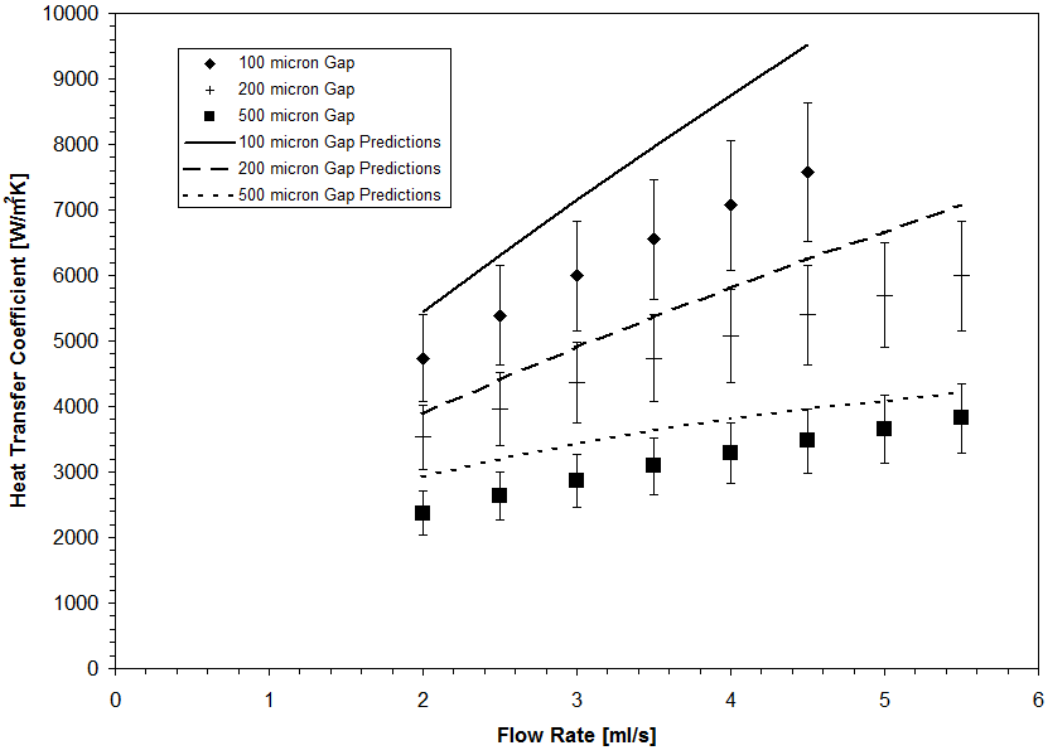

Figure 5.3 Data and theoretical predictions of single-phase heat transfer coefficient of HFE-7100 in different microgap channels Tin = 23°C and q = 10W. Error bars of 14% were added to the data points

As can be seen in Figure 5.3, no single-phase heat transfer experiments were conducted at a flow rate lower than 2 ml/s in order to avoid a heat transfer enhancement phenomenon known as "pseudo-boiling" (dissolved air initiating bubble formation). The discrepancy between measured data and theoretical predictions increases as the gap size decreases.

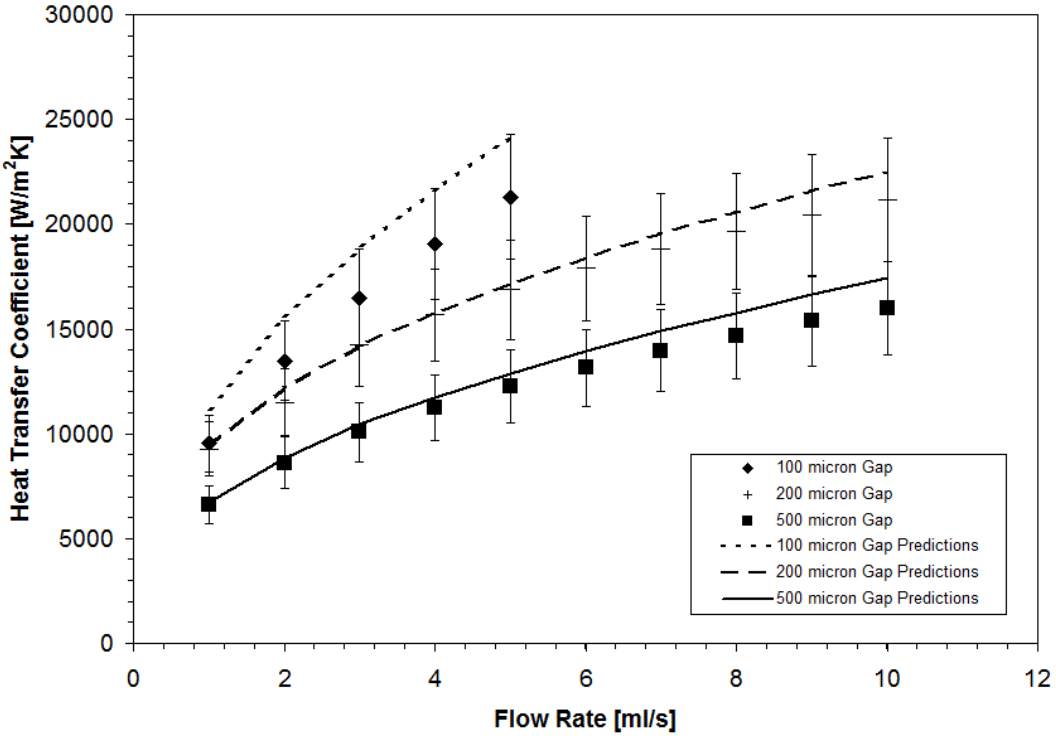

Figure 5.4 Data and theoretical predictions of single-phase heat transfer coefficient of water in different microgap channels. Tin=23 ^{o}C and q = 10 W. Error bars of 14% were added to the data points

The single-phase heat transfer coefficients for water flowing in the different size microgap channels are shown in Figure 5.4. Similarly to the HFE-7100 results, the heat transfer coefficients increase monotonically with the increasing flow rate, which agrees with the predicted behavior by the theory**.** Water results, however, have smaller discrepancy with the theoretical predictions than the HFE-7100. Error bars of 14% – equal to the maximum uncertainty in single-phase heat transfer – were added to Figure 5.3 and Figure 5.4. Moreover, the correlation itself has a 5-10% uncertainty. One more reason for the discrepancy in the HFE-7100 data can be in part due to the well known properties of water, in contrast to the high uncertainty in the properties of HFE-7100 coolant.

Chapter 6

Two-Phase Heat Transfer Data and Discussion

In this chapter, the experimental two-phase flow heat transfer data is discussed. Average and local heat transfer coefficients are presented. While observing the behavior of the average heat transfer coefficient as a function of the channel average vapor quality does not help understand the physics or the heat transport phenomena, it can be useful from an operational point of view in order to get a first order approximation of the channel average wall (test chip surface) temperature. Local heat transfer coefficients, and their change with local vapor qualities, are discussed next, in order to shed more light on the physics of two-phase flow regimes and heat transfer in microgap coolers.

The average and local data is plotted on Taitel-Dukler flow regime maps, and the regime-sorted data is later compared to the predictions of Chen and Shah classical heat transfer correlations.

6.1. Introduction and Basic Relations

Two-phase heat transfer experiments were conducted in three microgap channels with 100, 200, and 500 micron gaps. Two working fluids were used, and both coolants are engineered fluids made by 3M; FC-87 and Novec HFE-7100. All experiments were conducted under saturated conditions.

Two-phase flow boiling experiment was performed with liquid flow rates at the inlet varying from 0.5 to 4.5 ml/s, yielding mass flux varying from 100 kg/m^{2}s to 2500 kg/m^{2}s, while the input power was varying from 3 to 50 W, yielding a heat flux of 2 to 35 W/cm^2 before correcting for heat losses.

The top surface of the test chip is aligned in plane with the inner surface of the bottom half of the microgap channel, as described in Chapter 4. The top part of the microgap channel defines the size of the microgap. The chip is heated by an embedded serpentine heater at the junction plane of the silicon chip, as described in Chapter 5.

The exit vapor quality of the channel is calculated using the following energy equation, which assumes saturation condition at the beginning of micro-evaporator section of the microgap channel:

$$q'' \cdot A = \dot{m} \cdot h_{fg} \cdot x \tag{6.1}$$

Where q'' is the heat flux into the channel, A is the chip surface area, $\dot{m}$ is the mass flow rate, h_{fg} is the latent heat of vaporization, and x is the exit vapor quality.

6.2. Average Two-Phase Heat Transfer Coefficients

The chip average heat transfer coefficient is calculated from the equation:

$$h_{2\phi} = \frac{q''}{(T_{Wall\ Average} - T_{Sat})}$$

(6.2)

Where $h_{2\phi}$ is the two-phase heat transfer coefficient, $T_{wall\ Average}$ is the wall average temperature, and T_{Sat} is the channel average saturation temperature.

And

$$q'' = \eta \frac{V \cdot I}{A_{Chip}}$$

(6.3)

Where q'' is the test chip surface-averaged heat flux, and η is the heat flux conversion rate representing the percentage of the heat transfer rate going into the channel flow as discussed in Chapter 4. V and I are the applied voltage and current from the power supply, with the product giving the input power, and A_{chip} is the test chip wetted surface area.

The wall average temperature was calculated by first averaging the readings of the nine thermistors embedded in the test chip – and located at the junction plane, 800 micron below the chip's top surface – then account for the conduction through Silicon, to calculate the temperature on the wetted (top) surface of the test chip.

The mean average vapor quality, taken at 50% of the exit quality value as calculated in equation 6.1, is used in this section to characterize the two-phase flow in the micro gap channel.

6.2.1. 500 micron Gap Channel

The variation of the average heat transfer coefficient with the average channel vapor quality for HFE-7100 in a 500 micron gap channel is shown in Figure 6.1. The data shown is for mass fluxes of 120, 300, 500, 700, and 1000 kg/m^{2}s, which correspond to liquid flow rate at the inlet of the channel equal to 0.5, 1.5, 2.5, 3.5, and 4.5 ml/s, respectively.

The uniformly applied heat flux was gradually increased until the maximum allowable chip temperature of 110^{o}C was reached. Input power for two-phase flow of HFE-7100 in the 500 micron microgap channel ranged from 5 W to 45 W.

Examining the loci plotted in Figure 6.1, it is seen that the heat transfer coefficient appears to follow a 'U" shaped locus. The onset of flow boiling at an incrementally positive quality is seen to result in a local maximum value of the average heat transfer coefficient. The heat transfer coefficient then decreases, reaching a minimum value at an average quality of 0.5% – 2%, before shifting into an increasing trend and continuing until it reaches another local maximum value, typically attained when the chip is at the maximum allowable wall temperature of 110 ^{o}C. Similar behavior is seen for all but the lowest mass flux value of 120 kg/m^{2}s, which corresponds to a liquid flow rate of 0.5 ml/s. For this mass flux, the average heat transfer coefficient reaches its second maximum at an average quality of just 4.5%, an unlikely value for local dryout, and then resumes the decreasing trend.

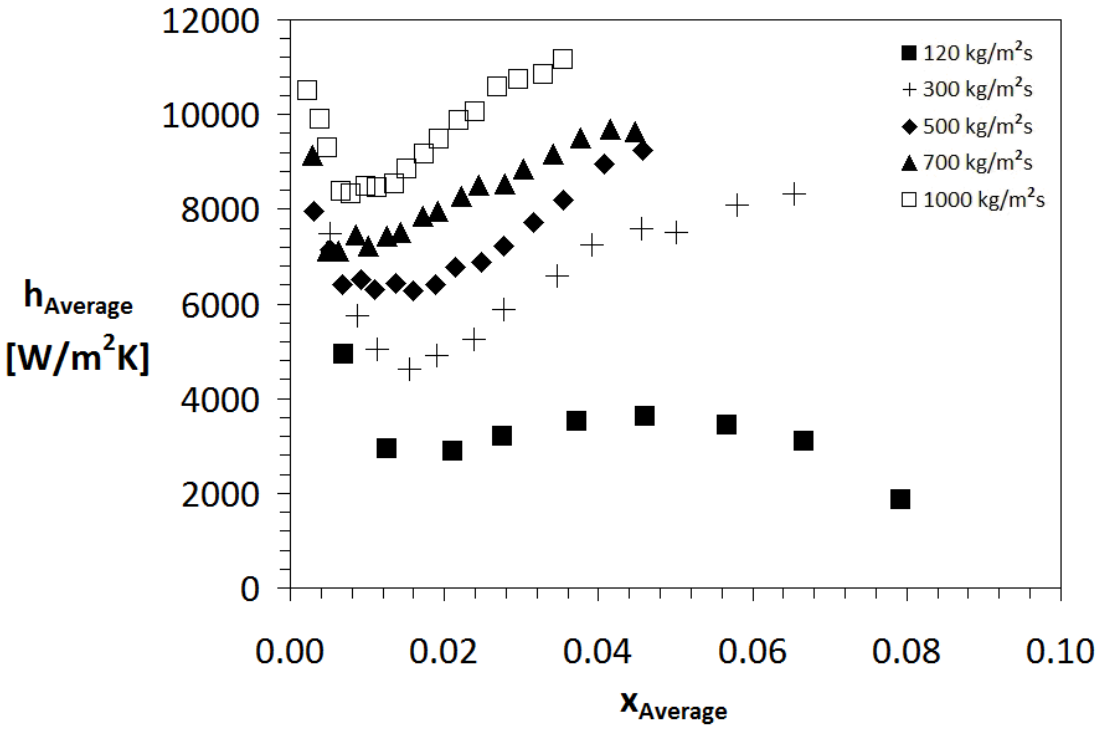

Figure 6.1 Variation of average two-phase heat transfer coefficients with average vapor quality for HFE-7100 flow in 500 micron Channel

The highest values of heat transfer coefficient for this data sub-set reached 11.5 kW/m^{2}K, and they were attained at the highest mass flux of 1000 kg/m^{2}s.

The same data set is shown in Figure 6.2. The corresponding superficial liquid and vapor velocities are plotted on a Taitel-Dukler flow regime map. It can be seen that for all the mass flux values of 120, 300, 500, 700, and 1000 kg/m^{2}s, most of the data falls into the Intermittent regime, with a few data points of each locus in the Annular regime.

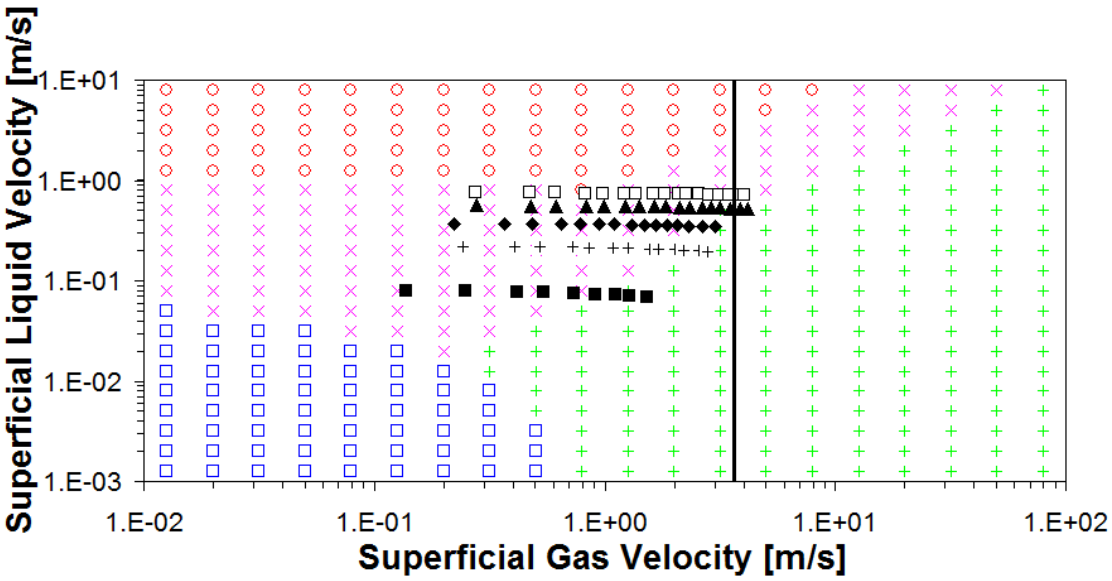

Figure 6.2 Taitel-Dukler flow regime map for flow of HFE-7100 in 500 micron microgap channel. Modified Ullmann-Brauner vertical transition from Intermittent to Annular flow is also shown on the map

The test results of 500 micron gap two-phase heat transfer experiment of coolant FC-87 are shown in Figure 6.3 and Figure 6.4. Similar to the HFE-7100 experiment, these tests were performed for mass fluxes of 120, 350, 550, 800, and 1000 kg/m^{2}s, corresponding to liquid flow rate at the inlet of the microgap channel equal to 0.5, 1.5, 2.5, 3.5, and 4.5 ml/s, respectively. As may be seen in Figure 6.3, for all 5 mass fluxes – including the lowest value of 120 kg/m^{2}s - the heat transfer coefficient follows the previously observed "U" shaped locus, peaking at a very low vapor quality, near the onset of flow boiling, then decreasing sharply, only to recover at moderate vapor qualities, and continue to increase until the maximum chip-allowable temperature of 110 ^{o}C is reached, typically at an input power of 50 W., corresponding to an average channel wall heat flux of 35 W/cm^2.

The highest value of heat transfer coefficient of 17 kW/m^{2}K was reached at the high mass of 1000 kg/m^{2}s, at vapor qualities near the onset of flow boiling. The minima in average h were attained at qualities of approximately 1% to 2.5% and the highest second maxima, of 11kW/m^{2}K, in heat transfer coefficient was achieved at the highest mass flux of 1000kg/m^{2}K .

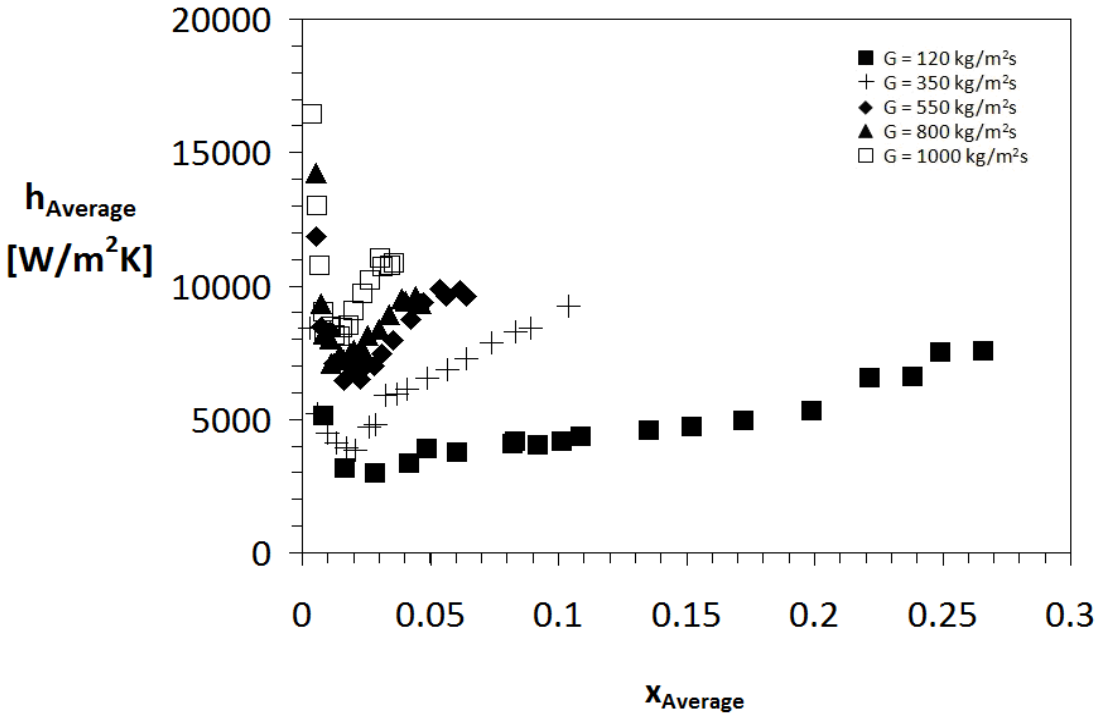

Figure 6.3 Variation of average two-phase heat transfer coefficients with average vapor quality for FC-87 flow in 500 micron Channel

The same experimental results of FC-87 are shown in Figure 6.4, where the corresponding liquid and vapor superficial velocities are plotted on Taitel and Dukler flow regime map, with the vertical transition boundary from Intermittent to Annular flow based on the Ullmann-Brauner model shown on the same map.

FC-87 has a latent heat of vaporization that is 30% lower than that of HFE-7100, which allowed for higher vapor qualities to be reached at the same test conditions. Therefore, exit vapor qualities as high as 60% were achieved, which allowed measuring data deeper into the Annular flow, as can be seen in Figure 6.4.

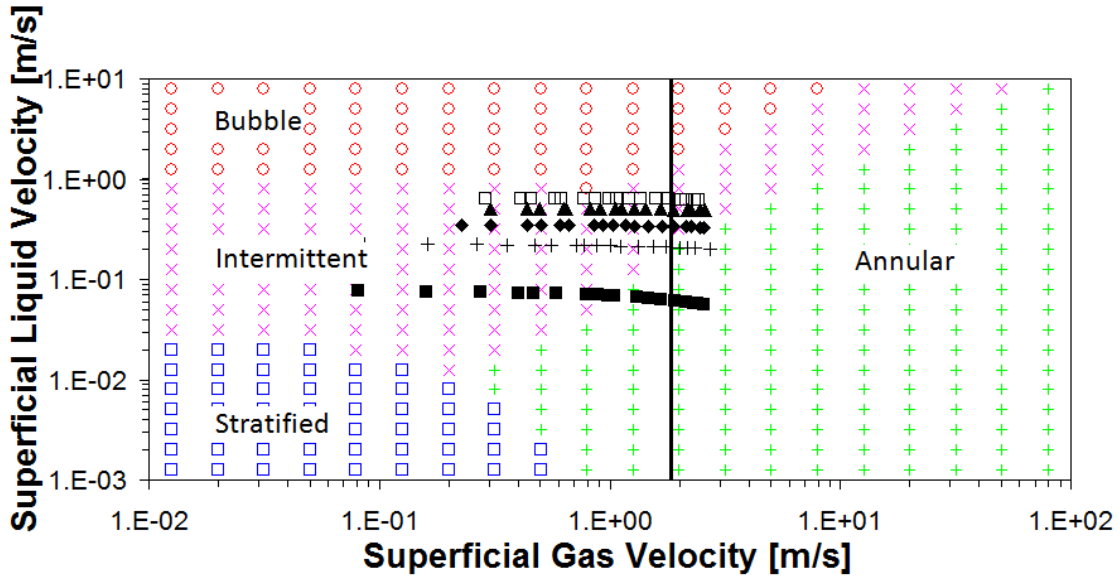

Figure 6.4 Taitel-Dukler flow regime map for flow of FC-87 in 500 micron microgap channel. Modified Ullmann-Brauner vertical transition boundary from Intermittent to Annular flow is added to the map

6.2.2. 200 micron Gap Channel

The variation of the average heat transfer coefficients with the average vapor quality in the 200 micron microgap channel is shown in this section for both coolants used in this work.

Test results for HFE-7100 are shown in Figure 6.5 and Figure 6.6. Liquid flow rate at the inlet were taken at 0.5, 1.5, 2.5, and 3.5 ml/s, corresponding to mass fluxes of 250, 750, 1250, and 1750, respectively. Applied input power ranges from 3 to 43 W, yielding heat fluxes of 2 – 30 W/cm^2. While the observed local maxima and rapid drop in the average heat transfer coefficient at low qualities is similar to that observed for the 500 micron channels, the higher average qualities produce only a gently rising locus that – even at the maximum average quality - falls well below the initial heat transfer coefficient values and, at the lower mass fluxes, seems to show a decreasing trend towards higher vapor qualities.

In these experiments the applied input power ranged from 3 W to 43 W, at which the maximum allowable chip temperature of 110 ^oC was reached. The highest measured heat transfer coefficient for two-phase flow of HFE-7100 in 200 micron microgap channel was at 24 kW/m^2K substantially higher than seen for the 500 micron channel, and it was achieved at the high mass flux of 1750 kg/m^2s. More typically, the average heat transfer coefficient for the 200 micron channel was in the range of 7 kW/m^2K to 10 kW/m^2K.

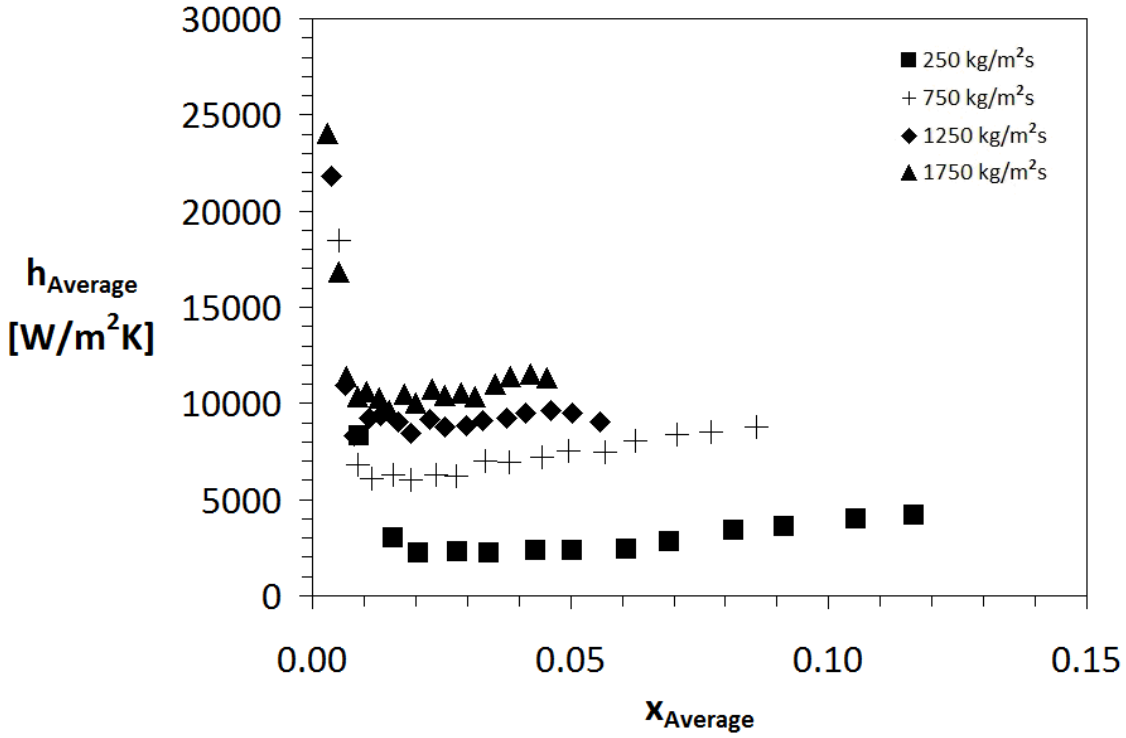

Figure 6.5 Average two-phase heat transfer coefficients plotted against vapor quality for HFE-7100 flow in 200 micron channel

The same test results are plotted on Taitel-Dukler map, with the imposed Ullmann-Brauner vertical transition boundary from Intermittent to Annular. As can be seen in Figure 6.6, most of the data was in the Intermittent flow regime, very few data points were in the transition region between Bubble and Intermittent flow regime, while the high vapor quality data points were predicted to be in the Annular flow regime.

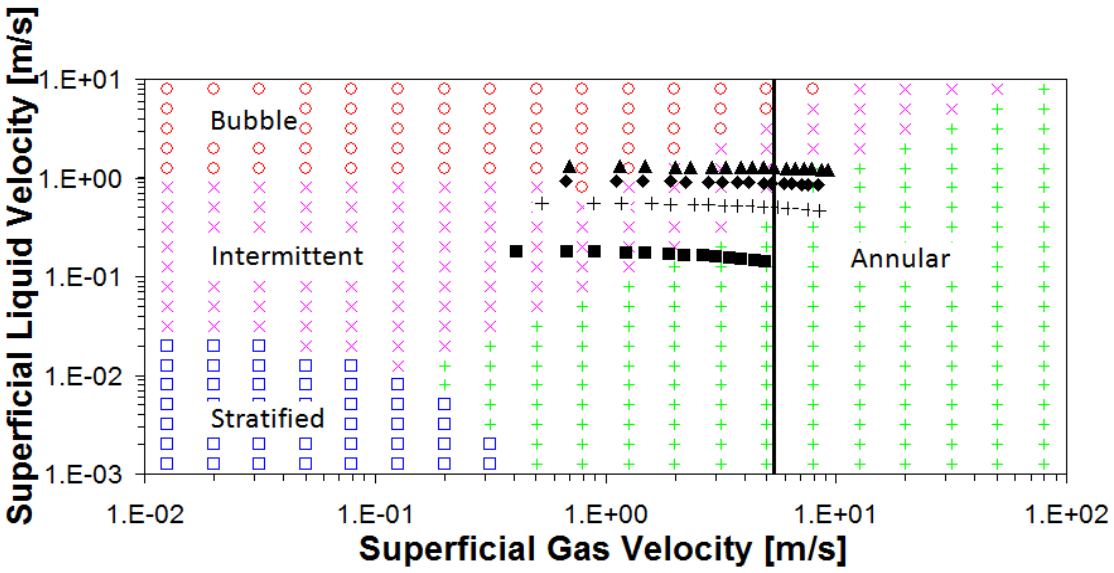

Figure 6.6 Taitel-Dukler flow regime map for flow of HFE-7100 in 200 micron microgap channel. Modified Ullmann-Brauner vertical transition boundary from Intermittent to Annular flow is shown on the map

Similarly, test results for FC-87 in the 200 micron microgap channel are shown in Figure 6.7 and Figure 6.8. Mass fluxes of 300, 800, and 1400 kg/m^{2}s, corresponding to liquid flow rate at the inlet to the microgap channel of 0.5, 1.5, and 2.5 ml/s. The full range of input power varying from 3 W to 50 W was applied to the test chip, yielding a heat flux of 2 – 30 W/cm^2.

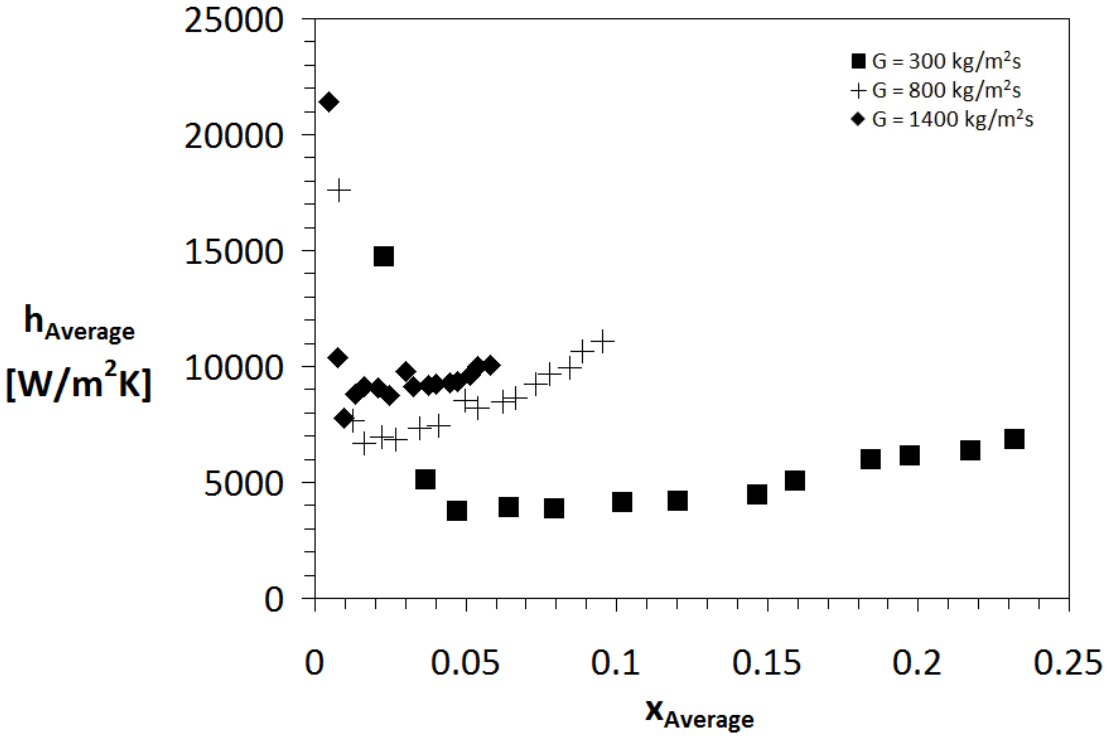

Figure 6.7 Average two-phase heat transfer coefficients plotted against vapor quality for FC-87 flow in 200 micron Channel

In a similar behavior as observed in the FC-87's results in 500 micron gap, the heat transfer coefficients have a maximum value at a very low vapor quality, near the onset of flow boiling, then it decrease with higher vapor qualities before it increases again – although at a moderate rate - as the flow quality increases. Maximum exit vapor quality close to 50% was achieved at the low flow rate of 0.5 ml/s, Maximum heat transfer coefficient value of 22 kW/m^{2}K was achieved at the high mass flux of 1400 kg/m^{2}s. The heat transfer coefficient shows an increasing trend at the higher qualities, especially for the mass flux of 300 kg/m^{2}s. However, further experiment at higher heat fluxes and vapor qualities were not possible due to reaching the test chip's maximum allowable input power of 50 W.

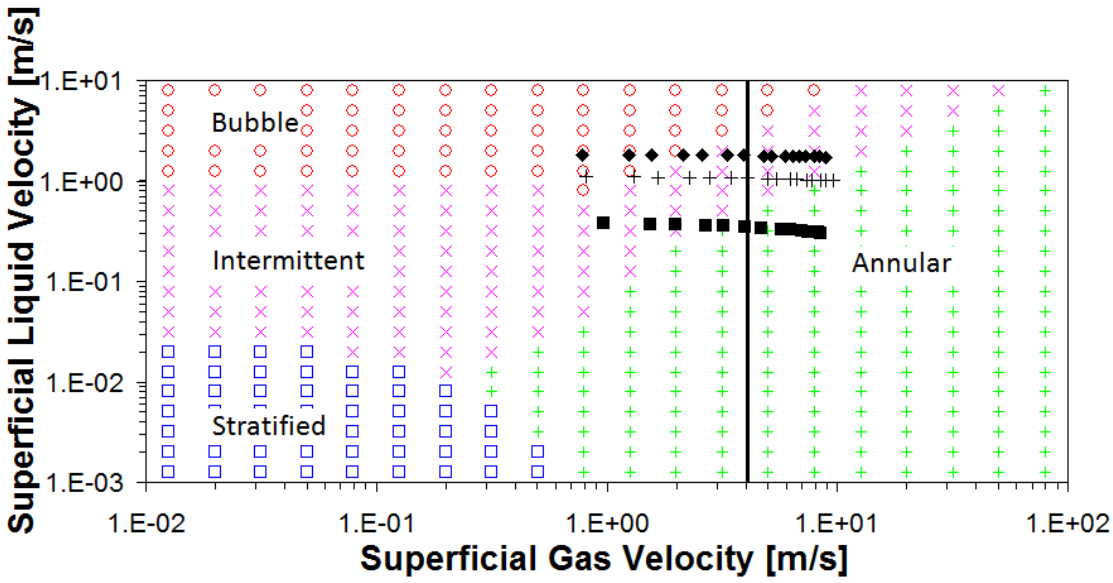

Figure 6.8 Taitel-Dukler flow regime map for flow of FC-87 in 200 micron microgap channel. Ullmann-Brauner transition line from Intermittent to Annular flow is shown on the map

6.2.3 100 micron Gap Channel

Finally, the test results of two-phase flow of HFE-7100 and FC-87 in the 100 micron microgap channel are shown in this section. For HFE-7100, tests were performed with mass fluxes of 500, 1500, and 2500 kg/m^{2}S, or liquid flow rate of 0.5, 1.5, and 2.5 ml/s at the inlet to the microgap channel, respectively. Reflecting the previously observed behavior for the larger channels, as can be seen in Figure 6.9, the heat transfer coefficient peaks at a very low vapor quality, then it decreases with increasing quality, before the loci change trend and show a slightly increasing trend with quality.

Input power within the range of 3 – 40 W was applied, the heat flux ranges from 2 to 28 W/cm^2. The highest maximum exit quality was close to 24%. The maximum heat transfer coefficient of 25 kW/m^{2}K was achieved at the highest mass flux of 2500 kg/m^{2}s.

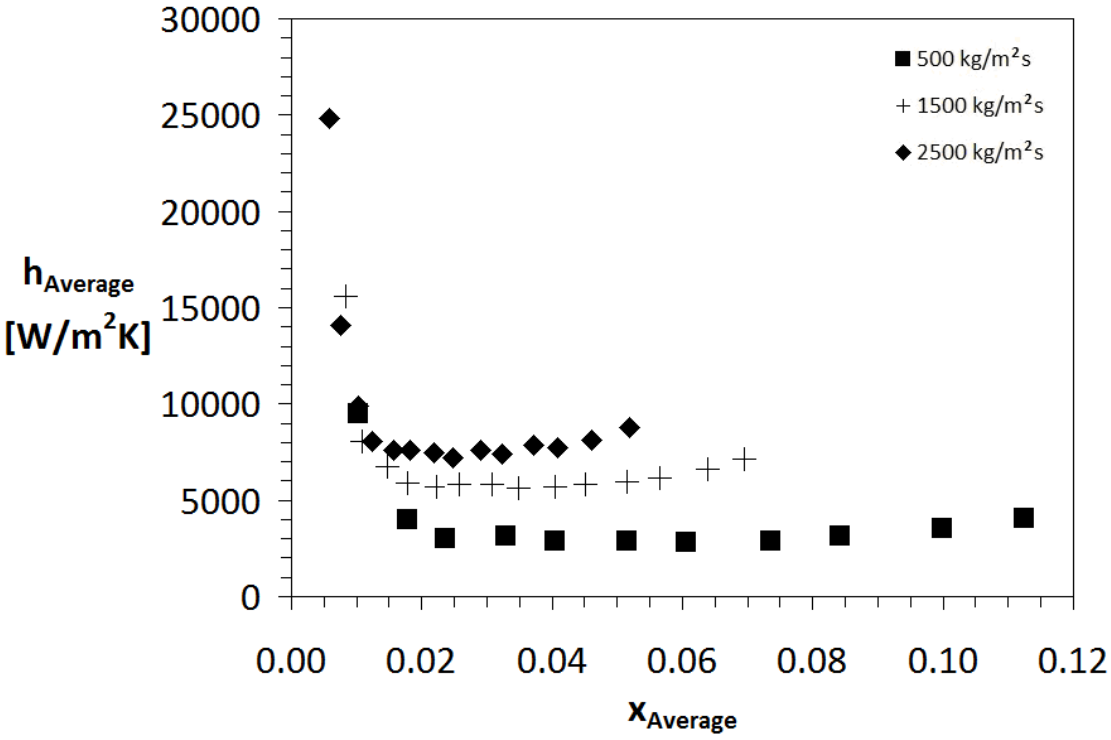

Figure 6.9 Variation of average two-phase heat transfer coefficients with average vapor quality for HFE-7100 Flow in 100 micron Channel

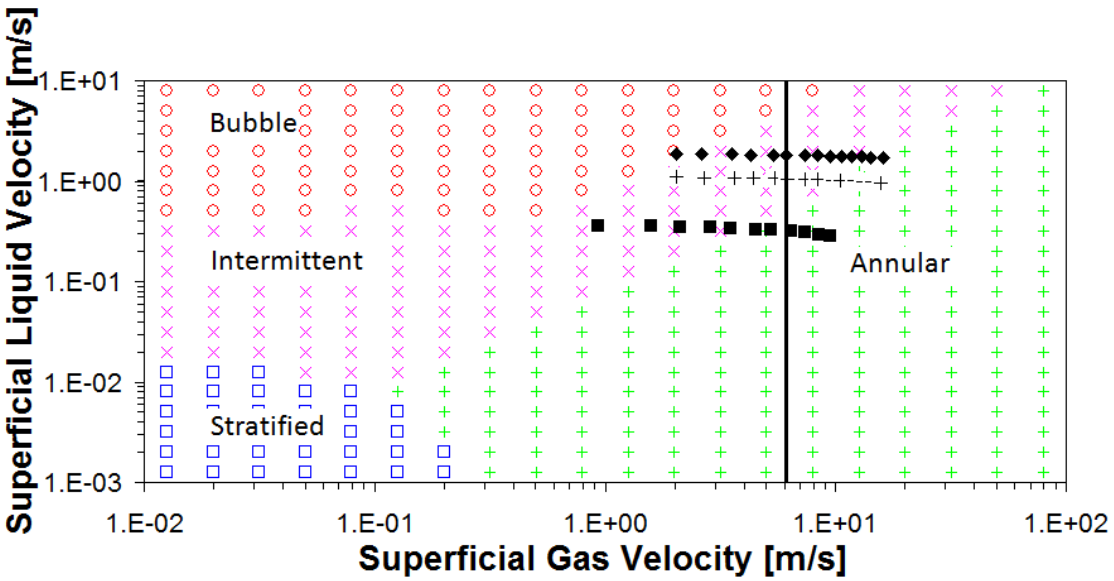

Figure 6.10 Taitel-Dukler flow regime map for flow of HFE-7100 in 100 micron microgap channel. Modified Ullmann-Brauner vertical transition from Intermittent to Annular flow is shown on the map

Test results for average FC-87 two-phase flow in 100 micron microgap channel are shown in Figure 6.11 and Figure 6.12. Input power varies between 3 and 40 W, with the heat flux varying from 2 to 28 W/cm^2. The tests were performed at liquid flow rate of 0.5, 1.5, and 2.5 ml/s at the inlet to the microgap channel. As previously seen in FC-87 results in the 500 micron and 200 micron microgap channels, the average heat transfer coefficient data shows the reverse parabolic or "U" shape as it progresses into higher vapor qualities.

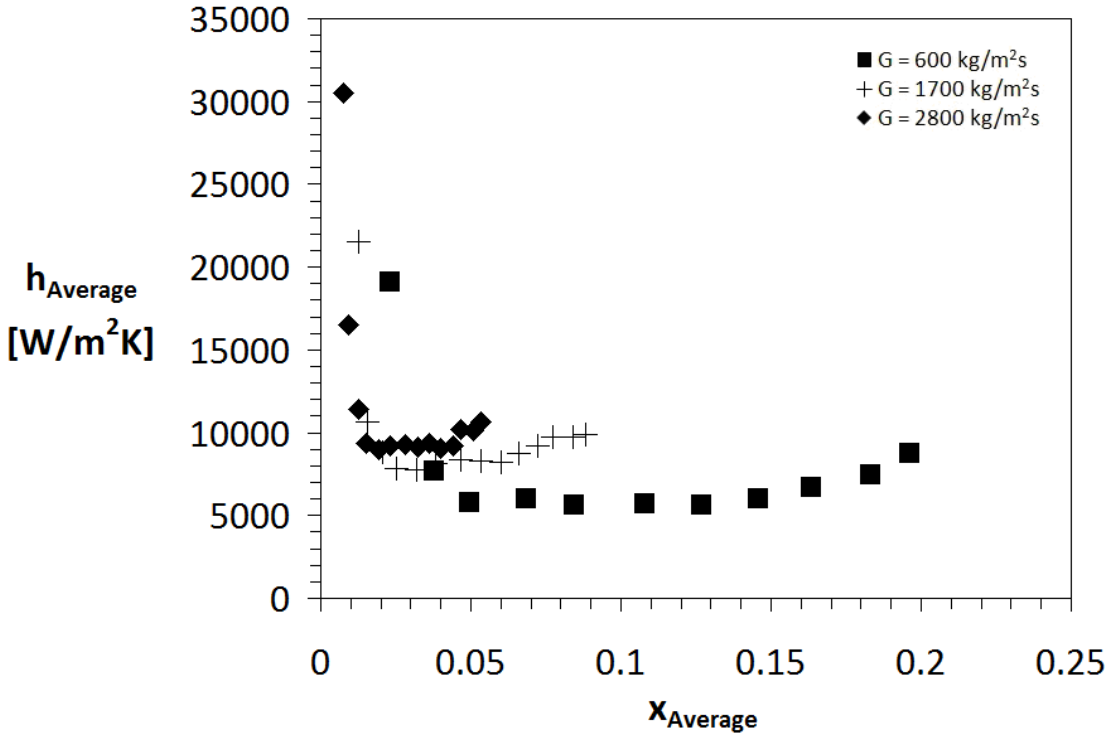

Figure 6.11 Average two-phase heat transfer coefficients plotted against vapor quality for FC-87 flow in 100 micron Channel

The highest average heat transfer coefficient value was reached at the mass flux of 2800 kg/m^{2}s, corresponding to a liquid flow rate of 0.5 ml/s at the inlet to the microgap channel. The heat transfer coefficient then decreases as it later goes through an inflection point near the Intermittent to Annular flow transition. The heat transfer coefficient then retains a positive slope, as the results show an increasing trend in to the Annular flow.

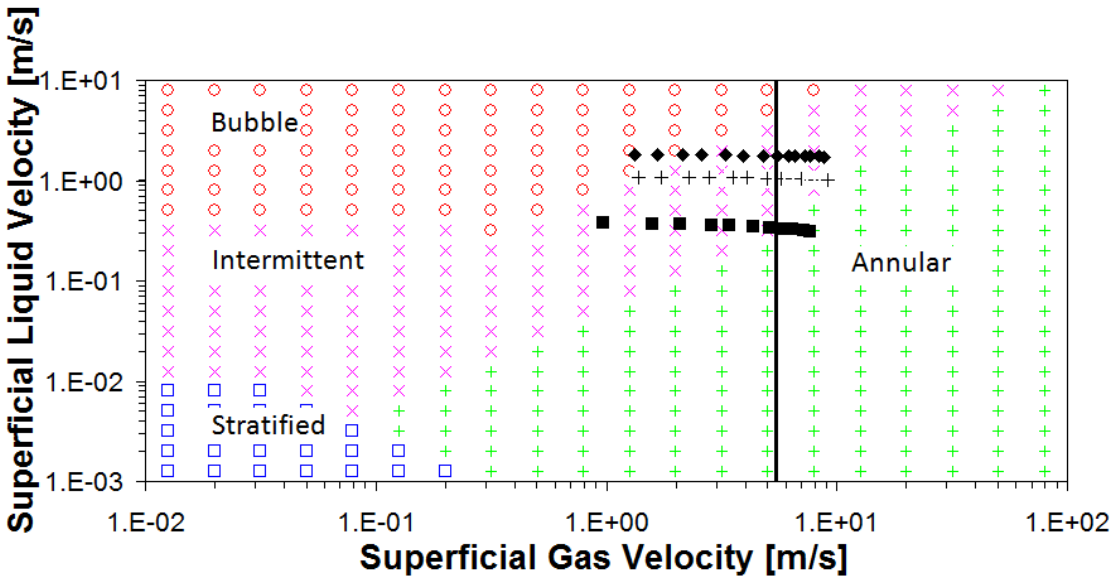

Figure 6.12 Taitel-Dukler flow regime map for flow of FC-87 in 100 micron microgap channel. Modified Ullmann-Brauner Vertical transition from Intermittent to Annular flow is shown on the map

6.3. Local Heat Transfer Coefficient

Knowing the local temperature and heat transfer coefficients is critical from a design and operational point of view. The difficulty of measuring or modeling the local cooling performance stems from not knowing the local heat flux, the local mass fraction of vapor (local vapor quality), nor the local film thickness and vapor volume fraction (void fraction).

To aid in determining the local (or "zonal") values of the heat transfer coefficient, the surface of the TTV chip described in Chapter 4, was divided into 18 section; 3 sections across the

13.75 mm width of the channel, and 6 sections in the flow direction, which has the length of 10.47 mm, as can be seen in Figure 6.13.

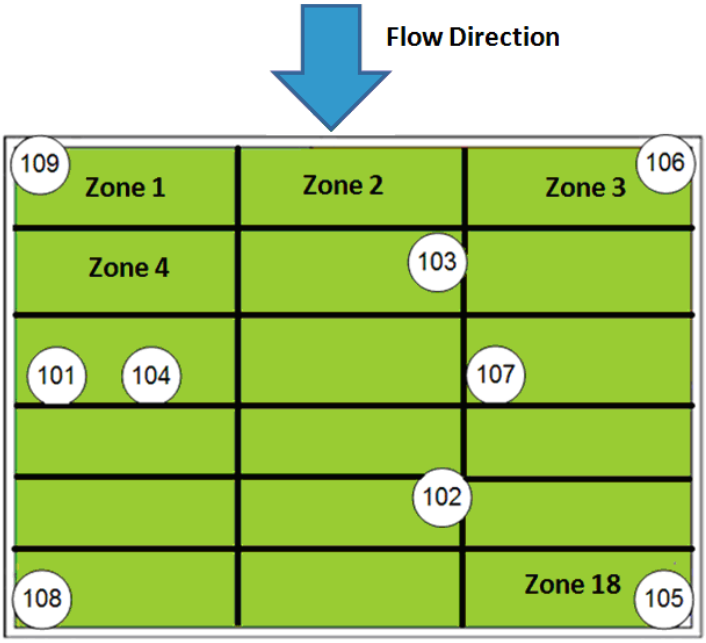

Figure 6.13 The TTV chip with the built-in sensors' locations and the 18 zones configuration imposed on the chip surface

Each of these 18 zones is associated with a "local" heat transfer coefficient. Local heat transfer coefficients were "inversely" calculated using the numerical modeling tool described in the following section.

6.3.1 Numerical Modeling

The finite element method has evolved much over the years, becoming a very useful tool to tackle any conduction problem numerically.

Following an inverse calculation methodology, ANSYS was used in this study to numerically determine the local heat transfer coefficients and subsequently the local heat flux. The heat flux was applied at the serpentine level, at the bottom of the test chip, 800 micron below the surface, and 18 local (zonal) values of heat transfer coefficient, based initially on the previously calculated average value, were applied at the top (wetted) surface of the TTV. ANSYS calculated the conduction through the 800 micron TTV test chip made of Silicon, and the process was repeated until the numerically predicted temperature values matched the experimentally measured temperatures at the location of the 9 sensors.

The governing equation solved in this simulation is the heat diffusion equation. This equation can be derived in a differential control volume, in which the energy entering, leaving, being generated, and being stored are represented in the conservation of energy equality:

$$\frac{\partial}{\partial x}\left(k_x \frac{\partial T}{\partial x}\right)+\frac{\partial}{\partial y}\left(k_y \frac{\partial T}{\partial y}\right)+\frac{\partial}{\partial z}\left(k_z \frac{\partial T}{\partial z}\right)+q'''=\rho C_p \frac{\partial T}{\partial t}$$

(6.4)

Where:

k_x, k_y, and k_z are the thermal conductivity in the x, y, and z directions, respectively. These terms account for heat diffusion through the medium.

q''' is the volumetric heat generation.

ρ is the density and C_p is the specific heat capacity at constant pressure. The term $\rho C_p \frac{\partial T}{\partial t}$ accounts for the amount of energy stored in the control volume over a period of time ∂t.

Equation 6.4 can be expressed using the dell operator as:

$$\nabla \cdot ([K]\nabla[T]) + q''' = \rho C_p \frac{\partial T}{\partial t}$$

(6.5)

Where $[T]$ is the temperature and $[K]$ is the thermal conductivity;

$$[K] = \begin{bmatrix} k_x & 0 & 0 \\ 0 & k_y & 0 \\ 0 & 0 & k_z \end{bmatrix}$$

(6.6)

The ANSYS code simulates the heat flow from the heater level at the bottom of the TTV chip, 800 micron below the surface, through the silicon and into the coolant flow in the microgap channel. The structure has 130200 elements, and 133361 nodes. The test chip's 4 silicon layers and 18 zones were simulated, and the resulting temperatures at the locations of the 9 embedded sensors were saved in an output text file.

First, the TTV heat transfer rate is applied at the bottom of the test chip (at the level of the serpentine heater) 800 micron below the wetted surface. Then, 18 initial local heat transfer coefficients are applied at the top (wetted) surface. For the initial run, the heat transfer coefficient values were set to be equal to the chip average heat transfer coefficient, the initial surface temperature profile is then determined from the first run.

Next, temperatures at the locations of the 9 thermistors are compared to the experimental data at the same locations, based on the discrepancy between the measured temperature and initial numerical results, the local (zonal) heat transfer coefficients are modified, and the new heat transfer coefficients are applied for the next run. The process is then repeated until the discrepancy

between the numerical and experimental results is within 1^{o}C. Typically, the number of iterations does not exceed 5 runs before the targeted agreement was achieved.

The initial and final results for the test condition of FC-87 flowing in 100 micron channel at 500 kg/m^{2}s under input heat of 30 W are shown in Figures 6.14 and Figure 6.15, the same data subset is also shown later in Figure 6.16 and 6.17.

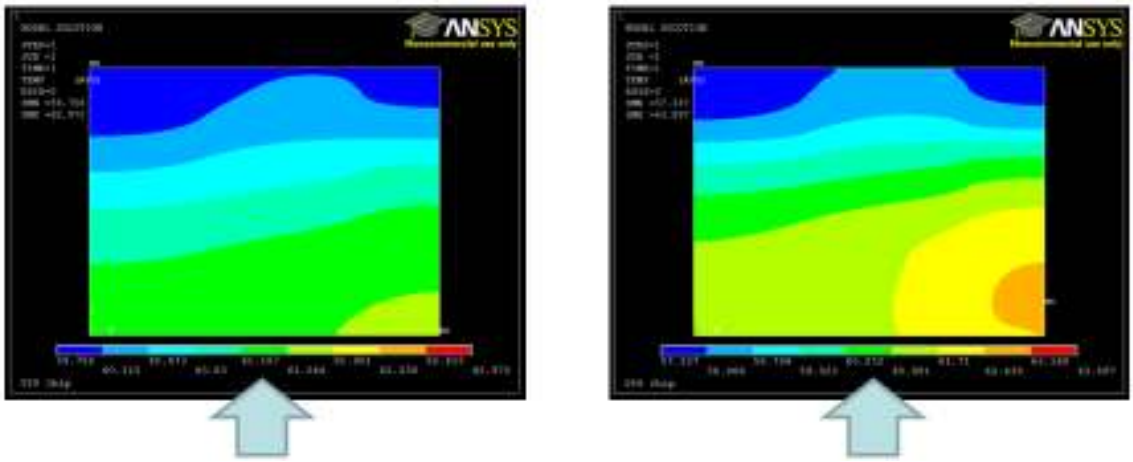

Figure 6.14 Local temperatures obtained from ANSYS; Initial run (left) and final run for FC-87 in 100 micron microgap channel, flow rate of 0.5 ml/s, and input power of 30 W

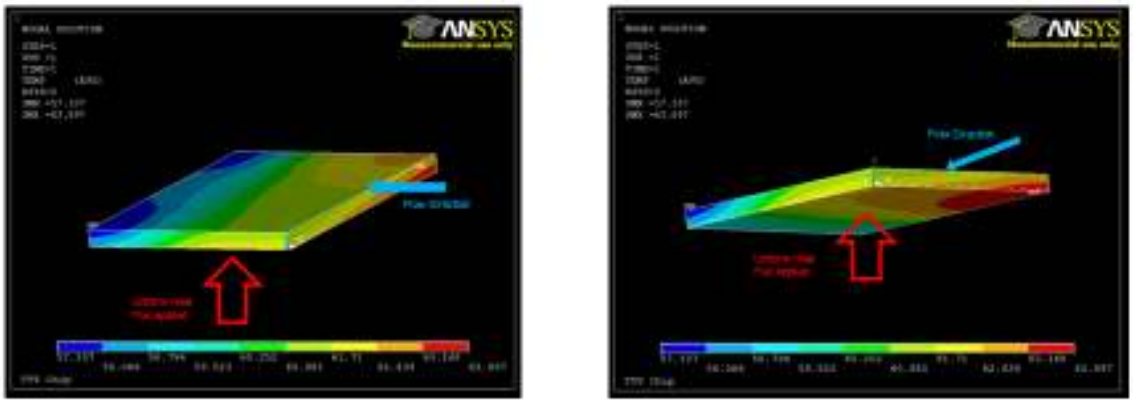

Figure 6.15 Local temperatures obtained from ANSYS; Final run of FC-87 flow in 100 micron microgap channel, flow rate of 0.5 ml/s, and input power of 30 W

As can be seen in Table 6.1, the numerical predictions and experimental measurements of surface temperature for the case of 2.5 ml/s flow of HFE-7100 with the applied input power of 40 W are presented. It can be seen that the greatest discrepancy for the present case was equal to 0.8 ^{o}C in temperature measured at sensor 101, 102, and 109..

Table 6.1 Numerical predictions and experimental results compared for two-phase flow of FC-87 in 100 micron microgap channel

Sensor #	Numerical		Experiment
	1st Iteration	Final Iteration	
101	61.7	62.1	62.9
102	60.9	59.7	58.9
103	61.8	61.9	62
104	61.7	61.9	62.1
105	60.4	58.1	58.7
106	61.9	61.6	60.9
107	61.4	61.1	61
108	60.7	58.4	57.9
109	62.2	63.1	62.5

The above process was repeated for all 345 test conditions, including 172 tests for HFE-7100 and 173 tests for FC-87. After running the data through the ANSYS model, each one of the 345 test conditions yielded 18 zonal heat transfer coefficients values, resulting in a total of 6210 local heat transfer coefficient values. The local temperatures and local heat transfer coefficients and heat fluxes were documented. The respective local conditions were used in the comparison of local heat transfer coefficients to classical correlations, as described later in this chapter.

6.3.2. Local Heat Transfer Coefficient Data and Discussion

In this section, selected local heat transfer coefficient data subsets are presented. The local heat transfer coefficients are plotted against local vapor qualities, and later the corresponding superficial liquid and vapor velocities are plotted on the Taitel-Dukler flow regime maps.

6.3.2.1 Effect of Mass Flux on Local Heat Transfer Coefficient

In this section, the effect of mass flux on local heat transfer coefficient will be examined. For two-phase flow experiment of FC-87 in 100 micron gap channel, three values of mass flux were applied. In this section, data measured at the maximum heat flux applied at each of these mass fluxes of 500, 1500, and 2500 kg/m^2s will be presented. The local heat transfer coefficients will be also compared to the predictions of Chen and Shah classical correlations.

a. Local Heat Transfer Coefficients of FC-87 in 100 micron Gap (G=500 Kg/m^2s, $q''= 19W/cm^2$)

The same test condition that was analyzed and presented in Figure 6.14 and 6.15 is also shown in Figure 6.16. Following the determination of the local temperature and heat flux condition, the local heat transfer coefficients are documented and presented in Figure 6.16.

As can be seen in Figure 6.16, the local heat transfer coefficient for the 500 kg/m^{2}s flow of FC-87 in a 100 micron microgap channel reaches a value of 8 kW/m^{2}K at a vapor quality of 0.05 near the inlet to the evaporation section (wetted surface of the test chip) of the microgap channel. The local heat transfer coefficient then decreases as the vapor quality increases, until it reaches a minimum value of 6.2 kW/m^{2}K at a vapor quality of 0.2, at which the heat transfer coefficient locus goes through an inflection point, and then changes to a positive slope, as it reaches a local value of 11 kW/m^{2}K at a vapor quality of 0.4 near the exit of the microgap channel.

The local data is compared to the prediction of the Chen and Shah classical correlations. It can be seen that typically Chen under-predict the heat transfer coefficient and Shah over-predict the heat transfer coefficient.

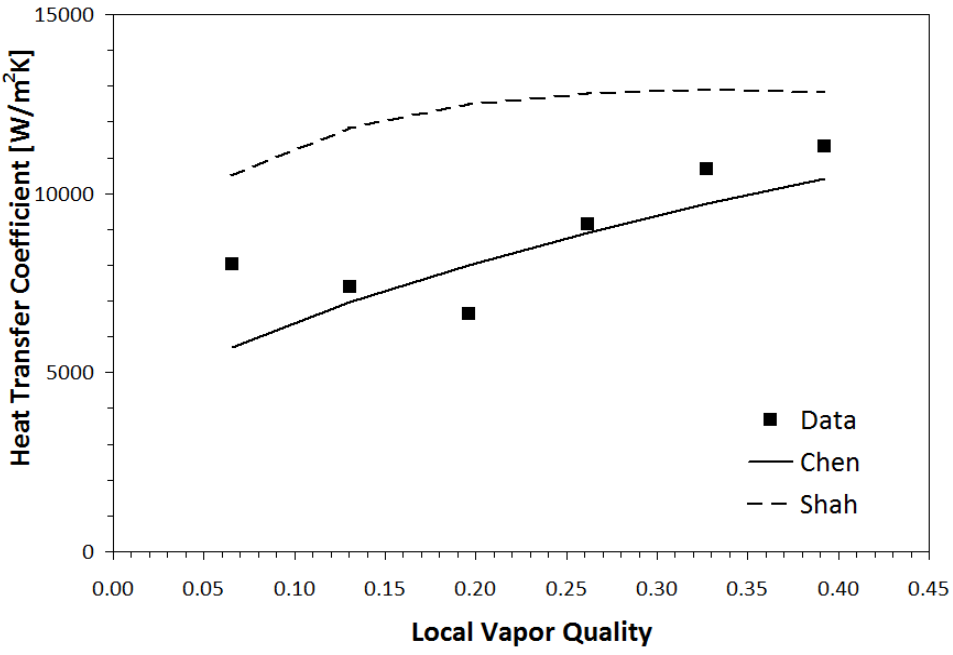

Figure 6.16 Local heat transfer coefficient and vapor quality, FC-87 in 100 micron channel, mass flux of 500 kg/m^{2}s, and the applied heat flux is 19 W/cm^2

The same local data subset is plotted on Taitel and Dukler flow regime map, presented in Figure 6.17. It can be seen that the heat transfer coefficient inflection point at vapor quality of 0.2 is actually in the vicinity of the channel flow regime transition from Intermittent to Annular flow. The increasing branch of the heat transfer coefficient is in the Annular flow, in agreement with previous observations of the literature data, which lead us earlier to defining the M-shape characteristic heat transfer coefficient curve. The current data presented in Figure 6.16 and 6.17 spans across the middle section of the M-shape curve.

It can be seen in Figure 6.17 that Annular data is much closer to Chen, while Intermittent data has almost an equal discrepancy with Chen and Shah.

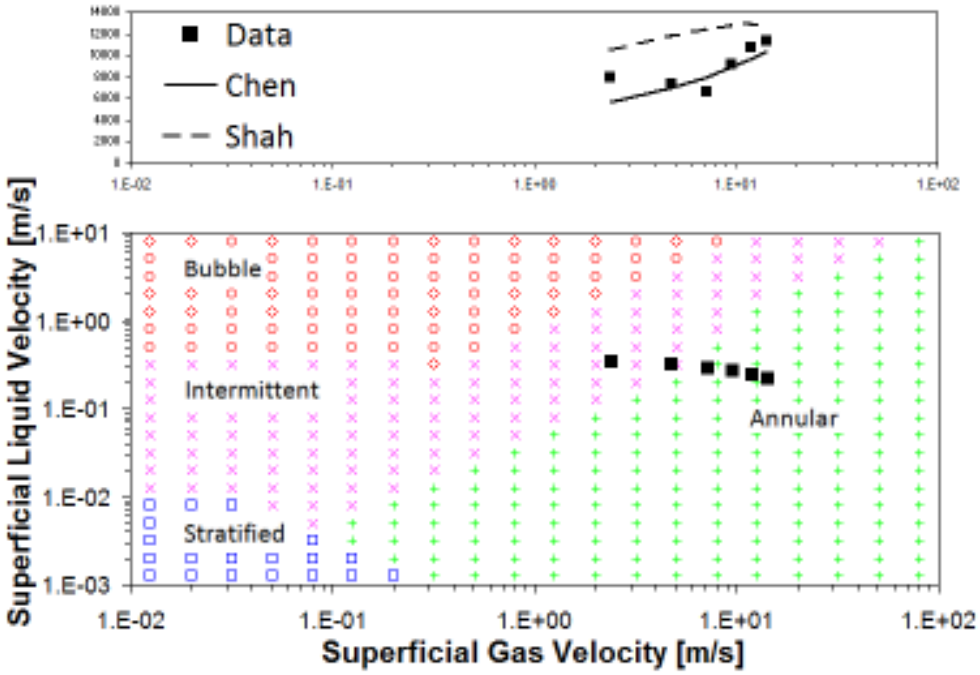

Figure 6.17 Taitel and Dukler flow regime map for local heat transfer coefficient and vapor quality, FC-87 in 100 micron channel, mass flux is 500 kg/m^{2}s, and the applied heat flux 19 W/cm^2

b. Local Heat Transfer Coefficients of FC-87 in 100 micron Gap (G=1500 Kg/m^{2}s, q''= 26W/cm^2)

The local heat transfer coefficients of the flow of 1500 kg/m^{2}S of FC-87 in 100 micron microgap channel, under an applied heat flux of 26 W/cm^2 are shown in Figure 6.18. The heat transfer coefficient reaches a peak value of 13.5 kW/m^{2}K at a very low vapor quality of 0.03, and it decreases down to 11 kW/m2K at a vapor quality of 0.09. The local heat transfer coefficient then fluctuates between 11 kW/m^{2}K and 12 kW/m^{2}K until it exits the channel at a vapor quality of 0.18. The data subset is mostly bounded by the predictions of Chen and Shah, with the exception of the last data point, with Chen under-predicting the heat transfer coefficient and Shah over-predicting the heat transfer coefficient.

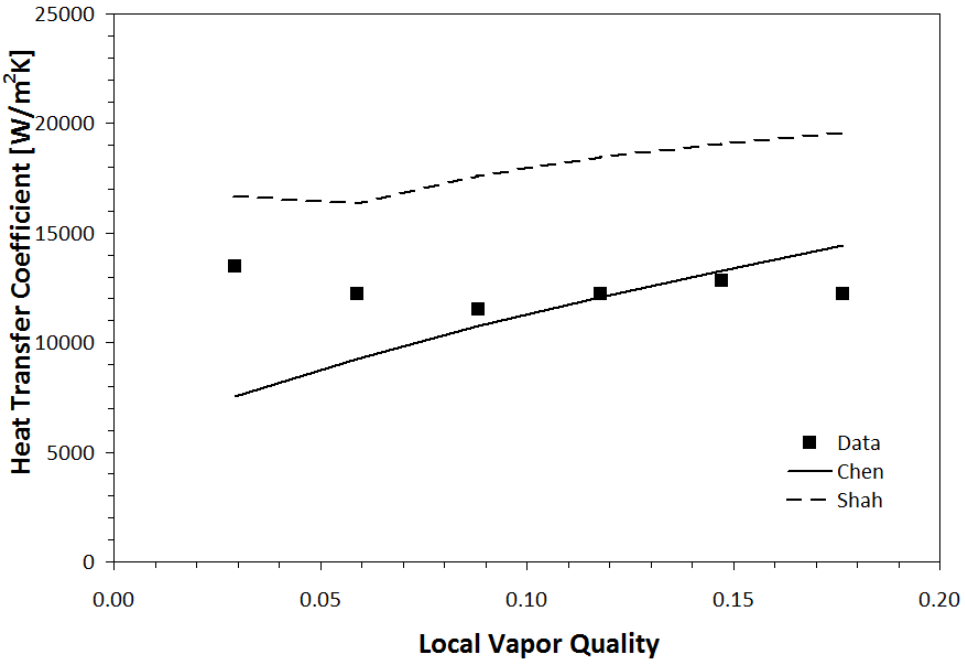

Figure 6.18 Local heat transfer coefficient and vapor quality, FC-87 in 100 micron channel, mass flux is1500 kg/m^{2}s, and the applied heat flux is 26 W/cm^2

The same data subset is plotted on Taitel-Dukler flow regime map in Figure 6.19. It can be seen that the minimum value in heat transfer coefficient occurred near the transition from Intemittent to Annular flow. The maximum exit quality of this data subset is only 0.18. The relatively low exit vapor quality of this data subset is the reason why the channel flow did not reach far enough into the Annular flow, which subsequently did not allow the thin liquid film evaporation to become the dominant heat transfer mechanism, unlike what was likely the case for the previous subset presented in Figure 6.16 and Figure 6.17.

It can also be seen from Figure 6.19 that Intermittent data is falling between Shah and Chen predictions, while the Annular flow data is much closer to Chen predictions than Shah predictions.

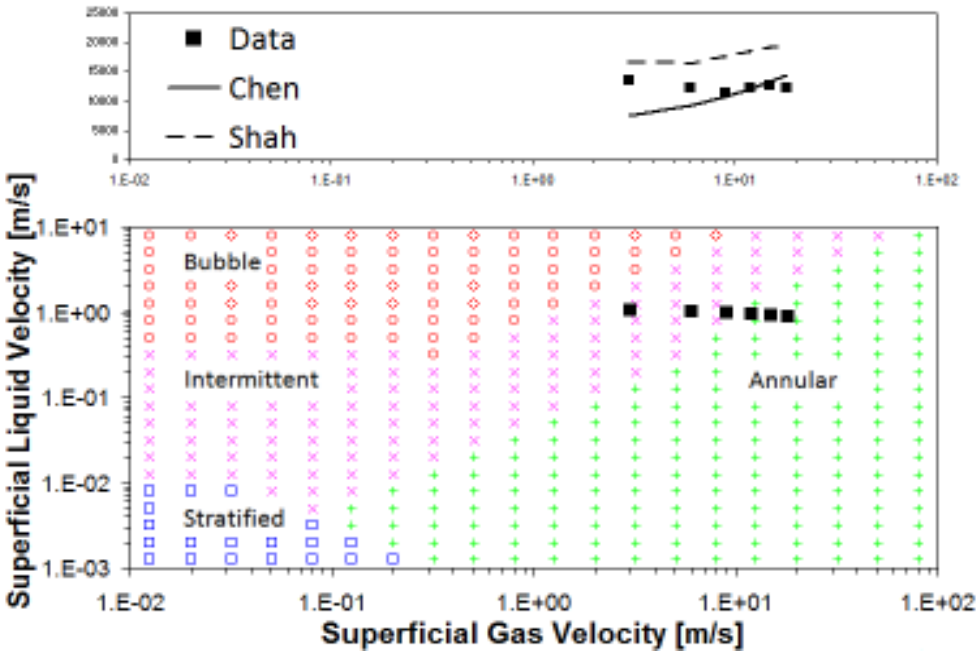

Figure 6.19 Local heat transfer coefficient and vapor quality, FC-87 in 100 micron channel, mass flux is 1500 kg/m^{2}s, and the applied heat flux is 26 W/cm^2

c. Local Heat Transfer Coefficients of FC-87 in 100 micron Gap (G=2500 Kg/m^{2}s, q''= 26W/cm^2)

The third selected subset of local heat transfer coefficient data to be presented is for a 2500 kg/m^{2}s flow of FC-87 in 100 micron microgap channel, under an applied heat flux of 26 W/cm^2. The local heat transfer coefficient has a maximum value of 16 kW/m^{2}K at a vapor quality of 0.02, then it decreases to 11 kW/m^{2}K at a quality of 0.09, and stays around the same value with a slight increase to 12 kW/m^{2}K at a quality of 0.11 at the exit of the microgap channel.

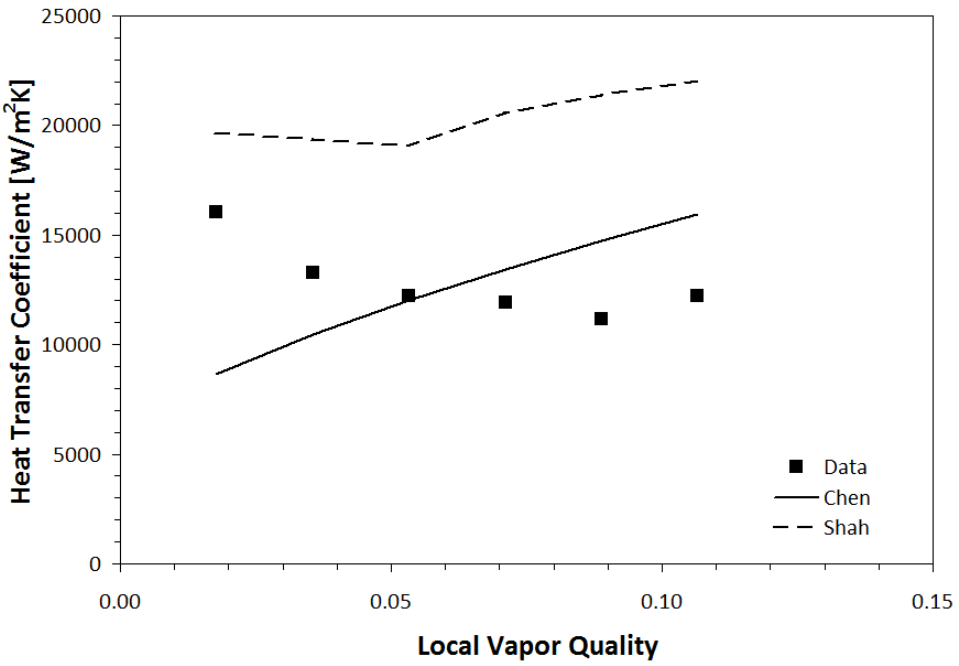

Figure 6.20 Local heat transfer coefficient and vapor quality, FC-87 in 100 micron channel, 2500 kg/m^{2}s, 26 W/cm^2

As can be seen in the Taitel-Dukler map representing this test condition and plotted in Figure 6.20, the data is mostly in Intermittent, and it crosses over to Annular toward the exit of the channel. The Intermittent data is closer to the prediction of Shah at the lowest vapor quality, and it get closer to Chen near the Intermittent-to-Annular transition boundary. The Annular data is much closer to Chen than Shah. However, both correlations did over-predict the local Annular heat transfer coefficient for this case, which is rather unusual as most data usually falls in between the predictions of the two correlations.

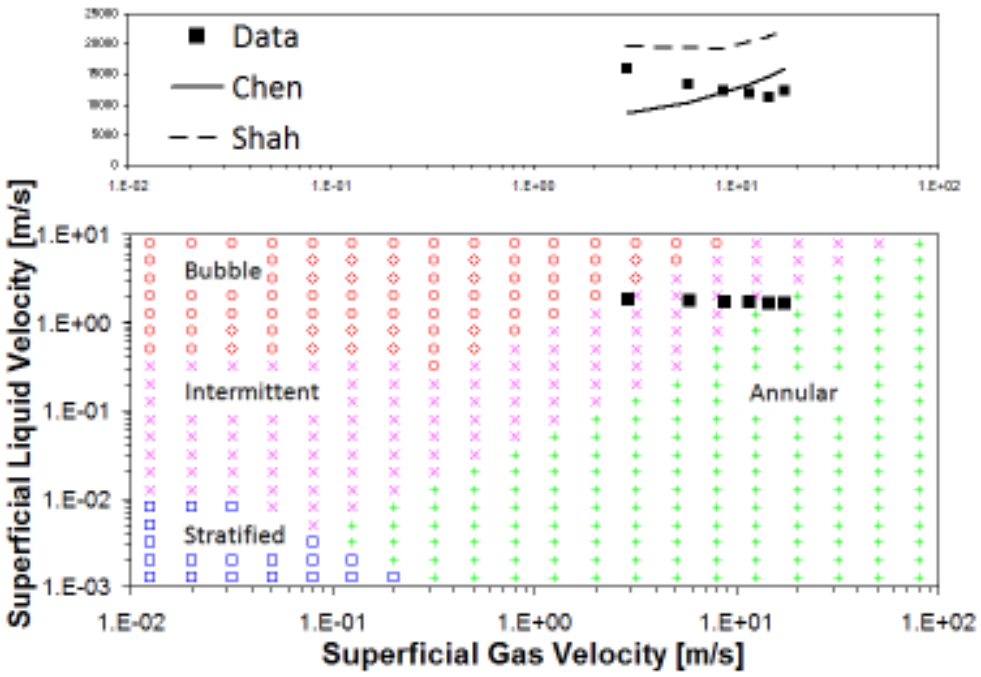

Figure 6.21 Taitel and Dukler maps for Local heat transfer coefficient and vapor quality, FC-87 in 100 micron channel, the mass flux is 2500 kg/m^{2}s, and the applied heat flux is 26 W/cm^2

6.3.2.2 Effect of Heat Flux on Local Heat Transfer Coefficient

In this section, the effect of increasing heat flux will be presented. The results presented in this section are for FC-87 flow in 500 micron microgap channel at a constant mass flux of 350 kg/m^{2}s. Local heat transfer coefficient will be presented, and compared to the predictions of Chen and Shah correlations. The test conditions from which the local heat transfer coefficients were calculated and presented in this section are highlighted in Figure 6.22

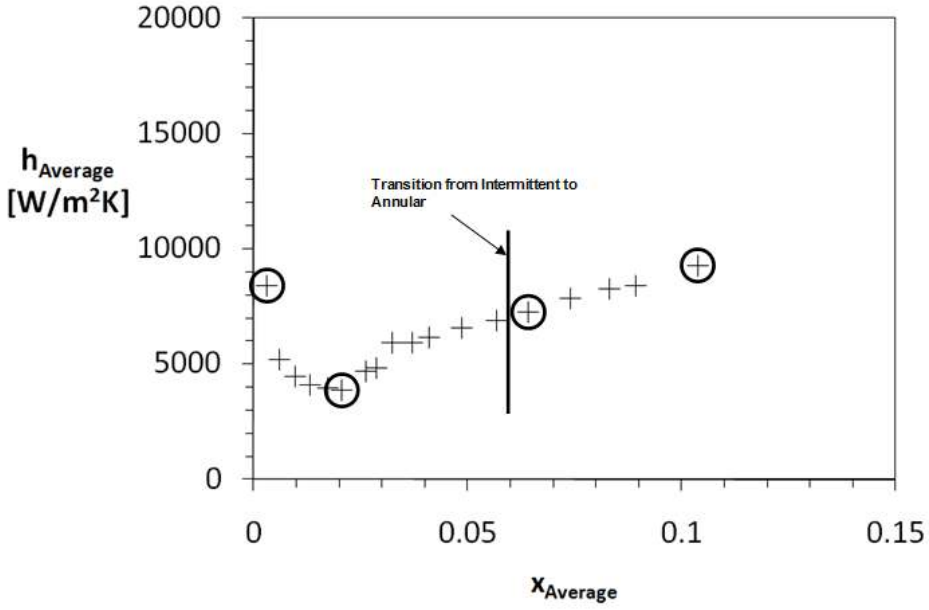

Figure 6.22 Average heat transfer coefficient variation with vapor quality. FC-87 in 500 micron channel, the mass flux is 350 kg/m^{2}s, and the applied heat flux is 1 – 30 W/cm^2 of the test conditions from which the local heat transfer coefficients were selected to be presented in this section

As can be seen in Figure 6.22, the 4 test conditions selected correspond to the: ***a.*** minimum heat flux, ***b.*** minimum average heat transfer coefficient (inflection point), ***c.*** transition to Annular flow, and ***d.*** maximum applied heat flux.

a. Local Heat Transfer Coefficients of FC-87 in 500 micron Gap (G=350 Kg/m^{2}s, q''= 1 W/cm^2)

Local heat transfer coefficients of 350 kg/m^{2}s flow of FC-87 in 500 micron gap, with an applied heat flux of 1 W/cm^2 are plotted in Figure 6.23. For the modest value of heat flux applied at this test condition, it can be seen that the vapor quality does not vary significantly, and therefore the predicted heat transfer coefficients were almost constant, varying between 2 kW/m^{2}K and 2.1 kW/m^{2}K for Chen, and between 7.2 kW/m^{2}K and 8 kW/m^{2}K for Shah. The measured local heat transfer coefficients, however, vary significantly, decreasing from over 10 kW/m^{2}K to 6 kW/m^{2}K between inlet and outlet.

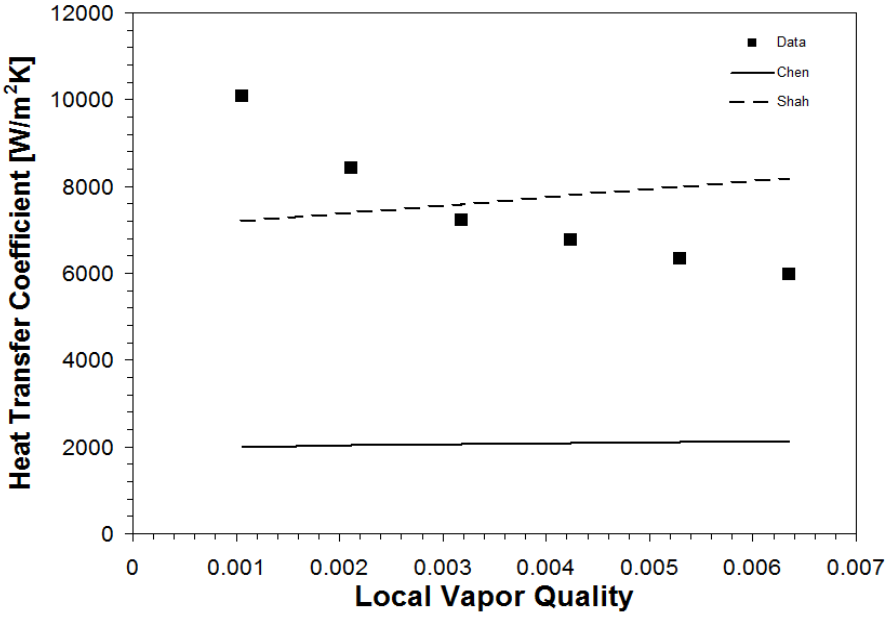

Figure 6.23 Local heat transfer coefficient variation with local vapor quality. FC-87 in 500 micron channel, the mass flux is 350 kg/m^{2}s, and the applied heat flux is 1 W/cm^2

At this test condition, the measured Intermittent flow local heat transfer coefficients are in a better agreement with Shah than Chen, with the average discrepancy with correlations equal to 21% and 71%, respectively.

Figure 6.24 shows the local data plotted on Taitel and Dukler flow regime map. As can be seen, the data is all deep in Intermittent regime, as predicted for such low vapor qualities.

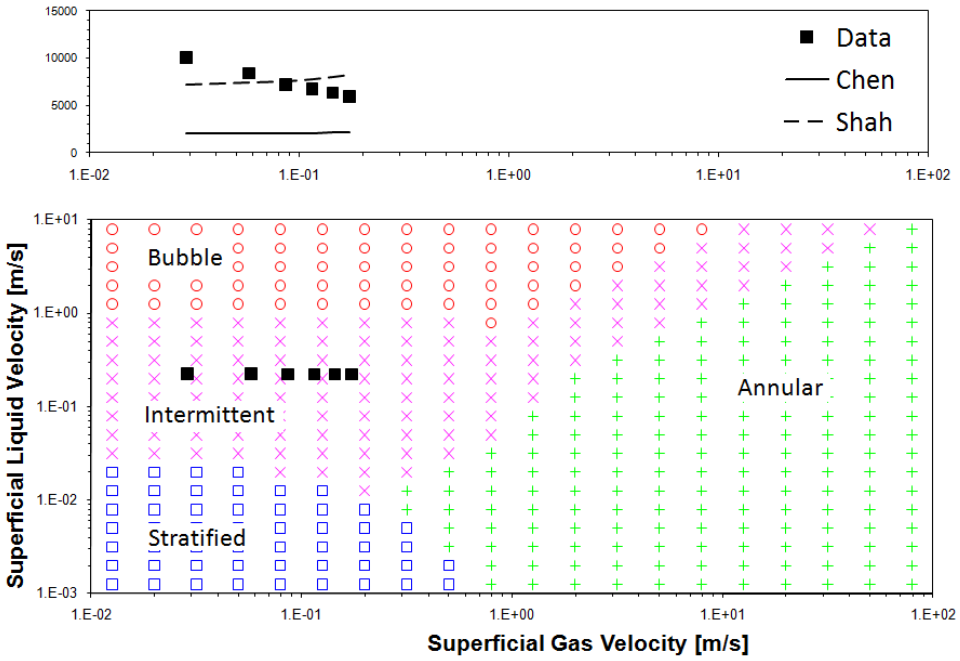

Figure 6.24 Taitel and Dukler maps for local heat transfer coefficient and vapor quality, FC-87 in 500 micron channel, the mass flux is 350 kg/m^{2}s, and the applied heat flux is 1 W/cm^2

The final local temperatures, numerically predicted using ANSYS as described previously in section 6.3.1, are listed in Table 6.2

Table 6.2 Numerically determined and measured local temperature at the location of 9 sensors embedded in the test chip. FC-87 in 500 micron channel, the mass flux is 350 kg/m^{2}s, and the applied heat flux is 1 W/cm^2

Sensor #	Temperature [^{o}C]	
	Numerical	Experiment
101	32.3	32.3
102	32.7	32.5
103	32.2	32.2
104	32.5	32.3
105	32.9	32.6
106	32.1	32.1
107	32.6	32.4
108	32.8	32.6
109	31.8	32.1

As can be seen in Table 6.2, the temperature variation across the surface is within 1.1 ^{o}C.

b. Local Heat Transfer Coefficients of FC-87 in 500 micron Gap (G=350 Kg/m^{2}s, q''= 6 W/cm^2)

The local heat transfer coefficients and vapor quality for a slightly higher heat flux of 6 W/cm^2 are presented in this section. This test condition corresponds to the minimum measured average heat transfer coefficient at a mass flux of 350 kg/m^{2}s, as shown previously in Figure 6.22.

Figure 6.25 displays the local heat transfer coefficient variation with local vapor qualities. It can be seen that the heat transfer coefficient is decreasing with the increasing quality, since the heat transfer coefficient values drop from 4.5 kW/m^{2}K to 3.5 kW/m^{2}K as the quality increases from below 1% to slightly over 4%. The heat transfer coefficient behavior is in qualitative

agreement with the expected behavior as seen in the characteristic, M-shaped heat transfer coefficient curve, described in Chapter 3, where the heat transfer coefficient is decreasing in the intermittent flow regime. The predictions of Chen and Shah correlations are also plotted in Figure 6.25. It can be seen the measured local heat transfer coefficients are bound by the predictions of Chen and Shah, with the data under-predicted by Chen, and over-predicted by Shah. The average discrepancy between the data presented in Figure 6.25 and the two classical correlations is 33% for Shah and 30% for Chen.

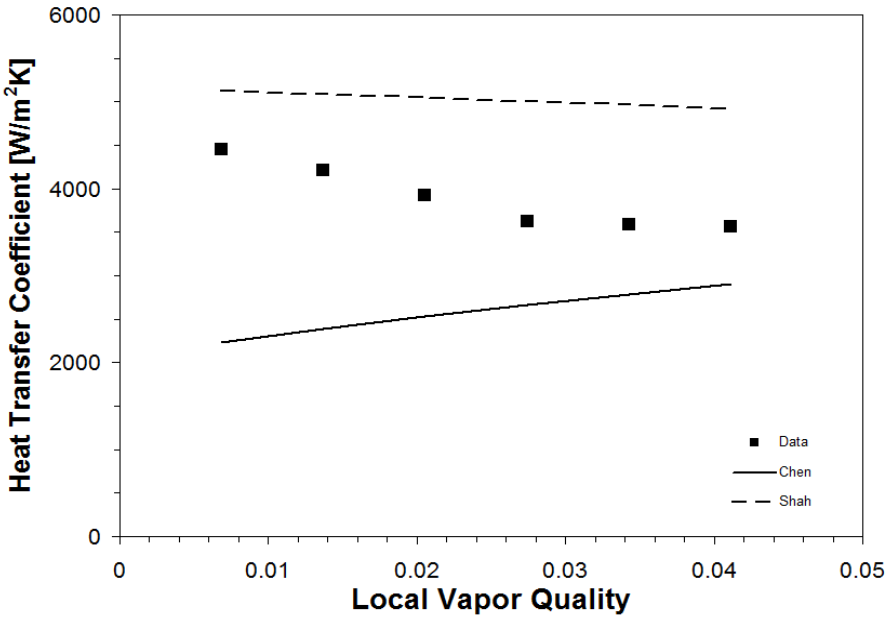

Figure 6.25 Local heat transfer coefficient variation with local vapor quality. FC-87 in 500 micron channel, the mass flux is 350 kg/m^{2}s, and the applied heat flux is 6 W/cm^2

The same data subset is plotted on the Taitel and Dukler flow regime map, and presented in Figure 6.26.

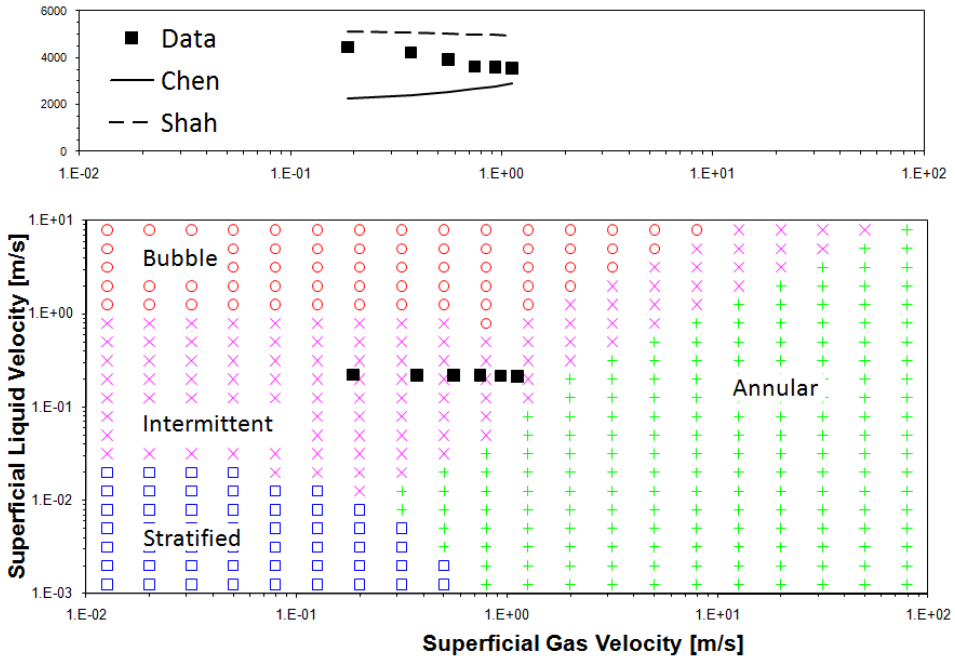

Figure 6.26 Taitel and Dukler maps for Local heat transfer coefficient and vapor quality, FC-87 in 500 micron channel, the mass flux is 350 kg/m^{2}s, and the applied heat flux is 6 W/cm^2

As can be seen in Figure 6.26, the data subset is entirely in the Intermittent flow regime, the local heat transfer coefficient behavior supports the Taitel and Dukler map prediction, as the local heat transfer coefficient is slightly decreasing as it progresses in the Intermittent flow, a behavior observed and described in the characteristic, M-shaped heat transfer coefficient curve.

The local measured and numerically predicted temperatures are compared in Table 6.3.

Table 6.3 Numerically determined and measured local temperature at the location of 9 sensors embedded in the test chip. FC-87 in 500 micron channel, the mass flux is 350 kg/m^{2}s, and the applied heat flux is 6 W/cm^2

Sensor #	Temperature [^{o}C]	
	Numerical	Experiment
101	46.8	47.3
102	48.5	47.8
103	45.9	46.0
104	47.0	47.3
105	48.7	49.4
106	45.1	45.8
107	47.1	47.3
108	48.6	47.7
109	44.8	44.1

As can be seen in Table 6.3, the surface is fairly isothermal with the greatest difference between any two measured temperatures not exceeding 5.3 ^{o}C. The greatest discrepancy between numerically determined and measured temperature for this data subset is 0.9 ^{o}C, for sensor number 108.

c. Local Heat Transfer Coefficients of FC-87 in 500 micron Gap (G=350 Kg/m^{2}s, q''= 19 W/cm^2)

The local heat transfer coefficients for a higher heat flux of 19 W/cm^2 are presented next. This data subset was selected because of the local vapor quality values near the transition boundary from Intermittent to Annular flow. The local heat transfer coefficients variation with the local vapor quality is displayed in Figure 6.27. Although not varying steeply, it can be seen that the heat

transfer coefficient locus goes through an inflection point near the vapor quality of 9%, where the local heat transfer coefficient curve changes slope, as it decreases from 8 kW/m^{2}K to 6 kW/m^{2}K, before it increases again to 8 kW/m^{2}K.

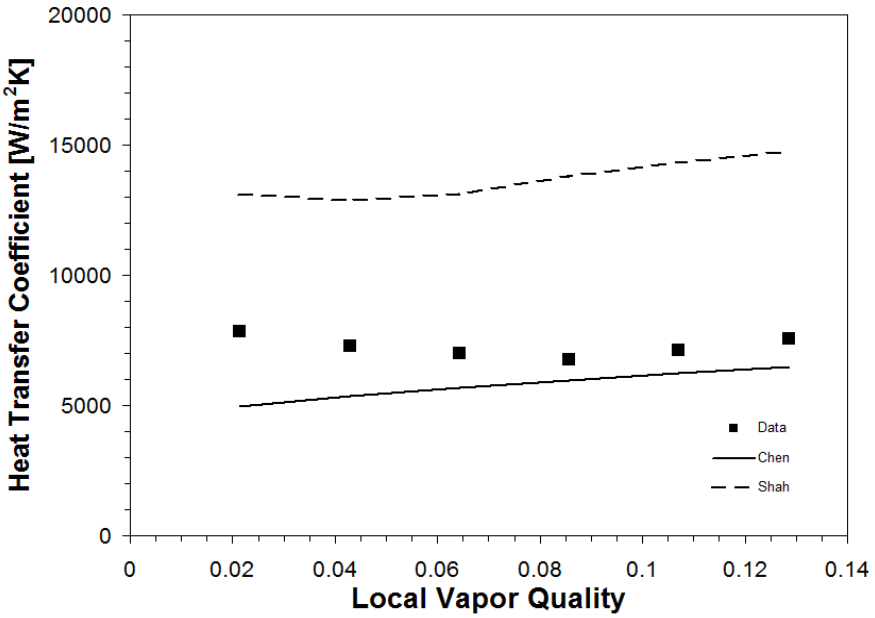

Figure 6.27 Local heat transfer coefficient variation with local vapor quality. FC-87 in 500 micron channel, the mass flux is 350 kg/m^{2}s, and the applied heat flux is 19 W/cm^2

The same data subset is plotted on Taitel-Dukler flow regime map, and is presented in Figure 6.28.

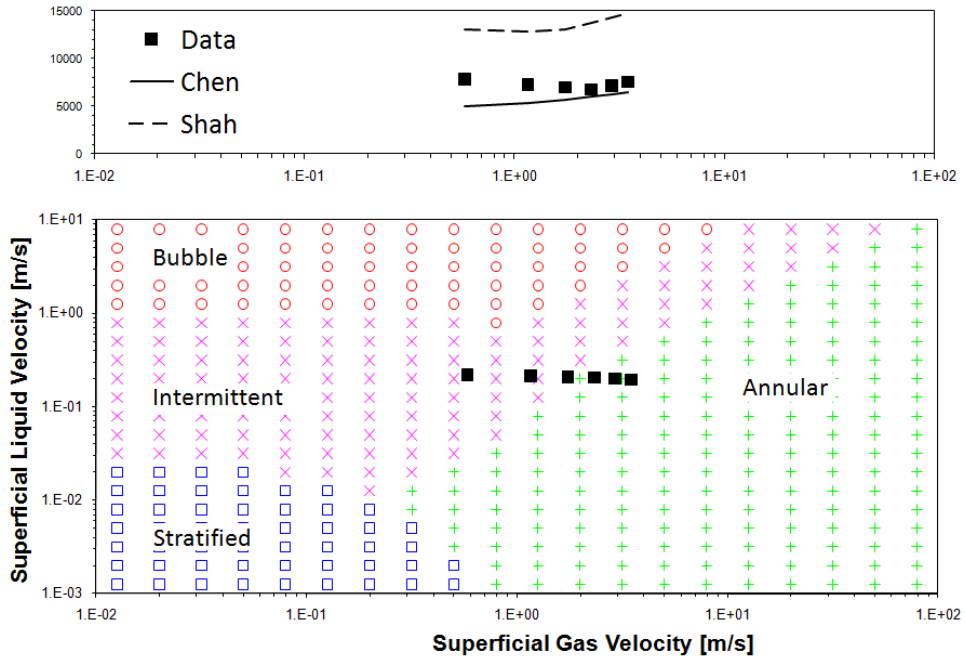

Figure 6.28 Taitel and Dukler maps for local heat transfer coefficient and vapor quality, FC-87 in 500 micron channel, the mass flux is 350 kg/m^{2}s, and the applied heat flux is 19 W/cm^2

As can be seen in Figure 6.28, the inflection point in the heat transfer coefficient curve occurs in the proximity of the transition from Intermittent to Annular flow. While the data is bound by the predictions of Chen and Shah, the discrepancy of the data with Chen correlation is smaller than Shah across the two flow regimes, with average discrepancy as high as 89% between the data and the predictions of Shah correlation, and merely 20% between the data and the predictions of Chen. Moreover, the predictions of Chen are remarkably close to the Annular flow data, with a discrepancy of only 12% for the three Annular flow data points in this subset.

The numerical predictions and measured temperatures are compared in Table 6.4. It can be seen that the test chip wall is becoming less isothermal as the applied heat flux increases, as the greatest difference between temperatures at any two sensors is as high as 6.3 ^{o}C. The greatest

discrepancy between numerically determined and measured temperature is only 1 ^{o}C, for temperature predictions at the location of sensors 105, 106, and 109.

Table 6.4 Numerically determined and measured local temperature at the location of 9 sensors embedded in the test chip. FC-87 in 500 micron channel, the mass flux is 350 kg/m^{2}s, and the applied heat flux is 19 W/cm^2

Sensor #	Temperature [^{o}C]	
	Numerical	Experiment
101	59.7	59.9
102	58.4	58.4
103	57.8	58.3
104	58.9	58.8
105	54.8	55.8
106	55.9	56.9
107	59.0	58.4
108	58.7	58.9
109	54.6	53.6

d. Local Heat Transfer Coefficients of FC-87 in 500 micron Gap (G=350 Kg/m^{2}s, q''= 31 W/cm^2)

Finally, the local heat transfer coefficient results are presented for the highest applied heat flux at the same gap size and mass flux as the previous cases in this comparison. The applied heat flux is equal to 31 W/cm^2. The data subset spans across the Intermittent and Annular flow regimes. As can be seen in Figure 6.29, local heat transfer coefficient is increasing continuously, with the

data closer to the prediction of Chen than that of Shah. The average discrepancy between correlations' predictions and data across this subset is 99% for Shah, and 30% for Chen.

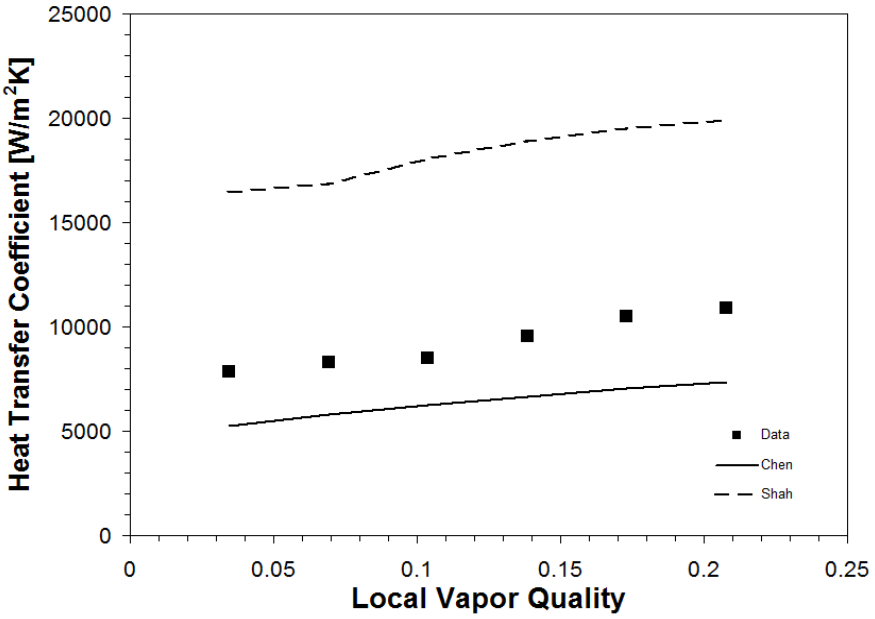

Figure 6.29 Local heat transfer coefficient variation with local vapor quality. FC-87 in 500 micron channel, the mass flux is 350 kg/m^{2}s, and the applied heat flux is 31 W/cm^2

The same data subset is plotted on the Taitel-Dukler flow regime maps, as shown in Figure 6.30. It can be seen that local heat transfer coefficient is increasing continuously, with the locus showing more positive slope as the data progresses in the Annular flow regime.

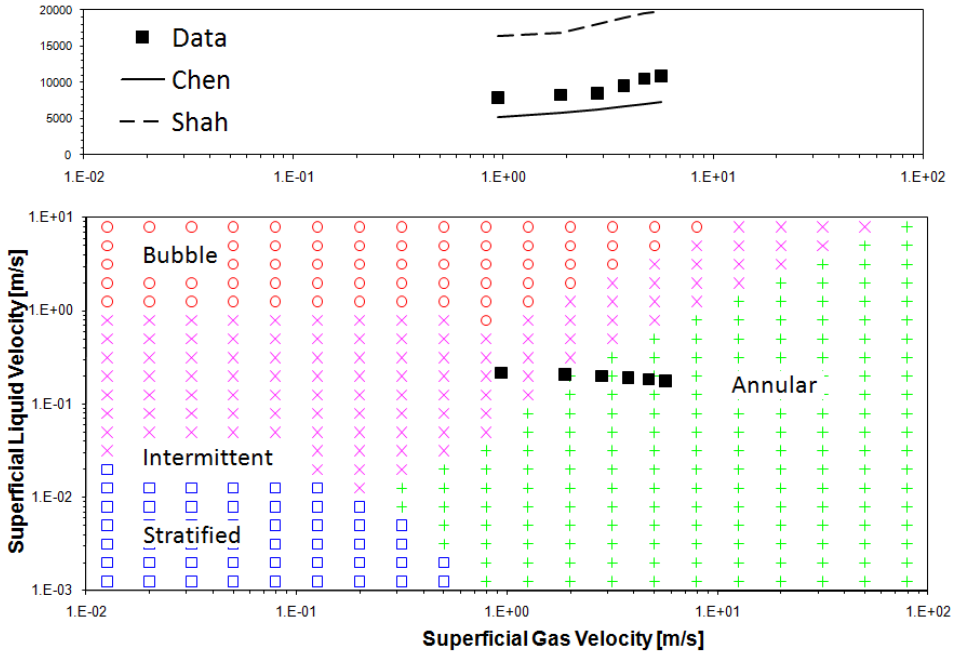

Figure 6.30 Taitel and Dukler maps for local heat transfer coefficient and vapor quality, FC-87 in 500 micron channel, the mass flux is 350 kg/m^{2}s, and the applied heat flux is 31 W/cm^2

The numerically determined temperatures are compared to the measured temperatures at the locations of the 9 embedded sensors. The data is listed in Table 6.5. It can be seen that the surface becomes highly non-isothermal, with a fairly large temperature gradient, equal to 13.2 ^{o}C between temperatures measured at sensor 105 and sensor 106. This raises a concern about the cooling uniformity of microgap coolers used for cooling of high flux electronic components, as well as the predictability of classical correlations, as will be discussed later in this chapter.

Table 6.5 Numerically determined and measured local temperature at the location of 9 sensors embedded in the test chip. FC-87 in 500 micron channel, the mass flux is 350 kg/m^{2}s, and the applied heat flux is 31 W/cm^2

Sensor #	Temperature [^{o}C]	
	Numerical	Experiment
101	68.6	67.7
102	61.8	62.4
103	69.8	69.5
104	68.8	67.9
105	58.7	58.1
106	71.8	71.3
107	68.9	68.0
108	62.6	63.5
109	71.5	69.9

6.4 Span-Wise Variations in Local Heat Transfer Coefficients

In order to explore the local heat transfer coefficients variation in the downstream direction, as well as their dependency on local vapor quality, two different configurations for the numerically predicted local heat transfer coefficients are compared.

Figure 6.31 displays the 18 zones used to define and calculate the local heat transfer coefficients in this study. These local values were defined in section 6.4, and are used later in section 6.5, where they are compared to the predictions of Chen and Shah classical correlations.

A schematic of the 6-zones configuration is shown in Figure 6.32. The 6-zone configuration, providing the spanwise-averaged axially local heat transfer coefficients, has been used in this chapter in all graphical representations of heat transfer coefficients; i.e. all figures

displaying local heat transfer coefficients variations with local vapor quality as well the local data on Taitel and Dukler flow regime maps.

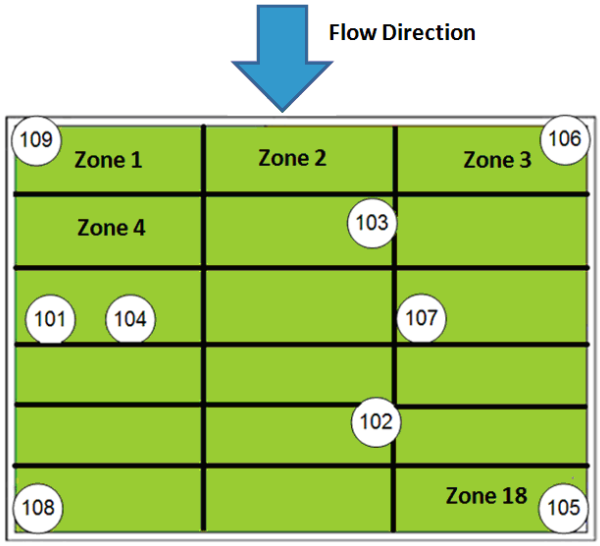

Figure 6.31 The TTV chip with the built-in sensors' locations and the 18 zones configuration imposed on the chip surface

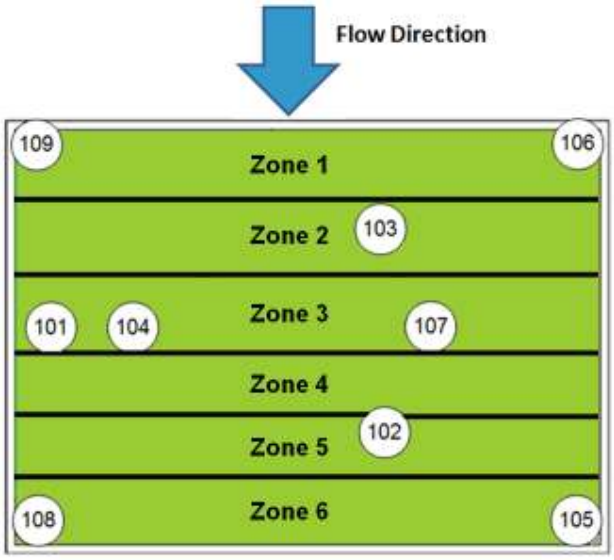

Figure 6.32 The TTV chip with the built-in sensors' locations and the 6 zones configuration imposed on the chip surface

The 18 zones predictions for two-phase flow of FC-87 in 500 micron gap channel at a mass flux of 350 kg/m^{2}s and under a modest heat flux of 1W/cm^2 are listed in Table 6.6.

In the table, the 6-zones local heat transfer coefficients are listed as well, along with discrepancy between each of the 18 local heat transfer coefficients, and its location's corresponding value of the "6-zone local h's"

Table 6.6 Local heat transfer coefficients data comparison for the 6-zones and 18-zones configurations of the same data subset; FC-87 in 500 micron channel, the mass flux is 350 kg/m^{2}s, and the applied heat flux is 1 W/cm^2

Zone #	18 Zones h (W/m^{2}K)	6 Zones h (W/m^{2}K)	Discrepancy (%)
1	10170	10069	1
2	10089	10069	0
3	9975	10069	-1
4	8503	8418	1
5	8582	8418	2
6	8356	8418	-1
7	7182	7232	-1
8	7234	7232	0
9	7232	7232	0
10	6649	6756	-2
11	6839	6756	1
12	6682	6756	-1
13	6143	6339	-3
14	6471	6339	2
15	6443	6339	2
16	6049	5971	1
17	5793	5971	-3
18	6043	5971	1

As can be seen in Table 6.6, the data is almost identical for the data subset taken at modest heat flux. The span-wise variations of local heat transfer coefficients were small, as the

discrepancy between any of the 18 local heat transfer coefficients and their corresponding span-wise averaged value did not exceed 3%, as presented in Table 6.6.

In a similar style, the local two-phase flow heat transfer coefficients are presented in Table 6.7 for the 350 kg/m^{2}s flow of FC-87 in 500 micron microgap channel under a much higher applied heat flux of 31 W/cm^2.

Table 6.7 Local heat transfer coefficients data comparison for the 6-zones and 18-zones configurations of the same data subset; FC-87 in 500 micron channel, the mass flux is 350 kg/m^{2}s, and the applied heat flux is 31 W/cm^2

Zone #	18 Zones h (W/m^{2}K)	6 Zones h (W/m^{2}K)	Discrepancy (%)
1	8248	7867	5
2	7607	7867	-3
3	7907	7867	1
4	8058	8284	-3
5	8280	8284	0
6	8487	8284	2
7	8371	8510	-2
8	8409	8510	-1
9	8510	8510	0
10	9364	9550	-2
11	10378	9550	9
12	8510	9550	11
13	11053	10514	5
14	10778	10514	3
15	9905	10514	-6
16	11693	10879	7
17	10755	10879	-1
18	10205	10879	-6

As can be seen in Table 6.7, the discrepancy between each of the 18 local heat transfer coefficients and its corresponding "span-wise-averaged" value can reach as high as 11% at the heat flux of 31 W/cm^2. This is due to temperature non-uniformities across the chip surface, which in this condition were as high as 13. 1^{o}C.

From the comparisons in Table 6.6 and Table 6.7 it can be seen that the span-wise variations in heat transfer coefficients are somewhat modest at low heat fluxes, and become significant at higher applied heat fluxes, where more special resolution is necessary in order to minimize the uncertainty of local heat transfer coefficients predictions in microgap coolers.

6.5 Comparison to Classical Correlations

The average and local two-phase heat transfer coefficients were compared to Chen and Shah heat transfer correlations. Average heat transfer coefficients were obtained as described in section 6.1 and 6.2. Local heat transfer coefficients were estimated via numerical modeling using ANSYS as described in Section 6.3.

6.5.1 Comparison Metric

The average discrepancy between the predicted and measured heat transfer coefficients was calculated as:

$$\varepsilon_i = \frac{\left| h_{predicted} - h_{measured} \right|}{h_{measured}}$$

(6.7)

and

$$\varepsilon_{average} = \frac{1}{n} \sum_{i}^{n} \varepsilon_i$$

(6.8)

6.5.2 Average Heat Transfer Coefficients

The average discrepancy between the correlations' predictions and the measured average heat transfer coefficients is listed in Table 6.8. As can be seen in Table 6.8, the Chen correlation – based on the average quality in the channel has a smaller overall discrepancy across the 345 data test conditions with an average discrepancy of 36%, while the Shah correlation – again base don the average quality - yielded an overall discrepancy of 52%.

The discrepancy between measured and predicted values was not affected greatly by fluid properties, yet it can be seen that FC-87 data is in a slightly better agreement with the correlations than HFE-7100 data.

Gap size was the most critical parameter in this comparison. It can be seen from Table 6.8 that the agreement between data and the classical heat transfer correlations varies strongly for microgap channels of different gap size. The discrepancy of measured data with Chen is equal to 65%, 34%, and 24% for the 100 micron, 200 micron, and 500 micron gaps, respectively. A similar

trend was observed in the discrepancy between the measured heat transfer coefficient and Shah correlation, where the discrepancy was found to equal 94%, 57 %, and 27% for gap sizes of 100 micron, 200 micron, and 500 micron, respectively. It is interesting to note that for the largest channel tested – 500 microns - the Shah and Chen correlations yielded nearly identical predictive capability

When separating the data based on the Taitel-Dukler flow regime classification , the Shah correlation is seen to perform best for data that fall in the Intermittent flow regime, with a discrepancy of 36% with the measured data, while the discrepancy between the predictions of Chen and the measured data is 40%. The Annular flow data, however, shows a different trend, with the Chen correlation displaying the smaller discrepancy, with merely 28% off the measured values, while Shah predicted the Annular heat transfer coefficient with a rather large discrepancy of 86%. Similar trends were reported by Kim et al (2007), Bar-Cohen et al (2009), and Ali et al (2010).

Table 6.8 Discrepancy between predicted and measured average heat transfer coefficients

Average Heat Transfer Coefficients Comparison		Number of Points	Discrepancy %	
			Chen	Shah
All Data		345	36	52
Fluid	**HFE-7100**	172	42	58
	FC-87	173	31	45
Gap Size	**100 micron**	78	65	94
	200 micron	107	34	57
	500 micron	160	24	27
Flow Regime	**Intermittent**	241	40	36
	Annular	104	28	86

6.5.3 Local Heat Transfer Coefficients

The local heat transfer coefficients were also compared to the predictions of the classical correlations. The local heat fluxes on the wetted surface was determined using ANSYS, and all 345 test conditions were treated as described in Section 6.3, yielding 345 x 18 = 6210 data points.

As can be seen in Table 6.9, the discrepancy between data and correlations for local heat transfer coefficients followed the same trend observed in average values and listed in Table 6.8. However, applying the local condition has helped reduce the discrepancy between predictions and data across the full data set. The discrepancy between data and correlation's predictions for Intermittent flow was down to 33% for both correlations, from 40% and 36% for Chen and Shah, respectively.

The Annular flow data is still better predicted by Chen than Shah, and the discrepancy between data and Chen's predictions is down to 23% from 28% when local values were used.
The agreement between data and correlations has the same trend for local and average values when it is classified by gap size, with the better agreement is found at the larger gap of 500 micron, and the agreement deteriorating for both correlations with the gap size as the gap size get smaller and changes from 500 to 100 micron.

The discrepancy was moderately smaller for FC-87 data than HFE-7100 data, with the FC-87 data showing discrepancy of 26% and 41% with Chen and Shah, respectively, while the HFE-7100 data showing a discrepancy of 35% and 53% with same correlations.

Table 6.9 Discrepancy between predicted and numerically calculated local heat transfer coefficients

Local Heat Transfer Coefficients Comparison		Number of Points	Discrepancy %	
			Chen	Shah
All Data		6210	30	47
Fluid	**HFE-7100**	3096	35	53
	FC-87	3114	26	41
Gap Size	**100 micron**	1404	54	85
	200 micron	1926	28	52
	500 micron	2880	20	25
Flow Regime	**Intermittent**	4338	33	33
	Annular	1872	23	78

Chapter 7

Conclusions and Future Work

7.1 Conclusions

This study focuses on the thermal characteristics of microgap coolers, and it details an experimental and numerical investigation of a TTV chip that is cooled via two-phase flow in microgap channels.

A detailed analysis of microchannel and microgap heat transfer data for two-phase flow of refrigerants and dielectric liquids, gathered from the open literature and sorted by the Taitel and Dukler flow regime mapping methodology, reveals the existence of the three primary flow regimes, i.e. Bubble, Intermittent, and Annular, along with Stratified flow for horizontal configurations, in miniature channels. However, the Annular flow regime is found to be the dominant regime for this thermal transport configuration and its prevalence is seen to grow with decreasing channel diameter and to become dominant for refrigerant flow in channels below 0.1 mm diameter.

A characteristic M-shaped heat transfer coefficient variation with quality (or superficial velocity) for the flow of refrigerants and dielectric liquids in miniature channels has been defined. The inflection points in this M-shaped curve are seen to equate approximately with flow regime transitions, including a first maximum at the transition from Bubble to Intermittent flow, a

decrease in the Intermittent regime followed by a sharp increase on transition to Annular flow, and a second maximum at moderate qualities in Annular flow just before local dryout begins.

Comparison of the microgap refrigerant data gathered from the literature to existing classical correlations reveals that the Chen correlation provides overall agreement to within a standard deviation of 38% for the entire data set. However, classification of the data by flow regime does allow for improved predictive accuracy. It is thus shown that the dominant, low quality Annular data could be correlated by the Chen correlation to within an average discrepancy of just 24%, while the Shah correlation provides agreement to within an average discrepancy of 32% (vs 72% for Chen) for data in the Intermittent regime, and the modified Gungor-Winterton correlation to approximately 37% (vs 39% for Chen) for the moderate-quality annular flow data.

A long channel test section was designed for cooling an Intel TTV test chip. The TTV chip can be heated by powering a serpentine heater 800 micron below the surface. The test chip is equipped with 9 temperature sensors embedded in the silicon chip. Experiments were performed with three different gap sizes; 100, 200, and 500 micron. Two working fluids were used; HFE-7100 and FC-87, mass fluxes ranged from 120 to 2800 kg/m^2s and applied heat flux ranges from 3 to 35 W/cm^2.

345 test conditions were performed; inlet and outlet fluid pressures and temperatures, as well as the measured wall temperature at the 9 locations of the chip embedded thermistors were stored and processed. Wall-averaged as well as local heat transfer coefficients were calculated, and

the data was sorted by flow regime according to the Taitel-Dukler flow regime mapping methodology.

The data was then compared to the predictions of Chen and Shah classical correlations. Channel-averaged heat transfer coefficients were found to agree reasonably well with the classical correlations, with the data having an overall 36% discrepancy with Chen correlation and an overall 52% discrepancy with Shah correlation.

Numerical simulations were used to determine the local heat flux and therefore the local heat transfer coefficients. ANSYS was used to create a numerical code simulating the TTV test chip, and determine the local heat flux on the wetted surface, and therefore the local heat transfer coefficient. Iterations were performed until the agreement between the numerical results and measured temperatures was as large as $1^{o}C$. The test chip surface was then divided into 18 zones, yielding 6210 values of zonal heat transfer coefficient for the entire database of 345 test conditions.

Local heat transfer coefficients curves – when plotted against local vapor qualities – displays a familiar behavior in microgap data, showing different segments of the generic M-shaped heat transfer coefficient curve. Most of the data shows a local maximum at a low vapor quality, then a decreasing trend in the Intermittent flow regime, as the heat transfer coefficient locus goes through an inflection point near the transition from Intermittent to Annular, then keeps on an increasing trend in Annular flow.

Local – or rather "zonal" – heat transfer coefficients were then sorted by flow regime map and compared to the predictions of classical correlations. Chen correlation has the best overall agreement, with and overall discrepancy of 30% compared to Shah's 47%. The correlations' agreement's dependency on the working fluid is not very clear, with Chen having a discrepancy of 35% with HFE-7100 data and 26% with FC-87 data, while Shah showing a discrepancy of 53% and 41% with HFE-7100 and FC-87, respectively.

A stronger trend was observed when separating the data by gap size, with the agreement between data and correlations getting poorer with smaller gap sizes. Chen shows discrepancies of 54%, 28%, and 20% with the 100 micron gap, 200 micron gap, and 500 micron gap, respectively. The data agreement with Shah has the same trend, with Shah having a discrepancy of 85% with 100 micron data, 52% with 200 micron data, and 25% with the 500 micron data. The correlations' dependence on dominant flow regime was also confirmed, with Chen performing best in Annular flow with 23% discrepancy, while both correlations had an equal discrepancy of 33% with Intermittent flow data.

Finally, a surface modification technique was tested. Ribs made of polymer photo-resist were grown on the surface; the ribs' length was 8 micron and two different sets of ribs were grown, separately, with the nominal spacing of 2 and 4 mm. The ribs were meant to physically prevent a dry patch on the surface from spreading across the entire test chip's wetted surface. While the ribs limit the local dryout to the corner region, they did not work as an enhancement mechanism, as the local heat transfer coefficient for the ribbed surface deteriorated in comparison with the bare die surface.

7.2 Future Work

In order to complete this ongoing effort of characterizing and modeling two-phase flow in microgap coolers, future investigations are recommended to add to the current understanding of thermal transport phenomena in these coolers:

- Non-uniform surface temperature are prevalent, even when uniform heat flux is applied. These non-uniformities need to be better predicted to a higher resolution than the current, rather coarse, 18-zones approach.

- Surface modification techniques can be used extensively on future chips, especially non-intrusive techniques such as the one used in this study by growing ribs of polymer photo-resist on the surface. This sets the stage to a new level of fluid direction and manipulation using different pattern of ribs or fins grown on the surface.

- Investigation of heat transfer coefficients at higher vapor qualities and higher heat fluxes is necessary. It would be of a great importance to perform these tests on a new generation of TTV where the upper limit of applied heat flux and maximum allowable wall temperature exceed those of the current TTV.

Appendix A

Surface Modification

In this section, the fabrication process of and reasoning behind growing a set of ribs on the chip surface will be discussed. A set of 8 micron long ribs of polymer photo-resist were grown on the surface of the test chip. The purpose was to have the ribs physically preventing any dry spot from growing across the surface of the test chip, limiting the local dryout to one "channel" without having the disadvantages associated with typical long parallel channel microchannels, such as flow instabilities and reverse flow, among other issues.

A.1 Theoretical Background

Zaitsev et al (2007) studied the rupture of a water film falling down a heated grooved surface. The copper plate was 1 m long with longitudinal grooves of 0.5 x 0.15 mm^2 cross section area, and 2 mm spacing. They found that the threshold heat flux at which an initial stable dry patch forms on the grooved surface is about two times higher than that on a smooth surface. Moreover, the grooves prevent dry patches from spreading over the total heated surface, essentially delaying the onset of the critical heat flux. Similar modifications were implemented in our current chip surface, as a potential enhancement solution for thin film instability.

For the present study, a set of ribs of polymer photo-resist was grown on the surface of the test chip, to create a "finned" surface similar to the experiment of Zaitsev et al (2007). The purpose

of the ribs is to prevent local dryout from spreading across the chip, delaying the critical heat flux, and heat transfer crisis.

The ribs length is of the order of the liquid film thickness at a vapor quality that exceeds 50%, where a sharp decreasing trend of heat transfer coefficient is often observed, as the test chip temperature reaches the maximum allowable limit, and cooling performance deteriorates

Using a void fraction correlation, such as Baroczy (1965)

$$\alpha = \left[1 + \left(\frac{1-x}{x} \right)^{0.74} \left(\frac{\rho_v}{\rho_l} \right)^{0.65} \left(\frac{\mu_l}{\mu_v} \right)^{0.13} \right]^{-1} \tag{A.1}$$

With the film thickness expressed as:

$$\delta = (1-\alpha) \cdot H \tag{A.2}$$

Where H is the height of the microgap channel.

Applying the above equations to gap heights of 0.1 – 0.5 mm yield a film thickness of 2 to 10 micron.

Assuming an adiabatic fin (rib) tip, the fin efficiency is calculated, and found to be equal to 99%. Considering the typical local dry spots to be of the order of 2 - 3 mm^2, the ribs spacing was chosen at 2 mm and 4 mm, and the overall addition to the surface area is found to be equal to 3%.

Therefore, it can be assumed that the additional area provided by the presence of the ribs will not, in itself, result in significant enhancement of heat transfer.

The aim of this surface modification is to evaluate the role of ribs, with heights of the order of the film thickness, in delaying the spreading of local dryout, preventing it from turning into global dryout which causes a major crisis in heat transfer, controlling the upper limit of microgap cooling.

A.2. Manufacturing Process

The fabrication process was performed at the University of Maryland's Nano-Fabrication lab. In the process of making the ribs, AZ 4620 polymer photo-resist was used. A few drops of the photo-resist were deposited on top of the test chip surface. The test chip then was spun at 4000 RPM for 40 seconds in order to get the desired photo-resist thickness of 8 micron. Following the spinning process, the test chip was soft-baked at 97 ^{o}C for 15 minutes. Next, a transparent film which has the desired ribs' pattern and spacing was placed on top of the photo-resist-covered test chip and all was exposed to UV light with 365 nm wavelength for 70 seconds. The test chip was then treated with developer for 40 seconds, in order to remove the UV-exposed layer of photo-resist, leaving only the ribs on the surface. The test chip was then rinsed with de-ionized water and dried.

When the testing of the first ribs' pattern was done, acetone was used to remove the polymer photo-resist ribs, and the process was repeated using different transparent film in order to

make a set of ribs with different spacing. A schematic of the ribs with 4 mm spacing is shown in Figure A.1, the flow direction is displayed on the figure.

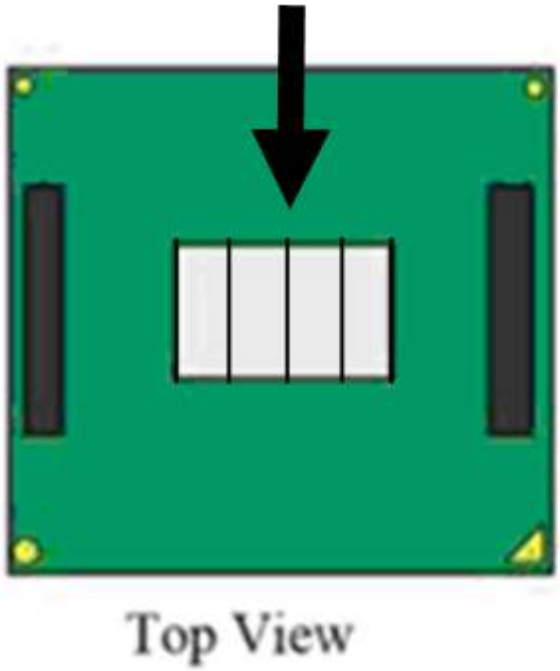

Figure A.1 Schematic of polymer photo-resist ribs on the test chip surface, with a nominal 4 mm spacing. The flow direction is shown on the figure

A.3. Heat Transfer Characteristics

Tests were performed for FC-87 in 100 micron microgap channel with two different sets of ribs, with 2 mm spacing and 4 mm spacing.

Local heat transfer coefficients of FC-87 flowing in 100 micron gap channel are presented in Figure 7.2.

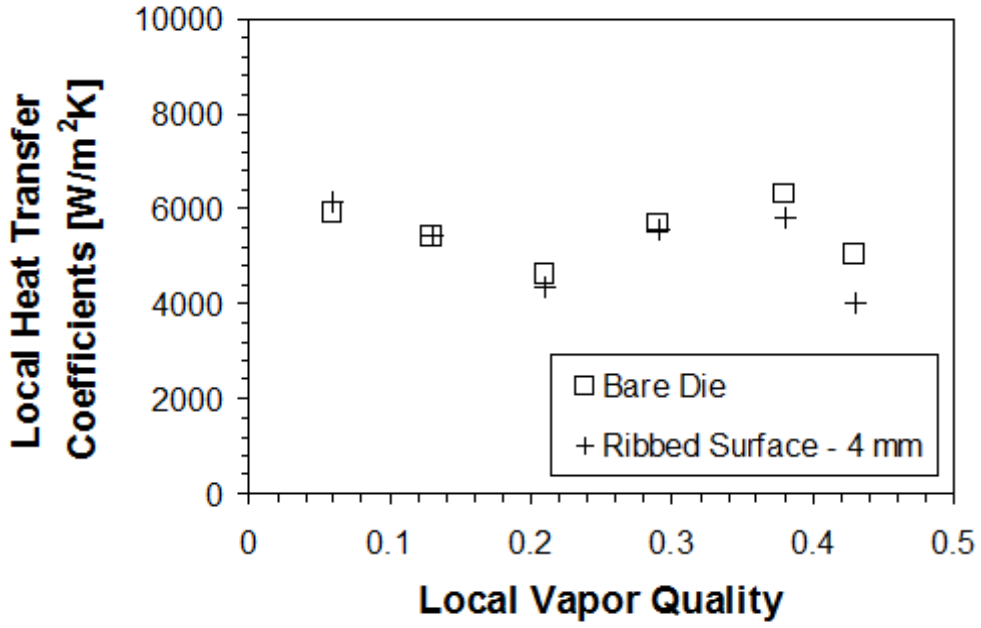

Figure A.2 Local heat transfer coefficients and vapor quality for FC-87 coolant in 100 micron microgap channel, flow rate is 0.5 ml/s and applied heat flux of 35 W/cm^2

As can be seen from the comparison of Figure A.2, the influence of the ribs was rather modest, with the local heat transfer coefficients actually deteriorating slightly for the results with the modified surface when compared to the bare die surface. The local heat transfer coefficients and vapor qualities are listed in Table A.1.

Table A.1 Local heat transfer coefficients for the flow of FC-87 in 100 micron gap, mass flux of 500 kg/m^{2}s, and applied heat flux of 35 W/cm^2

X	Bare Die h [W/m^{2}K]	Ribbed h [W/m^{2}K]
0.06	5914	6123
0.13	5398	5443
0.21	4632	4350
0.29	5700	5550
0.38	6321	5800
0.43	5043	4000

A closer look at the local sensor measured temperatures can add significant insight to the effect of the surface modification. The local temperatures for both tests are listed in Table A.2.

Table A.2 Measured temperatures of bare die and ribbed surface experiment for FC-87 in 100 micron gap, flow rate of 0.5 ml/s and heat flux of 35 W/cm^2

Sensor	Bare Die	Ribbed
101	109.2	110.3
102	91	90.1
103	102.2	103.1
104	108	110.2
106	99.1	97.1
107	91	90.1
108	99.3	107
109	103.2	102.2

It can be seen from Table A.2 that the local temperature of Sensor 108 raised by 8 ^{o}C, the most significant jump of temperature between the two tests. This was due to visible dry patches forming in the corner of the microgap channel, near the exit. It seems from these experiments that the ribs did, in fact, limit the dry patches from spreading across the die surface. However, it did not

succeed as an enhancement mechanism, since the local heat transfer coefficient value decreased when compared to the results from the bare die experiment.

Bibliography

Ali, I.A., Characterization and Modeling of Two-Phase Heat Transfer in Non-Uniformly Heated Microgap Channels, PhD Dissertation, Mechanical Engineering Department, University of Maryland, 2010.

Baker, O., Simultaneous Flow of Oil and Gas, Oil and Gas Journal, Vol. 53, no. 12, pp. 185-195, 1954.

Barajas, A.M., Panton, R.L., The effects of contact angle on two-phase flow in capillary tubes. Int. J. Multiphase Flow 19, 337–346, 1993.

Barnea, D., Unified Model for Predicting Flow-Pattern Transitions for the Whole Range of Pipe Inclinations, International Journal of Multiphase Flow, Vol. 8, no. 3, pp. 243-253, 1987.

Bar-Cohen, A., Ruder, Z., and Griffith, P., Thermal and Hydrodynamic Phenomena in a Horizontal Uniformly Heated Steam Generating Pipe, Journal of Heat Transfer, Vol. 109, no. 3, pp. 739-745, 1987.

Baroczy, C. J., "Correlation of liquid fraction in two-phase flow with applications to liquid metals", Chem. Eng. Prog. Symp. Ser., Vol. 61, No. 57, pp. 179 – 191, 1965.

Bennett, D.L., and Chen, J.C., Forced convective boiling in vertical tubes for saturated pure components and binary mixtures, AIChE Journal, vol. 26, pp. 454 – 461, 1980.

Bergles, A.E., and Kandlikar, S.G., On the Nature of Critical Heat Flux in Microchannels, Journal of Heat Transfer, Vol. 127, no. 1, pp. 101-107, 2005.

Chen, J.C., Correlation for boiling heat transfer to saturated fluids in convective flow, Industrial and Engineering Chemistry - Process Design and Development, Vol. 5 no. 3, pp. 322-329, 1966.

Collier J.G., Forced Convective Boiling, in *Two-Phase Flow and Heat Transfer in the Power and Process Industries,* eds. A. E. Bergles, J. G. Collier, J. M. Delhaye, G. F. Hewitt, and F. Mayinger, Hemisphere, New York, NY, 1981.

Cortina-Diaz, M., and Schmidt, J., Flow Boiling Heat Transfer of n-Hexane and n-Octane in a Minichannel, Proc. the 13th International Heat Transfer Conference, Sydney, Australia, 2006.

Dittus, F.W. and Boelter, L.M.K., Heat transfer in automobile radiators of the tubular type. University of California Publications in Engineering, vol. 2, pp. 443 – 461, 1930.

Figliola, R. and Beasley, D., Theory and Design for Mechanical Measurements, John Wiley & Sons, In., 1995.

Forster, H.K., and Zuber, N., Dynamics of vapor bubbles and boiling heat transfer, AIChe, Journal, vol. 1, no. 4, pp. 531 – 535, 1955.

Frankum, D.P., Wadekar, V.V., and Azzopardi, B.J., Two-Phase Flow Patterns for Evaporating Flow, Experimental Thermal and Fluid Science, Vol. 15, no. 3, 183-192, 1997.

Garimella, S.V., and Singhal, V., Single-phase flow and heat transport and pumping considerations in microchannel heat sinks Heat Transfer Engineering, v 25, n 1, p 15-25, 2004

Ghajar, A., Kim, A.J., and Tang, C., Two-Phase Flow Heat Transfer Measurements and Correlation for the Entire Flow Map in Horizontal Pipes, Proc. the 13th International Heat Transfer Conference, Sydney, Australia, 2006.

Gnielinski, V., New Equations for Heat and Mass Transfer in Turbulent Pipe and Channel Flow, International Chemical Engineer, Vol. 16, pp. 359 – 368, 1976.

Gungor, K.E., and Winterton, R.H.S., A General Correlation for Flow Boiling in Tubes and Annuli, International Journal of Heat and Mass Transfer, Vol. 29, no. 3, pp. 351-358, 1986.

Gungor, K.E., and Winterton, R.H.S., Simplified General Correlation for Saturated Flow Boiling and Comparisons of Correlations with Data, Chemical Engineering Research and Design, Vol. 65, no. 2, pp.148-156, 1987.

Hewitt, G.F., Liquid-Gas Systems, Flow Regimes, in *Handbook of Multiphase Systems,* ed. G. Hetsroni, pp. 2-3 – 2-43, Hemisphere, Washington, D.C., 1982.

Howes, J., et al., Cooling of an IGBT Drive System with vaporizable Dielectric Fluid (VDF,) 24th IEEE Semi-Therm symposium, San Jose, 2008.

Huh, C. and Kim, M.H., Two-Phase Pressure Drop and Boiling Heat Transfer in a Sinlge Horisontal Microchannel, Proc. the 4th International Conference on Nanochannels, Microchannels, and Minichannels, Limerick, Ireland, Paper No. ICNMM2006-9610, 2006.

Intel “Merom” Processor Test Vehicle, User Guide, November, 2005

Kabov O., Cooling of Microelectronics by Thin Liquid Films, Keynote lecture, Proc. Int. Workshop on “Wave Dynamics and Stability of Thin Film Flow Systems”, September 1-4, Chennai, India, Narosa Publishing House, pp. 279-311, 2006.

Kabov, O.A., and Bar-Cohen, A., Cooling technique based on evaporation of thin liquid film in microgaps, ExHFT 2009.

Kandlikar, S.G. and Balasubramanian, P., An extension of the flow boiling correlation to transition, laminar, and deep laminar flows in minichannels and microchannels, Heat Transfer Engineering, Vol. 25, no. 3, pp. 86-93, 2004.

Katto Y. and Ohno H., An Improved Version of The Generalized Correlation of Critical Heat Flux for the Forced Convective Boiling in Uniformly Heated Vertical Tubes, International Journal of Heat and Mass Transfer, Vol. 27, no. 9, pp. 1641-1648, 1984.

Kays, W. M., and Crawford, C., "Convective Heat and Mass Transfer," McGraw-Hill, New York, 1966.

Kays, W. M. and London, A. L., Compact Heat Exchangers, McGraw-Hill, New York, 1984.

Kim, D.W., Convection and Flow Boiling in Microgaps and Porous Foam Coolers, PhD Dissertation, Mechanical Engineering Department, University of Maryland, 2007.

Kuznetsov, V.V. and Shamirzaev, A.S., Boiling Heat Transfer for Freon R21 in Rectangular Minichannel," Proceedings of the 4th International Conference on Nanochannels, Microchannels, and Minichannels, Limerick, Ireland, Paper No. ICNMM2006-96096, 2006.

Lee, H.J. and Lee, S.Y., Heat Transfer Correlation for Boiling Flows in Small Rectangular Horizontal Channels with Low Aspect Ratios, International Journal of Multiphase Flow, Vol. 27, no. 12, pp. 2043-2062, 2001.

Lee, C.Y., Lee, S.Y., Effect of interfacial tensions on transition of two-phase flow pattern in mini-channels. In: Proceedings of third International Conference on Flow Dynamics, pp. 197–198, 2006.

Lee, C.Y., Lee, S.Y., Effect of interfacial tensions on behavior of two-phase plug flow in round mini-channels. In: Proceedings of 18th International Symposium on Transport Phenomena, pp. 1474–1479, 2007.

Lee, C.Y., and Lee, S.Y., Influence of surface wettability on transition of two-phase flow pattern in round mini-channels, Int. J Multiphase Flow, Vol. 34, pp 706 – 711, 2008.

Lin, S., Kew, P.A. and Cornwell, K., Two Phase Heat Transfer to a Refrigerant in a 1 mm Diameter Tube, International Journal of Refrigeration, Vol. 24, no. 1, pp. 51 – 56, 2001.

Mandhane, J.M., Gregory, G.A., and Aziz, K., A Flow Pattern Map for Gas Liquid Flow in Horizontal Pipes, International Journal of Multiphase Flow, Vol. 1, no. 4, 537-553, 1974.

Murray, C. T., International Electronics Manufacturing Initiative (iNEMI) Thermal Roadmap, MEPTEC-2005 Symposium, San Jose, 2005.

Patankar, S. V., Numerical Heat Transfer and Fluid Flow, Hemisphere, 1980.

Patel, C., Thermal Management from Chip Core to the Cooling Tower, MEPTEC-2005 Symposium, San Jose, 2005

Rahim, E. and Bar-Cohen, A., Parametric Dependence of Annular Flow Heat Transfer in Microgaps, Proceedings of the International Heat Transfer Conference, IHTC14-23315, IHTC 14, Washington, DC, USA, 2010.

Rahim, E., Revellin, R., Thome, J., and Bar-Cohen, A., Characterization and Prediction of Two-Phase Flow Regimes in Miniature Tubes, International Journal of Multiphase Flow, Vol. 37, no. 1, pp. 12 – 23, January 2011.

Revellin, R., Thome, J.R., New Diabatic Flow Pattern Map for Evaporating Flows in Microchannels, Proc. the 13th International Heat Transfer Conference, Sydney, Australia, 2006.

Serizawa, A., Feng, Z.P., Two-Phase Flow in Microchannels, Proc. 4th International Conference of Multiphase Flows, New Orleans, USA. Keynote Lecture, 2001.

Shah, M.M., A New Correlation for Heat Transfer During Boiling Flow Through Pipes, ASHRAE Transactions, Vol. 82, no. 2, pp. 66-86, 1976.

Shah, R. K. and London, A. L., Laminar Flow Forced Convection in Ducts, Supplement 1 to Advances in Heat Transfer, Academics, New York, 1978.

Shoham, O., Flow Pattern Transition and Characterization in Gas-Liquid Flow in Inclined Pipes, PhD. Dissertation, Tel-Aviv University, Ramat-Aviv, Israel, 1982.

Sharar, D., Morgan, B., Jankowski, N.R., and Bar-Cohen, A., Two-Phase Minichannel Cold Plate for Army Vehicle Power Electronics, Proceedings of the ASME 2011 Pacific Rim Technical Conference and Exposition on Packaging Integration of Electronic and Photonic Systems, InterPACK2011, Paper no. InterPACK2011-52079, Portland, OR, USA. 2011.

Sieder, E.N. and Tate, G.E., Heat Transfer and Pressure Drop of Liquids in Tubes, Industrial and Engineering Chemistry, Vol. 28, no. 12, pp. 1429-1435, 1936.

Sobierska, E., Kulenovic, R., and Mertz, R., Heat Transfer Meachanism and Flow Pattern During Flow Boiling of Water in a Vertical Narrow Channel – Experimental Results, Proc. of the 4th International Conference on Nanochannels, Microchannels, and Minichannels, Limerick, Ireland, Paper No. ICNMM2006-96141, 2006.

Tabatabai, A., and Faghri, A., A New Two-Phase Flow Map and Transition Boundary Accounting for Surface Tension Effects in Horizontal Miniature and Micro Tubes, Journal of Heat Transfer, v 123, n 5, p 958-968, 2001.

Taitel, Y., and Dukler, A.E., A Model For Predicting Flow Regime Transitions in Horizontal and Near Horizontal Gas-Liquid Flow, AIChE Journal, Vol. 22, no. 1, pp. 47-55, 1976.

Taitel, Y., Lee, N., Dukler, A.E., Transient Gas-Liquid Flow in Horizontal Pipes: Modeling the Flow Pattern Transitions, AIChE Journal, Vol. 24, no. 5, pp. 920-934, 1978.

Taitel, Y., Barnea, D., and Dukler, A.E., Modelling flow pattern transitions for steady upward gas-liquid flow in vertical tubes, AIChE J. 26 (3) 345 – 354, 1980.

Taitel, Y., and Dukler, A.E., Effect of Pipe Length on the Transition Boundaries for High Viscosity Liquids, International Journal of Multiphase Flow, Vol. 13, no. 4, pp 577-581, 1987

Taitel, Y., Flow Pattern Transition in Two Phase Flow, Keynote, Proc. of the 9th International Heat Transfer Conference, Jerusalem, Israel, pp. 237-254, 1990.

Tosaya, E., Processor Packaging thermal View, MEPTEC-2006 Symposium, San Jose, 2006.

Ullmann, A., and Brauner, N., The Prediction of Flow Pattern Map in Minichannels, Proc. 4th Japanese-European Two-Phase Flow Group Meeting, Kanabaikan, Kyoto, 2006.

Wang, P., McCluskey, F.P., and Bar-Cohen, A. Evaluation of Two-Phase Cold Plate for Cooling Electric Vehicle Power Electronics, Proceedings of IMECE 2011, Paper no. IMECE2011-64330. Denver, CO., USA, 2011.

Weisman, J., Duncan, D., Gibson, J., and Crawford, T., Effect of Fluid Properties and Pipe Diameter on Two-Phase Flow Pattern in Horizontal Lines, International Journal of Multiphase Flow, Vol. 5, no. 6, 437-462, 1979.

Wojtan, L., Revellin, R., and Thome, J.R., Investigation of Critical Heat Flux in Single, Uniformly Heated Microchannels, Proc. ECI International Conference on Heat Transfer and Fluid Flow in Microscale, Castelvecchio Pascoli, Italy, 2005.

Yang, Y., and Fujita, Y., Flow Boiling Heat Transfer and Flow Pattern in Rectangular Channel of Mini-Gap, Proc. 2nd International Conference on Microchannels and Minichannels, New York, USA, Paper no. ICMM2004-2383, 2004.

Zaitsev, D.V., Aviles, M., Auracher, H., and Kabov, O.A., Rupture of a subcooled liquid film falling down a heated grooved surface. Microgravity Science and Technology. XIX-3/4, pp 71 – 74, 2007.